LETTER

doi:10.1038/nature12421

Microscopic origin of the '0.7-anomaly' in quantum point contacts

Florian Bauer[1,2]*, Jan Heyder[1,2]*, Enrico Schubert[1], David Borowsky[1], Daniela Taubert[1], Benedikt Bruognolo[1,2], Dieter Schuh[3], Werner Wegscheider[4], Jan von Delft[1,2] & Stefan Ludwig[1]

Quantum point contacts are narrow, one-dimensional constrictions usually patterned in a two-dimensional electron system, for example by applying voltages to local gates. The linear conductance of a point contact, when measured as function of its channel width, is quantized[1–3] in units of $G_Q = 2e^2/h$, where e is the electron charge and h is Planck's constant. However, the conductance also has an unexpected shoulder at $\sim 0.7 G_Q$, known as the '0.7-anomaly'[4–12], whose origin is still subject to debate[11–21]. Proposed theoretical explanations have invoked spontaneous spin polarization[4,17], ferromagnetic spin coupling[19], the formation of a quasi-bound state leading to the Kondo effect[13,14], Wigner crystallization[16,20] and various treatments of inelastic scattering[18,21]. However, explicit calculations that fully reproduce the various experimental observations in the regime of the 0.7-anomaly, including the zero-bias peak that typically accompanies it[6,9–11], are still lacking. Here we offer a detailed microscopic explanation for both the 0.7-anomaly and the zero-bias peak: their common origin is a smeared van Hove singularity in the local density of states at the bottom of the lowest one-dimensional subband of the point contact, which causes an anomalous enhancement in the Hartree potential barrier, the magnetic spin susceptibility and the inelastic scattering rate. We find good qualitative agreement between theoretical calculations and experimental results on the dependence of the conductance on gate voltage, magnetic field, temperature, source–drain voltage (including the zero-bias peak) and interaction strength. We also clarify how the low-energy scale governing the 0.7-anomaly depends on gate voltage and interactions. For low energies, we predict and observe Fermi-liquid behaviour similar to that associated with the Kondo effect in quantum dots[22]. At high energies, however, the similarities between the 0.7-anomaly and the Kondo effect end.

In our measurements, we use the multigate layout on the surface of a GaAs/AlGaAs heterostructure shown in Fig. 1a. By suitably tuning the central- and side-gate voltages, V_c and V_s, at a fixed top-gate voltage, V_t, we can use the device to define a short, one-dimensional (1D) channel, containing a smooth, symmetric barrier, in the two-dimensional electron system (2DES) buried in the heterostructure. To describe such a quantum point contact (QPC), we adopt a 1D model with local interactions and a smooth potential barrier. We treat interactions perturbatively, using either second-order perturbation theory[23] (SOPT) or the functional renormalization group[24–26] (FRG) approach (Supplementary Information, sections 7 and 6, respectively). The lowest 1D subband of the device is modelled by

$$\hat{H} = \sum_{j\sigma} \left[E_{j\sigma} \hat{n}_{j\sigma} - \tau_j \left(d^\dagger_{j+1\,\sigma} d_{j\sigma} + \text{h.c.} \right) \right] + \sum_j U_j \hat{n}_{j\uparrow} \hat{n}_{j\downarrow} \qquad (1)$$

Here $\hat{n}_{j\sigma} = d^\dagger_{j\sigma} d_{j\sigma}$ counts the number of electrons with spin σ (spin up, $\sigma = \uparrow$ or $+$; spin down, $\sigma = \downarrow$ or $-$) at site j of an infinite, tight-binding chain with hopping amplitude τ_j, on-site interaction U_j and potential energy $E_{j\sigma} = E_j - \sigma\tilde{B}/2$ (Supplementary Fig. 8), and 'h.c.' denotes Hermitian conjugate. The Zeeman energy, $\tilde{B} = |g_{el}|\mu_B B$, describes the effect of a uniform external parallel magnetic field B, where μ_B is the Bohr magneton and g_{el} is the effective g factor (<0 in GaAs). (When similar symbols are used for model parameters and experimental parameters, we add tildes to the former to distinguish them from the latter.) We neglect spin–orbit interactions and other orbital effects. The parameters E_j, U_j and τ_j vary smoothly with j and differ from their bulk values, $E_{bulk} = U_{bulk} = 0$ and $\tau_{bulk} = \tau$ (taken as the unit of energy), only within a central constriction region (CCR) of N sites around $j = 0$, representing the QPC. Sites $j < -N/2$ and $j > N/2$ represent two non-interacting leads, each with bandwidth 4τ, chemical potential μ and bulk Fermi energy $\varepsilon_F = 2\tau + \mu$; we choose $\mu = 0$, implying half-filled leads (Fig. 1b). We set U_j to a fixed value, U, for all but the outermost sites of the CCR, where it drops smoothly to zero.

Within the CCR, we define the QPC barrier by specifying the shape of the 'band bottom' as $\omega_j^{min} = E_j - (\tau_{j-1} + \tau_j) - \mu$ (Fig. 1b, solid black line). We choose ω_j^{min} to define a smooth, symmetric barrier within the CCR, parabolic near the top[3], where we parameterize it as $\omega_j^{min} \approx \tilde{V}_c - \Omega_x^2 j^2 / 4\tau_0$ (Supplementary Information, section 4D). Here $\tilde{V}_c$ sets the barrier height with respect to μ (Fig. 1b, dashed black line), and $\Omega_x \ll \tau$ characterizes its curvature. We first consider the theoretical case of zero temperature, $\tilde{T} = k_B T$ (k_B, Boltzmann's constant), source–drain voltage, $\tilde{V}_{sd} = |e| V_{sd}$, and field, $\tilde{B}$: $\tilde{T} = \tilde{V}_{sd} = \tilde{B} = 0$. As $\tilde{V}_c$ is decreased below 0, the conductance, $g = G/G_Q$, increases from 0 to 1, showing a step of width $\sim\Omega_x$ (about 1.5 meV in our experiment), whose shape depends on U (Fig. 1k). In the upper part of the step, say $0.5 \lesssim g \lesssim 0.9$, we say that the QPC is 'sub-open'; the sub-open regime is of special interest because for measured $g(V_c)$ curves it contains the 0.7-anomaly.

The bare local density of states (LDOS), $A_j^0(\omega)$, for equation (1) has a strong maximum just above the band bottom[18], seen as a yellow–red ridge-like structure in Fig. 1b. In a semiclassical picture, $A_j^0(\omega) \propto 1/v_j(\omega)$, where $v_j(\omega)$ is the velocity at site j of an electron with energy ω with respect to μ. The ridge-like maximum of $A_j^0(\omega)$ above the barrier reflects the fact that electrons move slowest there. In the CCR's outer flanks, this ridge develops smoothly into the van Hove singularity, $A_{bulk}^0 \propto \left[(\omega - \omega_{bulk}^{min})\tau \right]^{-1/2}$, in the bulk LDOS at the bulk band bottom in the leads, $\omega_{bulk}^{min} = -\varepsilon_F$. We therefore call this LDOS structure a 'van Hove ridge'. Near the barrier's centre, its curvature causes the singularity to be smeared out on a scale set by Ω_x. This limits the amplitude of the van Hove ridge to $\max\left[A_j^0(\omega)\right] \propto \mathcal{O}(\Omega_x \tau_0)^{-1/2}$ and shifts it upwards in frequency relative to the band by $\mathcal{O}(\Omega_x)$ (Fig. 1f–h).

The van Hove ridge has a strong, $\tilde{V}_c$-dependent effect on numerous QPC properties. Near those spatial locations where the ridge intersects the chemical potential ($\omega = 0$), the LDOS is enhanced, thus amplifying the effects of interactions by $\mathcal{O}(\Omega_x \tau_0)^{-1/2}$ (which grows with QPC

[1]Center for NanoScience and Fakultät für Physik, Ludwig-Maximilians-Universität München, Geschwister-Scholl-Platz 1, 80539 München, Germany. [2]Arnold Sommerfeld Center for Theoretical Physics, Ludwig-Maximilians-Universität München, Theresienstrasse 37, D-80333 München, Germany. [3]Institut für Angewandte Physik, Universität Regensburg, D-93040 Regensburg, Germany. [4]Laboratory for Solid State Physics, ETH Zürich, CH-8093 Zürich, Switzerland.
*These authors contributed equally to this work.

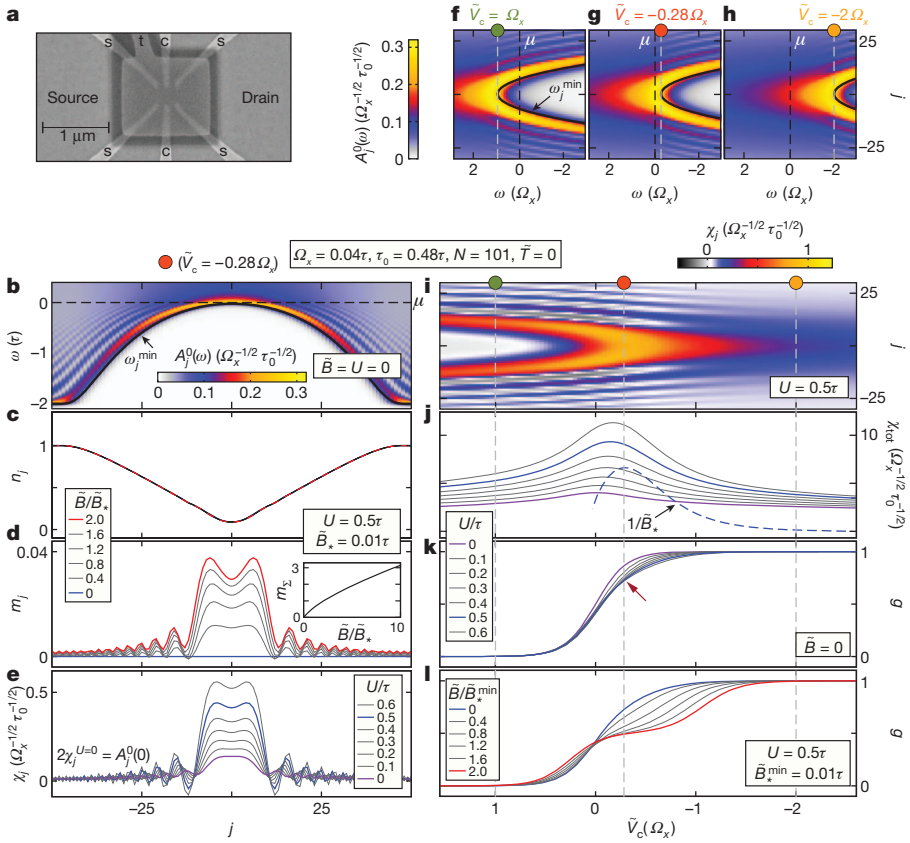

Figure 1 | Experimental set-up and model. **a**, Scanning electron microscope picture of the gate layout, featuring a top gate (t) at voltage V_t, two central gates (c) at voltage V_c and four side gates (s) at voltage V_s. Negative voltages V_c and V_s locally deplete the 2DES, which is 85 nm beneath the sample surface. Together with V_t, they induce a tunable electrostatic potential landscape in the 2DES. **b**, Barrier shape and LDOS. The bare ($U_j = 0$, $\tilde{B} = 0$) 1D LDOS per spin species, $A_j^0(\omega)$ (colour scale), as a function of energy, ω, and site index, j, for $\tilde{V}_c = -0.28\Omega_x$. The barrier shape is defined by the solid black line, showing the band bottom, ω_j^{min}. The LDOS vanishes exponentially rapidly below ω_j^{min} (Supplementary Fig. 11), and has a van Hove ridge (yellow–red) just above it, followed by Friedel oscillations (white fringes) at higher energies (up to $\omega \lesssim \tilde{V}_c$). **c**–**e**, Local properties of a sub-open QPC: FRG results for the sub-open barrier shown in **b**. **c**, **d**, The local density, n_j (**c**), and the magnetization, m_j (**d**), for several values of magnetic field, $\tilde{B}$. Inset of **d**, $m_\Sigma = \sum_{|j|\le 10} m_j$ as a function of $\tilde{B}$. **e**, The local spin susceptibility, χ_j, for several values of interaction strength, U. The shapes of m_j and χ_j are modulated by Friedel oscillations inherited from the bare LDOS (**b**), with locally varying wavelength, $\lambda \approx 1/n_j$. **f**–**l**, Changing barrier height. **f**–**h**, The bare LDOS, $A_j^0(\omega)$, for three successively lower barrier heights, $\tilde{V}_c/\Omega_x = 1$ (**f**), -0.28 (**g**) and -2 (**h**). The LDOS pattern is fixed with respect to $\tilde{V}_c$ (grey dashed lines) but shifts with respect to μ (black dashed lines). **i**–**l**, FRG results for the $\tilde{V}_c$ dependence of the local spin susceptibility, χ_j (colour scale), at fixed $U = 0.5\tau$ (**i**); the total spin susceptibility, $\chi_{tot} = \sum_j^{CCR} \chi_j$, for several U values (solid lines), and the inverse low-energy scale, $1/\tilde{B}_*$, for $U = 0.5\tau$ (dashed line) (**j**); the zero-temperature linear-response ($V_{sd} = 0$) conductance, $g = G/G_Q$, for several U values (at fixed $\tilde{B} = 0$) (**k**) and for several $\tilde{B}$ values (at fixed $U = 0.5\tau$) (**l**). For a large enough interaction, $U = 0.5\tau$, even for $\tilde{B} = \tilde{T} = \tilde{V}_{sd} = 0$ (blue lines in **k** and **l**), $g(\tilde{V}_c)$ has a shoulder (red arrow) at $g \approx 0.7$, the 0.7-anomaly. Three vertical dashed lines in **i**–**l** mark the three $\tilde{V}_c$ values used in **f**–**h**, as indicated by dots of matching colours.

length). In semiclassical terms, slow electrons feel interactions particularly strongly. When lowering the barrier top, $\tilde{V}_c$, to open the QPC, the van Hove ridge sweeps downwards (Fig. 1f–h); its interaction-amplifying effects are strongest in the $\tilde{V}_c$ regime where its apex, which has most weight, crosses μ. This happens for $0 \gtrsim \tilde{V}_c \gtrsim -\mathcal{O}(\Omega_x)$ (Fig. 1g), which, very importantly, encompasses the sub-open regime containing the 0.7-anomaly. Below, we show that the 0.7-anomaly and the zero-bias peak (ZBP) stem precisely from the amplification of interaction effects where the van Hove ridge intersects μ. The relevant implications are enhancements in the effective Hartree barrier governing elastic transmission, the spin susceptibility and the inelastic scattering rate, all of which lead to an anomalous reduction of g in the sub-open regime, especially for $T, B, V_{sd} > 0$.

Figure 1c–e illustrates several local properties, calculated at $\tilde{T} = 0$ using FRG, for the sub-open QPC barrier shown in Fig. 1b. We note four salient features, all intuitively expected. First, the local density, $n_j = \langle \hat{n}_{j\uparrow} + \hat{n}_{j\downarrow} \rangle$, is minimal at the barrier centre (Fig. 1c). Second, the local magnetization, $m_j = \langle \hat{n}_{j\uparrow} - \hat{n}_{j\downarrow} \rangle / 2$, vanishes at $B = 0$ (Fig. 1d, blue line); this reflects a physical assumption entailed in our calculations (Supplementary Information, section 6), namely that no spontaneous magnetization occurs, in contrast to the spontaneous spin splitting scenario advocated in refs 4, 8, 17. Third, m_j increases without saturation when $\tilde{B}$ becomes large (Fig. 1d, inset), indicating a smooth redistribution of spin, as expected for an open structure. Fourth, the local spin susceptibility, $\chi_j = (\partial m_j / \partial \tilde{B})_{\tilde{B}=0}$, is strongly enhanced with increasing U (Fig. 1e), because interactions amplify any field-induced spin imbalance.

The j dependence of χ_j is governed by that of $A_j^0(0)$ (in fact, $\chi_j^{U=0} = A_j^0(0)/2$), which is maximal near those sites where the van Hove ridge intersects μ. When $\tilde{V}_c$ is decreased through 0 (Figs 1f–h), these intersection points sweep out a parabolic arch in the $\tilde{V}_c - j$ plane, along which $\chi_j(\tilde{V}_c)$ (Fig. 1i, colour scale) is peaked, with most weight near the arch's apex. This leads to a corresponding peak in the total spin susceptibility, $\chi_{tot} = \sum_j^{CCR} \chi_j$, as a function of $\tilde{V}_c$ (Fig. 1j). This peak is strongly enhanced by increasing U (in accordance with the fourth feature above) and is located near the $\tilde{V}_c$ value where $g \approx 0.7$ (Fig. 1k). We will see further below that this peak strongly affects the $\tilde{B}$ dependence of the conductance (Fig. 1l).

Note that the spatial structure for $\chi_j(\tilde{V}_c)$ in Fig. 1i, namely two peaks merging into one as $\tilde{V}_c$ is lowered, is consistent with that, shown

in fig. 2b of ref. 14, for the density of spin-up electrons calculated using spin-density-functional theory, initialized in a small applied field to break spin symmetry. In ref. 14, the local maximum in the spin-up density was interpreted as evidence for a 'quasi-bound state' that was argued to host a spin-1/2 local moment; in contrast, features one and, especially, three above imply that our model yields no local moment.

Next we discuss the effect of the van Hove ridge on the conductance, $g(\tilde{V}_c)$, starting with its U dependence at $\tilde{B}=\tilde{T}=0$ (Fig. 1k). Increasing U skews the shape of the step in $g(\tilde{V}_c)$, which eventually develops a shoulder near $g\approx 0.7$ (red arrow). This shoulder develops because the increase in local density with decreasing $\tilde{V}_c$ is slightly nonlinear when the apex of the van Hove ridge drops past μ, causing a corresponding nonlinear upward shift in the effective Hartree barrier. For a parabolic barrier top, this occurs for $g\approx 0.7$. If the shape of the barrier top is changed to be non-parabolic, both the shape of the bare conductance step and the energy distance between the van Hove ridge apex and μ will change, which can cause the interaction-induced shoulder in g to shift away from 0.7. This explains the experimentally observed spread[6,12] of shoulders (that is, plateau values of the 0.7-anomaly) for $0.5 \lesssim g \lesssim 1$.

On increasing $\tilde{B}$ for fixed U and $\tilde{T}=0$ (Figs 1l and 2a), the shoulder in $g(\tilde{V}_c)$ becomes more pronounced, eventually developing into a spin-split plateau. Comparison of Fig. 2a with Fig. 2e shows that this development qualitatively agrees with experiment; the agreement was optimized by using U as fit parameter. Inspecting how the corresponding spin-resolved conductances, $g_\uparrow$ and $g_\downarrow$, change with $\tilde{B}$ (Fig. 2b), we note a strong asymmetry: although the bare barrier heights for spins $\uparrow$ and $\downarrow$ are shifted symmetrically by $-\tilde{B}/2$ and $\tilde{B}/2$, respectively, $g_\downarrow$ is decreased much more strongly than $g_\uparrow$ is increased. This is due to exchange interactions: increasing the spin-up density near the CCR centre (Fig. 1d) strongly raises the Hartree barrier, and more so for spin-down electrons than spin-up, owing to Pauli's exclusion principle. The consequences are most pronounced in the sub-open regime, owing to the van-Hove-ridge-induced peak in χ_{tot} there (Fig. 1j). We note, however, that $g_\uparrow = g_\downarrow$ at $\tilde{B}=0$, reflecting our above-mentioned assumption that no spontaneous spin splitting occurs.

Our FRG approach is limited to the case of zero temperature and zero source–drain voltage, for which no inelastic scattering occurs. To access qualitatively the effects of the latter at fixed U, we have instead used SOPT (Supplementary Information, section 7). Figure 2c–h shows a comparison of our SOPT results for the linear conductance, $g(\tilde{V}_c)$, calculated for several values of magnetic field, $\tilde{B}$, and temperature, $\tilde{T}=k_BT$, and our experimental data for $g(V_c)$. The measured conductance step shows a shoulder (Fig. 2e, f, red arrows) that becomes increasingly more pronounced with both increasing field, B (Fig. 2e), and increasing temperature, T (Fig. 2f), which is the hallmark of the 0.7-anomaly. Our perturbative calculations qualitatively reproduce both trends remarkably well. The only caveat is that the experimental curves in Fig. 2e, f show more pronounced shoulders than do the respective SOPT curves in Fig. 2c, d. This failure of SOPT to

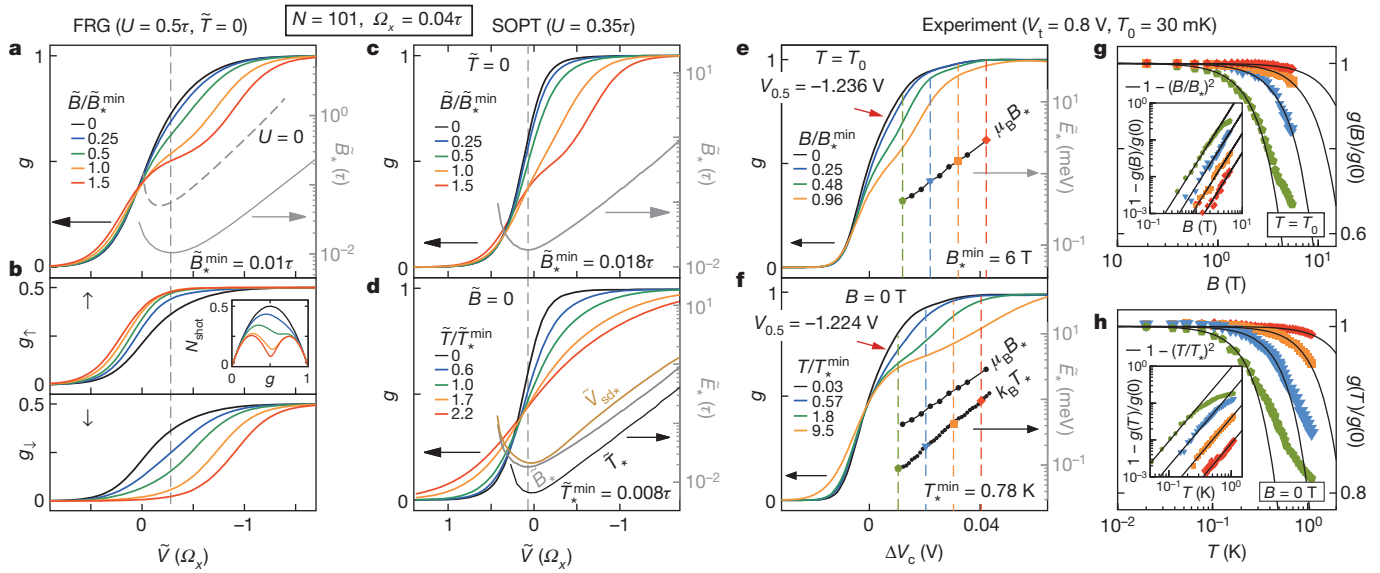

Figure 2 | Conductance: theory versus experiment. **a**, **b**, FRG results: the linear response conductance, $g(\tilde{V}_c, \tilde{B})$, of a QPC (**a**), and its spin-resolved components, $g_\uparrow$ and $g_\downarrow$ (**b**), plotted as functions of $\tilde{V}_c/\Omega_x$ for several values of $\tilde{B}$ at $\tilde{T}=0$ (but finite interaction U). The grey dashed and solid lines in **a** show the low-energy scale $\tilde{B}_*(\tilde{V}_c)$ for $U=0$ and $U=0.5$, respectively, plotted on the log-linear scale indicated on the right-hand axis (as also done in **c**–**f**). The small-field magnetoresponse in **a** is strongest when $\tilde{B}_*$ takes its smallest value, $\tilde{B}_*^{min}$ (vertical dashed lines). Inset of **b**, the shot noise factor, $N_{shot} = \sum_\sigma g_\sigma(1-g_\sigma)/2$, plotted as function of g. Its asymmetric development with $\tilde{B}$, which reflects that of $g_\uparrow$ and $g_\downarrow$, agrees qualitatively with experiment (see fig. 4d of ref. 7). **c**, **d**, SOPT results: $g(\tilde{V}_c, \tilde{B})$ at $\tilde{T}=0$ for several values of $\tilde{B}$ (**c**) and $g(\tilde{V}_c, \tilde{T})$ at $\tilde{B}=0$ for several values of $\tilde{T}$ (**d**), both plotted as functions of $\tilde{V}_c/\Omega_x$. The low-energy scale $\tilde{B}_*(\tilde{V}_c)$ is shown as a thin grey line in **c** and repeated in **d**; $\tilde{T}_*(\tilde{V}_c)$ and $\tilde{V}_{sd*}(\tilde{V}_c)$ are respectively shown as thin black and brown lines in **d**. The vertical dashed line indicates where $\tilde{B}_*$ takes its minimal value, $\tilde{B}_*^{min}$. For $\tilde{V}_c$ values below this dashed line, the lines for $\tilde{B}_*$, $\tilde{T}_*$ and $\tilde{V}_{sd*}$ in **d** are nearly straight on the log-linear scale, implying the behaviour summarized by equation (3), and are nearly parallel to each other, implying that the ratios $\tilde{B}_*/\tilde{T}_*$ and $\tilde{V}_{sd*}/\tilde{T}_*$ are essentially independent of $\tilde{V}_c$ there. **e**, **f**, Experiments—pinch-off curves. **e**, $g(V_c)$ measured at a low 2DES temperature, T_0, for various magnetic fields parallel to the 2DES, plotted as a function of $\Delta V_c = V_c - V_{0.5}$, where $V_{0.5}$ is the gate voltage for which the conductance at $B=0$ and $T=T_0$ is $g(V_{0.5})=0.5$. **f**, Analogous to **e**, but for $B=0$ and various temperatures T. Colours in **e** and **f** are chosen to provide comparability with theory curves in **a**, **c** and **d** (with the correspondence $|e|\Delta V_c \propto -\tilde{V}_c$). **g**, **h**, Experiments—Fermi-liquid behaviour: $g(B)/g(0)$ as function of B at temperature T_0 (**g**), and $g(T)/g(T_0)$ as function of T at $B=0$ (**h**), shown on log-linear scales (insets show their differences from unity on log-log scales) to emphasize small values of B and T. Coloured symbols distinguish data taken at different fixed V_c values, indicated by dashed lines of corresponding colour in **e** and **f**. The quadratic B and T dependences observed in **g** and **h** for each fixed V_c value confirm equation (2) and were used to determine the corresponding scales $B_*(V_c)$ and $T_*(V_c)$. (Black lines in **g** and **h** show $1-(B/B_*)^2$ and $1-(T/T_*)^2$, respectively.) The resulting energies, $E_* = \mu_B B_*(V_c)$ and $E_* = k_B T_*(V_c)$, are shown as functions of V_c in **e** (for B_*) and **f** (for both B_* and T_*) on a log-linear scale. The shape of these measured functions agrees qualitatively with the SOPT predictions in **c** and **d**, confirming the nearly exponential $\tilde{V}_c$ dependences and the nearly V_c-independent B_*/T_* ratio, discussed above. (For additional data, similar to that in **g** and **h**, see Supplementary Information, section 2B.)

produce real shoulders is present both in the low-field dependence at low temperature (compare Fig. 2e with Fig. 2c; the former, but not the latter, shows a weak shoulder even at zero field) and in the temperature dependence at zero field (compare Fig. 2f and Fig. 2d). In contrast, the more powerful FRG approach does reproduce the weak shoulder even for $\tilde{B}=\tilde{T}=0$, as discussed above; compare the black $g(\tilde{V}_c)$ curves in Fig. 2a (FRG) and Fig. 2c (SOPT). (That the latter curve, in contrast to the former, lies above its non-interacting version, $g^0(\tilde{V}_c)$, is an artefact of SOPT; see Supplementary Information, section 7D.)

We next focus on the limit of small energies $\tilde{B}$, $\tilde{T}$ and $\tilde{V}_{sd}$. Here our SOPT calculations yield three predictions, enumerated below, that are all consistent with our measurements. First, for fixed $\tilde{V}_c$, the leading dependence of the nonlinear conductance, $g_{nl}=(dI/d\tilde{V}_{sd})/G_Q$, on $\tilde{B}$, $\tilde{T}$ and $\tilde{V}_{sd}$ is predicted to be quadratic, as confirmed by the measured data in Figs 2g, h and 3a. This implies an expansion of the form

$$\frac{g_{nl}(\tilde{B},\,\tilde{T},\,\tilde{V}_{sd})}{g_{nl}(0,\,0,\,0)} \approx 1-\frac{\tilde{B}^2}{\tilde{B}_*^2}-\frac{\tilde{T}^2}{\tilde{T}_*^2}-\frac{\tilde{V}_{sd}^2}{\tilde{V}_{sd*}^2} \qquad (2)$$

for $\tilde{B}/\tilde{B}_*$, $\tilde{T}/\tilde{T}_*$, $\tilde{V}_{sd}/\tilde{V}_{sd*}\ll 1$, where $\tilde{B}_*$, $\tilde{T}_*$ and $\tilde{V}_{sd*}$ are $\tilde{V}_c$-dependent crossover scales that govern the 'strength' of the 0.7-anomaly for $U\neq 0$: the smaller these scales, the stronger the dependence on $\tilde{B}$, $\tilde{T}$ and $\tilde{V}_{sd}$ for a given $\tilde{V}_c$. Our SOPT results for these crossover scales are shown as thin lines on log-linear scales in Fig. 2c and Fig. 2d, respectively. Second, in that part of the sub-open regime where $g_{nl}(0,\,0,\,0)\approx 1$, they all depend exponentially on $\tilde{V}_c$:

$$\tilde{B}_*,\ \tilde{T}_*,\ \tilde{V}_{sd*} \propto \exp(-\pi\tilde{V}_c/\Omega_x) \qquad (3)$$

Third, and again for $g_{nl}(0,\,0,\,0)\approx 1$, the ratios $\tilde{B}_*/\tilde{T}_*$ and $\tilde{V}_{sd*}/\tilde{T}_*$ are essentially independent of $\tilde{V}_c$ (Supplementary Fig. 4). Remarkably, both the second and third predictions are confirmed by our experimental results (Fig. 2e for B_*, Fig. 2f for T_* and Supplementary Fig. 3 for V_{sd*}). The behaviour predicted by equation (3) for $\tilde{T}_*$ is also in accord with previous experiments[6] and with a perturbative treatment of interactions using Wentzel–Kramers–Brillouin wavefunctions[21]. Remarkably, the exponential $\tilde{V}_c$ dependence of the crossover scales stated in equation (3) can be understood from a non-interacting ($U=0$) theory, by using the bare transmission probability[3]

$$T_\sigma^0(\omega)=\left[e^{-2\pi(\omega-\tilde{V}_c+\sigma\tilde{B}/2)/\Omega_x}+1\right]^{-1} \qquad (4)$$

in the Landauer–Büttiker formula. A detailed analysis (Supplementary Information, section 5) shows that the crossover scales experience a further exponential reduction with increasing effective interaction strength, $U/\sqrt{\Omega_x\tau_0}$.

When plotted as a function of $\tilde{V}_c$, $1/\tilde{B}_*$ has a peak in the sub-open regime just before the onset of the exponential dependence of equation (3) (Fig. 1j). This peak is roughly similar in shape and position to that in $\chi_{tot}(\tilde{V}_c)$ (compare dashed and solid blue lines in Fig. 1j), except that the latter has a finite offset, reflecting the non-zero spin susceptibility of an open QPC. Thus, we predict, fourth, that $1/\tilde{B}_*$, which characterizes the strength of the low-field magnetoconductance, is roughly proportional to the spin susceptibility, χ_{tot}, of the CCR.

Next we address the remarkable experimental fact[6] that many low-energy properties of the 0.7-anomaly (including our first and third predictions) are similar to those seen in transport through a Kondo quantum dot (KQD). This led to the proposal[13,14] that a QPC harbours

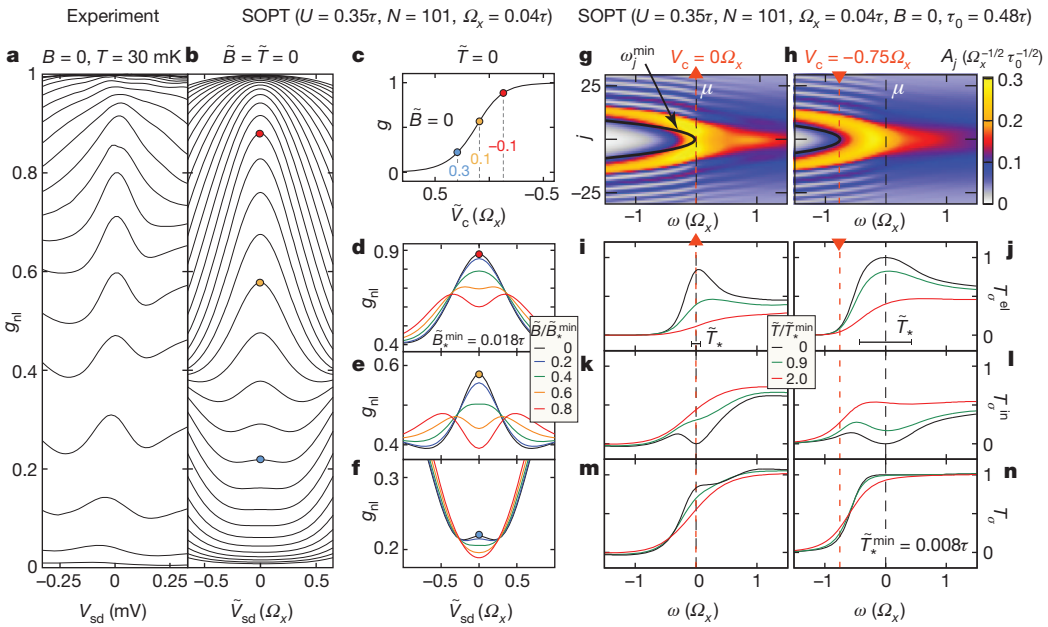

Figure 3 | Finite excitation energies. **a**–**f**, Zero-bias peak. **a**, Experimental data for the nonlinear conductance, g_{nl}, as a function of source–drain voltage, measured for several V_c values at a fixed low temperature and zero field. **b**, Keldysh SOPT results for $g_{nl}(\tilde{V}_{sd})$ for several $\tilde{V}_c$ values at $\tilde{T}=\tilde{B}=0$, showing qualitative agreement with **a**. **c**, The linear-response conductance, $g=g_{nl}(\tilde{V}_{sd}=0)$, as a function of $\tilde{V}_c$. **d**–**f**, $g_{nl}(\tilde{V}_{sd})$ as in **b**, but for three different $\tilde{V}_c$ values (compare colour-matched dots in **c** and **b**) and five different magnetic field values in each panel. Increasing $\tilde{B}$ causes the ZBP to split into two subpeaks once $\tilde{B}\gtrsim\tilde{B}_*$; the splitting is therefore most pronounced in **e**, for which $\tilde{B}_*$ is smallest. A detailed discussion of the ZBP, including its T dependence, will be published elsewhere. Here we would like to point out the qualitative agreement of **d**–**f** with published data; see, for example, fig. 2d of ref. 6. **g**, **h**, Interacting LDOS: $A_j(\omega)$, calculated using SOPT, shown for two fixed gate voltage values, $\tilde{V}_c/\Omega_x=0$ (**g**) and -0.75 (**h**) (red dashed lines). **i**–**n**, Equilibrium transmission probabilities: the corresponding elastic, inelastic and total transmission probabilities, T_σ^{el} (**i**, **j**), T_σ^{in} (**k**, **l**) and T_σ (**m**, **n**), calculated using SOPT and shown as functions of energy, ω, for three different temperatures. At $\tilde{T}=0$ (black curves) $T_\sigma^{in}(\omega)$ vanishes at $\omega=0$, where there is no phase space for inelastic scattering. However, it increases as ω changes from zero, causing a corresponding reduction in the elastic transmission for $\omega\neq 0$, such that $T_\sigma^{el}(\omega)$ has a narrow 'low-energy peak' around $\omega=0$. On increasing the temperature, the probability of inelastic scattering increases, causing the minimum in $T_\sigma^{in}(\omega)$ and the peak in $T_\sigma^{el}(\omega)$ to be smeared out. This leads to a net $\tilde{T}$-induced reduction in the total transmission, $T_\sigma(\omega)$ near $\omega=0$, causing a corresponding reduction in the conductance (Fig. 2d, f). This reduction is stronger for $\tilde{V}_c/\Omega_x=0$ (**m**) than for $\tilde{V}_c/\Omega_x=-0.75$ (**n**), because the probability of electron–hole pair creation during inelastic scattering is largest when apex of the van Hove ridge lies closest to μ (compare **g** and **h**).

a quasi-bound state, whose local moment gives rise to the Kondo effect. In contrast, our van-Hove-ridge scenario fully explains the 0.7-anomaly without invoking the Kondo effect. In particular, we find no indications that a smooth parabolic barrier hosts a discrete, localized spin (compare with the third feature above), and no Kondo effect/0.7-anomaly similarities (experimentally or theoretically) at high energies ($\gtrsim \tilde{B}_*$), where the Kondo effect is governed by an unscreened local moment. Nevertheless, the two phenomena do have similar low-energy behaviour. This is because both involve a spin-singlet ground state featuring spatially confined spin fluctuations. For a KQD they result from screening of the localized spin, whereas for a QPC they result from the extended structure of the van Hove ridge (Fig. 1i); but this distinction, which is important on short length scales (high energies), does not matter on long ones (low energies). These spin fluctuations are characterized by exponentially small energy scales, the Kondo temperature for a KQD, and $\tilde{T}_*$ for a QPC, both scaling inversely with the local spin susceptibility (for a QPC, this follows from prediction four). For a KQD, the local spin fluctuations can be described by Nozières–Fermi-liquid theory[27,28] in terms of scattering phase shifts, which determine its low-energy properties. Because a QPC, like a KQD, harbours spatially confined spin fluctuations, a similar Nozières–Fermi-liquid framework applies, explaining why its low-energy transport properties are similar to those of a KQD.

We next study finite excitation energies ($\tilde{T}$, $\tilde{V}_{sd} > 0$), where inelastic scattering becomes important (Fig. 3). We begin by considering the nonlinear differential conductance, g_{nl}, as a function of source–drain voltage, V_{sd}. Experimentally, g_{nl} shows a narrow peak at $V_{sd} = 0$ (Fig. 3a; see also refs 6, 9, 10). This ZBP appears strongest in the sub-open regime, but remains visible even very close to pinch off[10] ($g \to 0$). It splits with increasing field once B exceeds a V_c-dependent crossover value that is smallest when $g \approx 0.7$ (see fig. 2d of ref. 6). Remarkably, our model, treated using Keldysh SOPT (Supplementary Information, section 7B), yields a ZBP (Fig. 3b, d–f) that qualitatively reproduces this behaviour. In the sub-open regime ($0.5 \lesssim g \lesssim 0.9$), a ZBP arises even without interaction (this follows from equation (4)), but interactions modify it in two ways (Supplementary Information, section 7C): a finite V_{sd} causes a net charge enhancement at the barrier, resulting in a reduction of transmission due to Coulomb repulsion; and opens up a finite phase space for inelastic backscattering. Both effects strongly depend on the LDOS near μ (Fig. 3g, h), and are thus strongest when the apex of the van Hove ridge lies near μ (as in Figs 3g and 1g). However, the van Hove ridge intersects μ also for $g < 0.5$ (as in Fig. 1f), which explains why a ZBP is experimentally observed even close to pinch off[10].

The two modification mechanisms just discussed also apply to the case of increasing temperature. To highlight the role of inelastic scattering, we now discuss (for $\tilde{B} = \tilde{V}_{sd} = 0$) the transmission probability $T_\sigma(\omega) = T_\sigma^{el}(\omega) + T_\sigma^{in}(\omega)$, written as the sum of elastic and inelastic contributions corresponding respectively to transmission without or with the creation of electron–hole pairs (see Supplementary Information, section 7A, for their precise definition). Figure 3i–n shows examples of these quantities. With increasing temperature, the probability for inelastic scattering increases, causing $T_\sigma^{in}(\omega)$ to increase (Fig. 3k, l) and $T_\sigma^{el}(\omega)$ to decrease (Fig. 3i, j). This leads to a net temperature-induced reduction in the total transmission, $T_\sigma(\omega)$ (Fig. 3m, n), near $\omega = 0$, causing a corresponding reduction in the conductance (Fig. 2d, f). Importantly, this reduction is V_c dependent: it is strongest when the apex of the van Hove ridge lies near μ (as in Fig. 3m) and decreases away from this point (as in Fig. 3n), because the probability for electron–hole pair creation during inelastic scattering increases with the LDOS near μ. The fact that $T_\sigma(\omega)$ acquires a non-trivial, interaction-induced dependence on $\tilde{T}$ in the sub-open regime is consistent with the fact that near $g \approx 0.7$ the measured thermopower violates the Mott relation[5], which is based on the assumption of non-interacting electrons.

Finally, we note that we have studied the magnetic field dependence of the transconductance, dG/dV_c, both experimentally and by using FRG. We obtain excellent qualitative agreement between experiment and theory, showing that such measurements can be understood without invoking spontaneous spin polarization, as is often advocated to explain them[4,8,17]. A detailed analysis (Supplementary Information, section 2C, and Supplementary Fig. 5) establishes that the g factor is enhanced significantly by interactions, and that interaction strength can be tuned experimentally using a top gate.

We have presented detailed microscopic calculations that qualitatively reproduce the full phenomenology of the 0.7-anomaly. We argued that a van Hove ridge in the LDOS, combined with interactions, provides a natural explanation for the anomalous behaviour of the conductance of a sub-open ($g \gtrsim 0.5$) QPC. The experimentally observed[6] similarities between the 0.7-anomaly and the Kondo effect at low energies arise because both phenomena involve spatially localized spin fluctuations; at high energies, the similarities cease. We verified our Fermi-liquid predictions for the QPC conductance by systematic measurement of the conductance as a function of V_c, B and T. Strikingly, we demonstrated that the zero-bias peak in a QPC arises from the interplay of interactions and geometry. By implication, anomalous zero-bias behaviour might also arise in other systems involving interacting electrons traversing 1D low-density regions with slowly varying spatial inhomogeneities, such as the gated nanowires being studied in the search for Majorana fermions[29].

METHODS SUMMARY

The nanostructure is laterally defined in a 2DES located 85 nm beneath the surface of a GaAs/AlGaAs heterostructure. The low-temperature carrier density and mobility are $1.9 \times 10^{11}\,cm^{-2}$ and $1.2 \times 10^6\,cm^2\,V^{-1}\,s^{-1}$, respectively. Electron-beam lithography was used to create the Ti/Au gates. The top gate is electrically insulated from the others by cross-linked poly(methyl methacrylate). Perfect alignment of magnetic fields parallel to the 2DES and the 1D channel defining the QPC was ensured by using a two-axis magnet and was controlled by magnetotransport measurements. We used a dilution refrigerator and reached electron temperatures as low as $T_{2DES} \approx 30$ mK.

Our most accurate theoretical results were obtained by using FRG[24–26] to calculate $T = 0$ properties. FRG amounts to doing renormalization-group-enhanced perturbation theory in the interaction U. In setting up our FRG flow equations, we made two approximations, both exact to second order in U: we truncated the infinite hierarchy of flow equations by neglecting the flow of the three-particle vertex; and we set to zero all components of the two-particle vertex that are not already generated to second order in the interaction (coupled-ladder approximation).

To access the effects of inelastic scattering for $\tilde{T} > 0$ or $\tilde{V}_{sd} > 0$ at fixed U, we used SOPT: we dressed bare Green's functions by evaluating the self-energy perturbatively to second order in the interaction. For $\tilde{V}_{sd} = 0$, we calculated the linear conductance following the strategy in ref. 23, generalized to $\tilde{B} \neq 0$ and broken electron–hole symmetry. For $\tilde{V}_{sd} > 0$, we calculated the nonlinear conductance, $g_{nl} = (dI/d\tilde{V}_{sd})/G_Q$, using the Meir–Wingreen formula for the current (equation (6) of ref. 30).

Received 16 November 2012; accepted 26 June 2013.
Published online 28 August 2013.

1. van Wees, B. J. *et al.* Quantized conductance of point contacts in a two-dimensional electron gas. *Phys. Rev. Lett.* **60,** 848–850 (1988).
2. Wharam, D. A. *et al.* One-dimensional transport and the quantisation of the ballistic resistance. *J. Phys. C* **21,** L209–L214 (1988).
3. Büttiker, M. Quantized transmission of a saddle-point constriction. *Phys. Rev. B* **41,** 7906(R) (1990).
4. Thomas, K. J. *et al.* Possible spin polarization in a one-dimensional electron gas. *Phys. Rev. Lett.* **77,** 135–138 (1996).
5. Appleyard, N. J. *et al.* Direction-resolved transport and possible many-body effects in one-dimensional thermopower. *Phys. Rev. B* **62,** R16275–R16278 (2000).
6. Cronenwett, S. M. *et al.* Low-temperature fate of the 0.7 structure in a point contact: a Kondo-like correlated state in an open system. *Phys. Rev. Lett.* **88,** 226805 (2002).
7. DiCarlo, L. *et al.* Shot-noise signatures of 0.7 structure and spin in a quantum point contact. *Phys. Rev. Lett.* **97,** 036810 (2006).
8. Koop, E. J. *et al.* The influence of device geometry on many-body effects in quantum point contacts: signatures of the 0.7-anomaly, exchange and Kondo. *J. Supercond. Nov. Magn.* **20,** 433–441 (2007).
9. Sarkozy, S. *et al.* Zero-bias anomaly in quantum wires. *Phys. Rev. B* **79,** 161307R (2009).
10. Ren, Y. *et al.* Zero-bias anomaly of quantum point contacts in the low-conductance limit. *Phys. Rev. B* **82,** 045313 (2010).

11. Micolich, A. P. What lurks below the last plateau: experimental studies of the $0.7 \times 2e^2/h$ conductance anomaly in one-dimensional systems. *J. Phys. Condens. Matter* **23,** 443201 (2011).
12. Burke, A. *et al.* Extreme sensitivity of the spin-splitting and 0.7 anomaly to confining potential in one-dimensional nanoelectronic devices. *Nano Lett.* **12,** 4495–4502 (2012).
13. Meir, Y., Hirose, K. & Wingreen, N. S. Kondo model for the 0.7 anomaly in transport through a quantum point contact. *Phys. Rev. Lett.* **89,** 196802 (2002).
14. Rejec, T. & Meir, Y. Magnetic impurity formation in quantum point contacts. *Nature* **442,** 900–903 (2006).
15. Ihnatsenka, S. & Zozoulenko, I. V. Conductance of a quantum point contact based on spin density-functional theory. *Phys. Rev. B* **76,** 045338 (2007).
16. Matveev, K. A. Conductance of a quantum wire at low electron density. *Phys. Rev. B* **70,** 245319 (2004).
17. Reilly, D. J. Phenomenological model for the 0.7 conductance feature in quantum wires. *Phys. Rev. B* **72,** 033309 (2005).
18. Sloggett, C. Milstein, A. I. & Sushkov, O. P. Correlated electron current and temperature dependence of the conductance of a quantum point contact. *Eur. Phys. J. B* **61,** 427–432 (2008).
19. Aryanpour, K. & Han, J. E. Ferromagnetic spin coupling as the origin of 0.7 anomaly in quantum point contacts. *Phys. Rev. Lett.* **102,** 056805 (2009).
20. Güçlü, A. D. *et al.* Localization in an inhomogeneous quantum wire. *Phys. Rev. B* **80,** 201302(R) (2009).
21. Lunde, A. M. *et al.* Electron-electron interaction effects in quantum point contacts. *New J. Phys.* **11,** 023031 (2009).
22. Goldhaber-Gordon, D. *et al.* Kondo effect in a single-electron transistor. *Nature* **391,** 156–159 (1998).
23. Oguri, A. Transmission probability for interacting electrons connected to reservoirs. *J. Phys. Soc. Jpn* **70,** 2666–2681 (2001).
24. Andergassen, S. *et al.* Renormalization-group analysis of the one-dimensional extended Hubbard model with a single impurity. *Phys. Rev. B* **73,** 045125 (2006).
25. Karrasch, C., Enss, T. & Meden, V. Functional renormalization group approach to transport through correlated quantum dots. *Phys. Rev. B* **73,** 235337 (2006).
26. Metzner, W. *et al.* Functional renormalization group approach to correlated fermion systems. *Rev. Mod. Phys.* **84,** 299–352 (2012).
27. Nozières, P. A ''fermi-liquid'' description of the Kondo problem at low temperatures. *J. Low Temp. Phys.* **17,** 31–42 (1974).
28. Glazman, L&. Pustilnik, M. in *Nanophysics: Coherence and Transport* (eds Bouchiat, H. *et al.*) 427–478 (Elsevier, 2005).
29. Mourik, V. *et al.* Signatures of Majorana fermions in hybrid superconductor-semiconductor nanowire devices. *Science* **336,** 1003–1007 (2012).
30. Meir, Y. & Wingreen, N. S. Landauer formula for the current through an interacting electron region. *Phys. Rev. Lett.* **68,** 2512–2515 (1992).

Supplementary Information is available in the online version of the paper.

Acknowledgements We thank B. Altshuler, P. Brouwer, R. Egger, J. Folk, L. Glazman, V. Golovach, A. Hamilton, A. Högele, Y. Imry, M. Kiselev, J. Kotthaus, D. Logan, D. Loss, C. Marcus, Y. Meir, H. Monien, M. Pepper, M. Pustilnik, A. Rosch, K. Schönhammer, B. Spivak and A. Yacoby for discussions, and, in particular, S. Andergassen, C. Honerkamp, S. Jakobs, C. Karrasch, V. Meden, M. Pletyukhov and H. Schoeller for FRG-related help and advice. We acknowledge support from the DFG through SFB-631, SFB-TR12, De730/3-2, De730/4-1, De730/4-2, De730/4-3, HO 4687/1-3, LU819/4-1 and the Cluster of Excellence Nanosystems Initiative Munich; from the Center for NanoScience; and from the US National Science Foundation under grant no. NSF PHY05-51164. S.L. acknowledges support through a Heisenberg fellowship of the DFG.

Author Contributions J.v.D. and S.L. coordinated the project: J.v.D. initiated and supervised the theoretical work, and S.L. planned and supervised the experiments and their analysis. F.B. and J.H. carried out the calculations using FRG, and J.H., F.B. and B.B. carried out the calculations using perturbation theory. D.S. and W.W. provided the wafer material, and D.B. fabricated the nanostructure. E.S., D.B., D.T. and S.L. carried out the measurements, and E.S., D.B., F.B. and J.H. carried out the experimental data analysis. J.H. and F.B. prepared the figures, and J.v.D., S.L., F.B., J.H. and E.S. wrote the paper.

Author Information Reprints and permissions information is available at www.nature.com/reprints. The authors declare no competing financial interests. Readers are welcome to comment on the online version of the paper. Correspondence and requests for materials should be addressed to J.v.D. (vondelft@lmu.de) or S.L. (ludwig@lmu.de).

SUPPLEMENTARY INFORMATION

doi:10.1038/nature12421

Contents

S-1. OVERVIEW

The following supplementary material provides additional information related to various aspects of the main article. Its sections can be read independently and in arbitrary order. They are grouped into two parts: Part I (Secs. S-2 and S-3) is devoted to experiments and their comparison with theory; Part II (Secs. S-4 to S-7 C) provides further theoretical details.

Section S-2 gives supplementary information about our measurements discussed in the main article. Section S-2 A describes the experimental setup. In Sec. S-2 B we present the raw data on which the experimental tests of Fermi liquid predictions in the main article are based, together with corresponding results obtained by the functional renormalization group (fRG) (Fig. S2). We also present additional data (Fig. S3) illustrating the gate-voltage dependence of the crossover scales in magnetic field, temperature and source-drain-voltage, B_*, T_* and $V_{\rm sd*}$, together with corresponding calculations using second-order perturbation theory (SOPT). Sec. S-2 C explains in detail how the effective g-factor $g_{\rm ss}$ is extracted from the transconductance for large fields (Fig. S5), and offers some comments on the much-discussed scenario that the 0.7-anomaly is due to spontaneous spin polarization in the QPC region.

Sec. S-3 presents further $T = 0$ fRG results (Figs. S6 and S7) that demonstrate qualitative agreement with shot noise and compressibility measurements by other groups. These fRG results, and those in Sec. S-5, were calculated using "static" fRG, which differs from the "dynamic" fRG approach used in the main text by neglecting the frequency dependence of the self-energy and all vertices (see Sec. S-6 F). Static fRG yields results that are very similar to those of dynamic fRG (see Fig. S15), while being numerically cheaper by a factor $\sim 10^3$.

Section S-4 describes our theoretical model in detail. We have used two slightly different parametrizations of the QPC barrier shape, called "model I" and "model II", which both describe parabolic barrier tops and hence give essentially equivalent results for QPC properties. They are defined in Secs. S-4 B and S-4 D, respectively (the main article uses only model II). Sections S-4 C and S-4 E explain how the effects of geometry are encoded in the bare local density of states (LDOS), focussing in particular on the van Hove ridge of a QPC, which is key to understanding the 0.7-anomaly.

Section S-5 focuses on the low-energy scale $\widetilde{B}_*(\widetilde{V}_{\rm c})$ for a QPC: it shows that its exponential $\widetilde{V}_{\rm c}$-dependence has a purely geometric origin, and that the strength of its U-dependence likewise depends on the shape of the barrier.

Sections S-6 and S-7 discuss details of the two theoretical methods used here to incorporate the effect of interaction: the functional Renormalization Group (fRG) and second order perturbation theory (SOPT), respectively. Section S-7 C is devoted to a detailed description of our

SOPT results for finite temperature or finite source-drain voltage, offering a summary of the features of the 0.7-anomaly which SOPT does or does not capture qualitatively. Finally, Sec. S-7 D discusses an SOPT artefact that arises with increasing U.

Equation and figure and section numbers from the main article or the supplementary material are prefaced below by A (for "article") vs. S (for "supplementary"), respectively, e. g. Eq. (A1), Fig. A1**f**, Sec. A-2 vs. Eq. (S1), Fig. S2**b**, Sec. S-4. As in the main article, we use tildes to distinguish theory parameters from those used in experiment, writing, e. g. $\widetilde{T} = k_{\rm B}T$, $\widetilde{B} = |g_{\rm el}|\mu_{\rm B}B$, and $\widetilde{V}_{\rm c,s} \propto -|e|V_{\rm c,s}$.

PART I: EXPERIMENT VS. THEORY

S-2. OUR EXPERIMENTAL DATA VS. THEORY

A. Experimental setup

The gate layout of our sample, shown in Fig. A1**a** for a dummy sample whose layout is identical to that of the actual sample, provides a particularly high tunability of the central constriction region (CCR). The gates can be used to laterally define either a quantum point contact (QPC) or a quantum dot (QD) in the two-dimensional electron system (2DES) 85 nm beneath the surface of a GaAs/AlGaAs heterostructure. In this work, we focus exclusively on the QPC geometry; a study of the crossover from QD to QPC will be published elsewhere.[1] More information about the experimental conditions is provided in the methods summary section of the main article.

In our two-terminal transport measurements the current $I_{\rm sd}$ flows through the nanostructure between ohmic contacts marked by "source" and "drain" in Fig. A1**a**, and we measure the differential conductance $g = (\mathrm{d}I_{\rm sd}/\mathrm{d}V_{\rm sd})/G_{\rm Q}$ (henceforth simply called conductance) using lockin methods. In all measurements discussed in this paper we apply a negative voltage $V_{\rm c}$ to both center gates and a negative voltage $V_{\rm s}$ to all four side gates. This depletes the 2DES in the vicinity of the gates, so that propagation between source and drain through the CCR is confined to a narrow channel, leading to the quantization of transverse modes. (Further variations of individual gate voltages allow additional control of the lateral symmetry properties of the CCR, but such studies are not included in this work.) Moreover, our sample also contains a global top gate (see Fig. A1**a**).

In this work, we focus on gate voltages such that transport is carried solely by the first subband, corresponding to the lowest transverse mode. Its behavior can be described by a one-dimensional effective model for motion in the longitudinal (say x-) direction. The shape of the effective potential $V_{\rm eff}(x)$ in the CCR can be changed by tuning $V_{\rm c}$, $V_{\rm s}$ and $V_{\rm t}$. Increasing the top gate voltage $V_{\rm t}$ increases the carrier density of the 2DES in the contacts of the CCR and hence the chemical potential, thereby deepening (w. r. t. μ) the trenches between the regions of high potential energy caused by the central and side gates[4]. This changes not only the shape of $V_{\rm eff}(x)$, but also causes the transverse wave functions to be more localized and hence increases the effective one-dimensional on-site interaction strength U within the CCR. For future reference, we summarize this trend as follows:

The effective interaction strength U can be increased experimentally by increasing $V_{\rm t}$. (S1)

For a QPC geometry, increasing $V_{\rm t}$ has an additional effect: due to the deepened trenches in the potential landscape, the energy spacing of the transverse eigenmodes increases, resulting in an increased subband spacing[5]. This trend is demonstrated in Fig. S1 based on measured pinch-off curves of our QPC for varying top-gate voltages. It can be used, in principle, to quantify the $V_{\rm t}$-induced increase in U in terms of the $V_{\rm t}$-induced increase in subband spacing[6], as will be elaborated in Sec. S-5 C below.

B. Fermi liquid properties

Figs. S2**b** and S2**c** show the raw experimental data for the measured linear response conductance of our QPC (a constant lead resistance has already been subtracted for all data). They show how the pinch-off curves depend on magnetic field and temperature, respectively. For comparison, Fig. S2**a** shows corresponding fRG data calculated for zero temperature as a function of the magnetic field $\widetilde{B}$. Both calculated and measured data exhibit the expected transition from a weak kink at $g \simeq 0.7$ at small T and B to a pronounced 0.7-anomaly if either magnetic field (measured and calculated data) or temperature (measured data) is substantially increased.

The raw data from Figs. S2**b** and S2**c** underly the experimental results presented in Figs. A2**e-h** of the main article. Figs. S3**a-d** shows additional data sets, plotted in the same way as in Figs. A2**g** and A2**h**, but displaying data not shown there for lack of space. Together, these data confirm the Fermi-liquid behavior expected theoretically for sufficiently low fields and temperatures: Figures A2**g** and S3**a**,**b** show that at sufficiently low temperatures, $T_0 \ll T_*$ (in our measurements $T_0 = T_{\rm 2DES} \simeq 30\,\mathrm{mK}$), the leading magnetic field-dependence of the linear conductance is quadratic,

$$g(B)/g(0) = 1 - (B/B_*)^2\,, \qquad B \ll B_*\,, \tag{S2a}$$

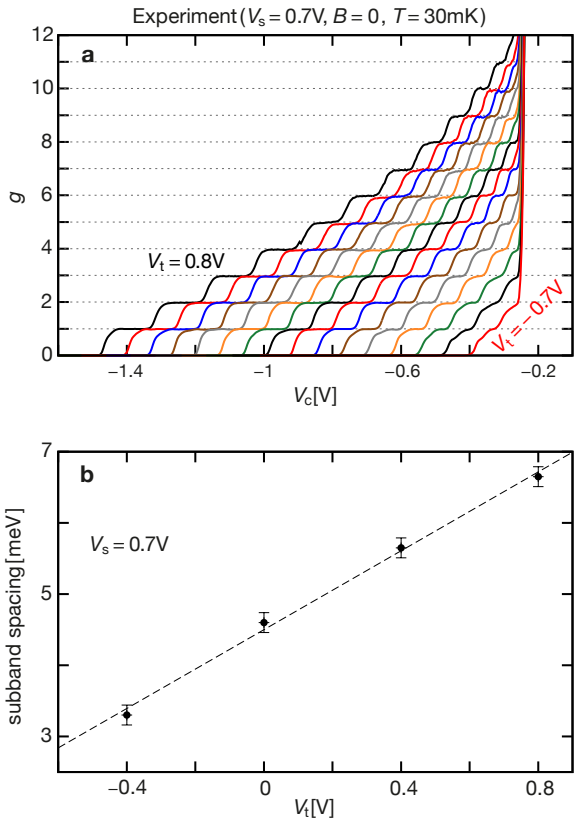

Figure S1: **V_t-dependence of subband spacing. a**, Measured pinch-off curves $g(V_c)$ of our QPC for a series of top-gate voltages in the range $-0.7\,\mathrm{V} \le V_t \le 0.8\,\mathrm{V}$. As V_t is decreased the carrier density also becomes smaller which, in turn, results in a larger pinch-off voltage V_c and, clearly, in more narrow plateaus at integer g. The steep increase of $g(V_c)$ independent of V_t at $V_c \simeq -0.25\,\mathrm{V}$ indicates the transition from 1D to 2D transport as the 2DES directly below the center gates is no longer depleted. **b**, Energy spacing between the lowest two 1D subbands as a function of V_t. The data points were evaluated from finite-V_{sd} measurements (raw data[2] not shown), using a procedure described in Refs. 2,3, whose uncertainty is indicated by the error bars. The resulting subband spacing is approximately proportional to the width of the first conductance plateau in **a**. As expected from a simple capacitive model, it is also proportional to V_t (the dashed straight line is a guide for the eye).

as expected from Eq. (A2). Similarly, Figs. A2**h** and S3**c**,**d** show that at zero field ($B = 0$), the leading temperature dependence is likewise quadratic,

$$g(T)/g(T_0) = 1 - (T/T_*)^2\,, \qquad T \ll T_*\,. \qquad \text{(S2b)}$$

Fitting Eqs. (S2a) and (S2b) to the data in Figs. S2**b** and S2**c**, respectively, yields the low-energy scales $B_*(V_c)$ and $T_*(V_c)$ used in Figs. A2**g** and A2**h** and depicted by colored symbols in Figs. A2**e** and A2**f**, respectively (and similarly for Figs. S3**a-d**). The scaled conductance curves displayed in Figs. S3**a-d** are plotted only in the restricted ranges $g(B)/g(0) \gtrsim 0.8$ and $g(T)/g(T_0) \gtrsim 0.8$, respectively. For smaller conductances, where the conditions $B \ll B_*$ or $T \ll T_*$ no longer hold, the measured B- and T-dependences of the conductance deviate from quadratic behavior by bending upward, tending toward saturation (as shown in Figs. A2**g**,**h**).

The fit parameters B_* and T_* are compared in the half-logarithmic presentation in Fig. A2**f** as functions of the center gate voltage ΔV_c. For convenience, this data is shown again in Fig. S3**f**, together with the low-energy source-drain voltage scale V_{sd*}. The latter was obtained by determining the curvature of the nonlinear conductance curves $g_{nl}(V_{sd})$ (shown in Fig. A3**i**) at $V_{sd} = 0$:

$$g_{nl}(V_{sd})/g_{nl}(0) = 1 - (V_{sd}/V_{sd*})^2, \quad V_{sd} \ll V_{sd*}\,. \qquad \text{(S2c)}$$

Compared to our determinations of B_* and T_* from linear-response data, those for V_{sd*} have rather larger error margins, since for technical reasons the non-linear conductance data was measured with a smaller signal-to-noise ratio.

As mentioned in the main article, SOPT makes two predictions for the $\widetilde{V}_c$-dependence of the crossover scales $\widetilde{B}_*$, $\widetilde{T}_*$ and $\widetilde{V}_{sd*}$ in the V_c-range where $g \to 1$: first, all three scales depend exponentially on V_c (Fig. S3**e**); and second, the ratios $\widetilde{B}_*/\widetilde{T}_*$ and $\widetilde{V}_{sd*}/\widetilde{T}_*$ are, to within a few %, independent of $\widetilde{V}_c$ (as illustrated in Fig. S4 for a range of U-values). The experimental results for B_*, T_* and V_{sd*} shown in Fig. S3**f** confirm both predictions. This demonstrates that at low energies a QPC shows Fermi-liquid behavior, as argued in detail in the main article.

C. Top-gate tuning of effective g_{ss}-factor

In a QPC geometry, interactions are known to enhance the effective electronic g-factor[7–9]. For large fields ($B \gg B_*$), an effective g-factor, say g_{ss}, can be extracted from the transconductance dg/dV_c, by exploiting the fact that the measured field-induced subband splitting of the first conductance step, say ΔE, increases linearly with field, $\Delta E = g_{ss} B$. In previous experiments with in-plane fields (B in the 2DES plane), $|g_{ss}|$-values have been observed exceeding the bulk value ($g_{GaAs} \simeq -0.45$) by up to a factor of 6[9,10], an increase that was attributed by Koop *et al.* to interaction effects[9].

In Fig. S5 we present the results of fRG calculations and measurements of the transconductance and the top-gate dependence of g_{ss} that confirm this interpretation. We numerically deduce the transconductance $\mathrm{d}G/\mathrm{d}V_c$ ($\mathrm{d}G/\mathrm{d}\widetilde{V}_c$) from both the measured and calculated conductance data. Typical experimental results are plotted in Fig. S5**a** for the range $0 < g < 1$ as a function of V_c. They show two peaks whose splitting ΔE increases linearly for large fields, as $\Delta E \simeq g_{ss} B + \Delta_{hfo}$ (Fig. S5**b**), where both the slope g_{ss} and the "high-field offset" Δ_{hfo} are found to increase with top-gate voltage V_t (Fig. S5**c**).

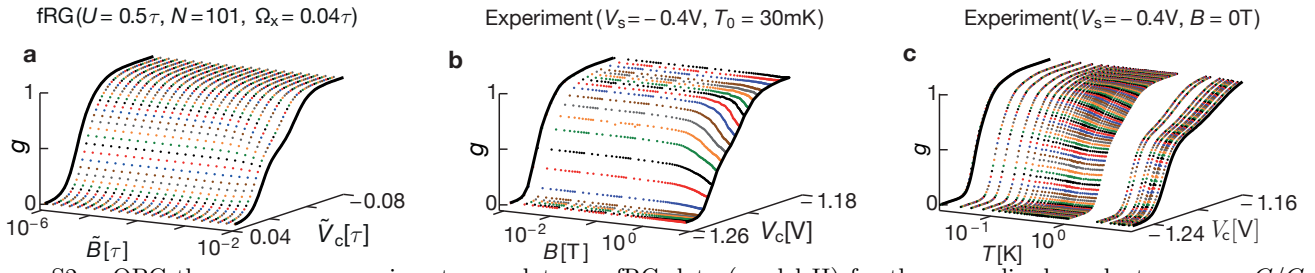

Figure S2: QPC theory versus experiment, raw data: **a**, fRG data (model II) for the normalized conductance $g = G/G_Q$, calculated at $T = 0$ and fixed side gate voltage $\widetilde{V}_s = 1.75\tau$ as function of center gate voltage $\widetilde{V}_c$ and magnetic field $\widetilde{B}$. **b**, **c** Experimental data for the normalized linear response conductance $g = (dI/dV_{sd})/G_Q$ (lead resistance subtracted), measured at fixed side and top gate voltages, $V_s = -0.4$ V and $V_t = 0.8$ V. **b** g at $T_{2DES} = T_0 = 30$ mK, measured as function of center gate voltage V_c and inplane magnetic field B aligned along the narrow constriction. **c**, g at $B = 0$, measured as function of V_c and temperature T. The data presented here are the raw data used for Figs. 2e-h in the main article and in Figs. S3**a-d** below. For better visibility, the pinch-off curves at minimal and maximal magnetic field / temperature have been highlighted by thick black lines, serving as guides for the eyes. The best signal-to-noise ratio was achieved by slowly sweeping B at constant V_c in **b**, and by sweeping V_c at constant T in **c**.

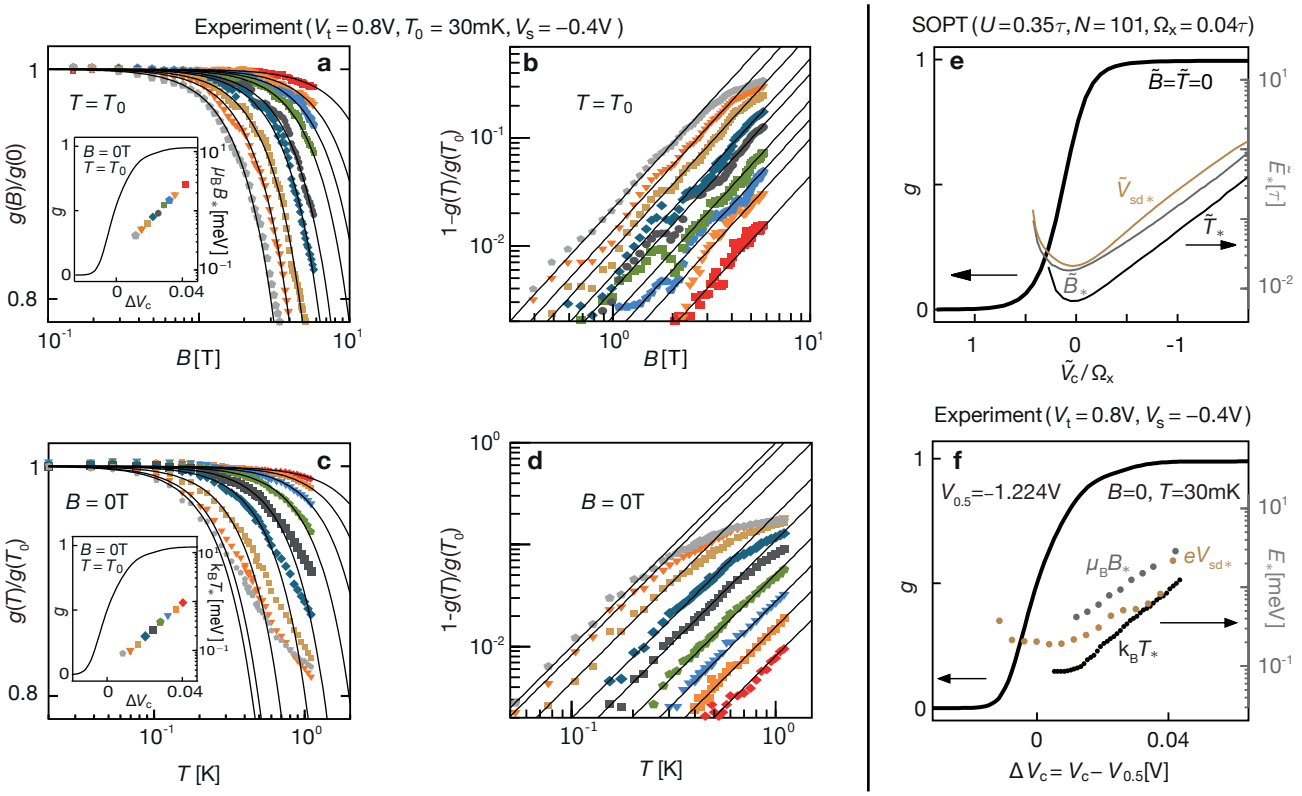

Figure S3: **a-d, Experiments; Fermi-liquid behavior.** **a**, $g(B)/g(0)$ on a lin-log-scale and **b**, $1 - g(B)/g(0)$ on a log-log-scale. **c** and **d**, as in **a** and **b** but for temperature instead of magnetic field dependence. These data supplement similar data shown in Figs. A2**g** and A2**h**, not repeated here. Black lines are fits of the form $g(X)/g(0) = 1 - X^2/X_*^2$ and express the leading quadratic decrease in both temperature and magnetic field. Insets demonstrate the exponential dependence of the scaling energies $\mu_B B_*$ and $k_B T_*$ (extracted from the fits) on V_c, respectively. Colored symbols in the main plots and corresponding insets have the same V_c-values. **e, f, Comparison of low-energy scales from theory and experiment: e** SOPT results for model II, for the conductance g (thick black line) and the low-energy scales $\widetilde{B}_*$, $\widetilde{T}_*$ and $\widetilde{V}_{sd*}$ (thin grey, black and brown lines, respectively), as functions of $\widetilde{V}_c$. **f** Corresponding experimental results for g, $\mu_B B_*$ and $k_B T_*$ (data repeated from insets of **a** and **c**) and eV_{sd*} as functions of $\Delta V_c = V_c - V_{0.5}$, where $V_{0.5}$ is the gate voltage for which the conductance at $B = 0$ and $T = T_0$ is $g(V_{0.5}) = 0.5$. V_{sd*} has been extracted from the leading quadratic dependence of the ZBP (as in **a-d** for $X = V_{sd}$). Note the strikingly good qualitative agreement between the SOPT results in **e** and the experimental results in **f**, for the gate-voltage dependence of all three low-energy scales.

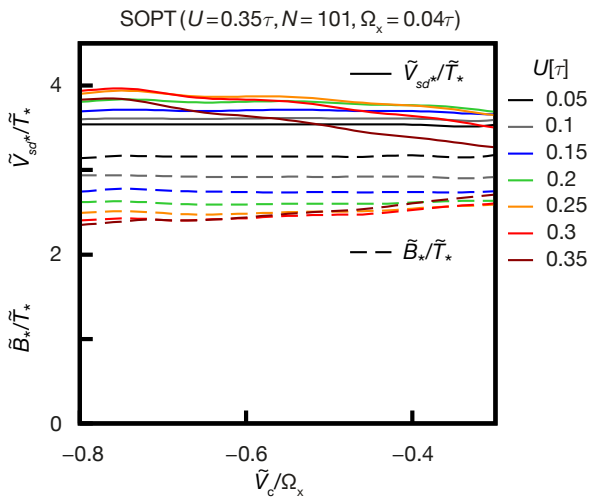

Figure S4: The ratios $\widetilde{V}_{\mathrm{sd}*}/\widetilde{T}_*$ (solid lines) and $\widetilde{B}_*/\widetilde{T}_*$ (dashed lines) as functions of $\widetilde{V}_\mathrm{c}/\Omega_x$ for several different U-values, calculated by SOPT for model II, using the same QPC barrier shape as used for Figs. A2**c**, **d**.

The effect of increasing V_t can be mimicked in our model by increasing U (for reasons explained in Supplementary Sec. S-2 A). Indeed, the results of our fRG calculations, shown in Fig. S5**d**-**f**, qualitatively match the trends shown by the experimental data in Fig. S5**a**-**c**. This establishes several important points. First, interactions are the reason why the g-factor extracted from $\Delta E(B)$ is anomalously large. Second, the effective interaction strength can be tuned experimentally via a top gate voltage. Third, the experimental observation of $\Delta_\mathrm{hfo} \neq 0$ can be understood *without* adopting the spontaneous spin polarization scenario that is often advocated[7,9,31] to explain it. Let us now elaborate these points in more detail.

We theoretically studied the U-dependence of g_ss by using fRG to calculate pinch-off curves for parabolic QPC barrier shapes such as that of Fig. A1**b**, for a range of fields $\widetilde{B}$ and interaction strengths U. Fig. S5**d** plots the transconductance, i. e. the derivative $-dg(\widetilde{V}_\mathrm{c})/d\widetilde{V}_\mathrm{c}$ as function of $\widetilde{V}_\mathrm{c}$ (varied over a range corresponding to $0 \leq g \leq 1$), for a large number of different $\widetilde{B}$-fields, at $U = 0.5\tau$. In such a plot the field-induced spin splitting of the conductance step manifests itself as a pair of local maxima[7–9,11]. The $\widetilde{V}_\mathrm{c}$-separation of their peaks, say ΔE, is proportional to the effective $\widetilde{B}$-induced subband splitting. Evidently ΔE increases with $\widetilde{B}$. Fig. S5**e** shows $\Delta E(\widetilde{B})$ vs. $\widetilde{B}$ for six values of U, including the data extracted from Fig. S5**d**. For large fields ($\widetilde{B} \gg \widetilde{B}_*$) we find a linear relation,

$$\Delta E(\widetilde{B}) \simeq (g_\mathrm{ss}/g_\mathrm{el})\widetilde{B} + \Delta_\mathrm{hfo} \ , \qquad \text{(S3)}$$

where Δ_hfo represents the "high-field offset" as defined by Koop *et al.*[9], i. e. the linear extrapolation of the high-field behavior to $\widetilde{B} = 0$. Fig. S5**f** and its inset show that both the slope and the offset increase with U, implying that both g_ss and Δ_hfo serve as measures of the effective interaction strength.

Koop *et al.* have reported a strong enhancement of the g-factor as the spacing ω_{12} between the electronic subbands of the QPC is increased[9]. Our theory nicely explains this finding: an increase in ω_{12} corresponds to a smaller transverse channel width, implying an enhanced interaction strength (as argued at the end of section S-2 A) and hence an increase in g_ss (see Fig. S5**f**).

This interpretation is confirmed by the experimental data shown in Fig. S5**a**-**c**. This data was measured using a second sample ("sample 2"), of similar design than that used to study the Fermi-liquid properties of Figs. A2**e**-**h** discussed in the main text ("sample 1"). For sample 2, we measured $\Delta E(B) = a \cdot \Delta V_c$ (for the values of the conversion factor a see table in Fig. S5**b**) as function of top gate voltage V_t, which corresponds to tuning the effective interaction strength. According to our theoretical considerations, increasing V_t causes increasing U [see Eq. (S1)] and hence increasing g_ss (by Fig. S5**f**). Fig. S5**a**-**c** present experimental results corresponding to the predictions in Fig. S5**d**-**f** (using V_t instead of U). They qualitatively confirm our numerical results, especially that both g_ss and Δ_hfo increase with V_t and, therefore, the interaction strength. (In contrast to us, Koop *et al.* did not observe a systematic correlation between g_ss and Δ_hfo. A possible reason is that their study varied the shape of the QPC potential by varying the width and length of the QPC, whereas we varied V_t. Our studies thus differ from theirs in the detailed shape of the 2D potential landscape. The effective interaction strength is very sensitive towards the latter, as discussed in more detail in Sec. S-5 C.)

We conclude our discussion on $\Delta E(B)$ with an important comment on the high-field offset Δ_hfo. In several experimental studies of the 0.7-anomaly[7–9], the observation of a nonzero value for Δ_hfo was interpreted as evidence "that there is a possible spin polarization of the 1D electron gas in zero magnetic field" (the quote is from Thomas *et al.*[7]). Our fRG results show that this interpretation is not compelling, since we obtain $\Delta_\mathrm{hfo} \neq 0$ without any spontaneous spin polarization. $\Delta_\mathrm{hfo} \neq 0$ simply implies that the $\widetilde{B} = 0$ conductance step $g(\widetilde{V}_\mathrm{c})$ is somewhat skewed (see Figs. A1**k**, A1**l**, A2**a**), so that the peak in the transconductance is not symmetric (as seen in Fig. S5**d**); as shown here, this can be achieved with a magnetization that is strictly zero. Indeed, our fRG approach assumes from the outset that the magnetization per site, $m_j = \frac{1}{2}(n_{j\uparrow} - n_{j\downarrow})$, is strictly zero at $\widetilde{B} = 0$ (see blue line in Fig. A1d, and introduction of Sec. S-6). This *a priori* assumption is justified *a posteriori* by the good qualitative agreement between fRG and experiment found throughout this work, and in Fig. S5 in particular. Moreover, this assumption is a prerequisite for understanding the low-energy Fermi-liquid properties of the 0.7-anomaly discussed in the main text, and the resulting analogies between the 0.7-anomaly and the Kondo effect: for the latter, there is zero spin polarization at

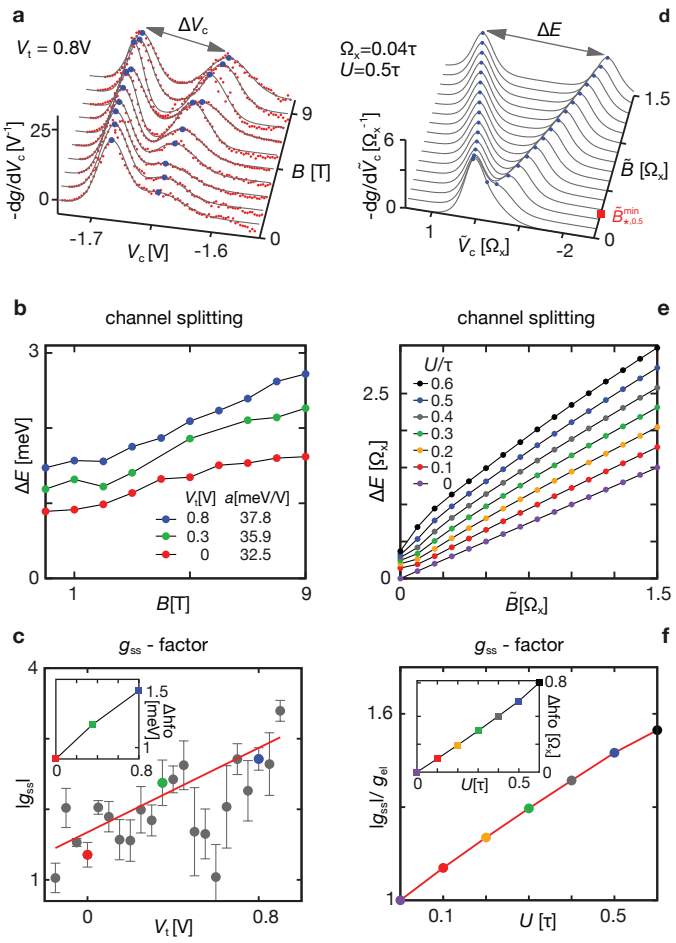

Figure S5: **Determination of the subband-splitting g-factor g_{ss}.** **a-c.** Results from experimental measurements on a sample ("sample 2") of similar design as that discussed in the main text ("sample 1"). **d-f**, Corresponding results from fRG calculations. **a,d**, The transconductance, i. e. the derivative of the conductance with respect to gate voltage (V_c in **a**, $\widetilde{V}_c$ in **d**), plotted as a function of gate voltage, for several magnetic fields. An increasing magnetic field lifts the spin degeneracy, causing the conductance step to split into two spin-resolved sub-steps and giving rise to two local maxima in **a,d** (marked by blue dots). In **d**, $\widetilde{B}^{\rm min}_{*,0.5}$ (red square) stands for $\widetilde{B}^{\rm min}_{*}$ at $U = 0.5$. **b**,**e**. The peak distance ΔE, determined by fitting a pair of Gaussians (shown by gray lines in **a**) to the peak pairs in **a,d**, is plotted as function of magnetic field, in **b** for three different top gate voltages, and in **e** for seven different values of the on-site interaction U. Linear least-square fits to such curves in the range of large fields, using $\Delta E \simeq g_{\rm ss} B + \Delta_{\rm hfo}$, yield the effective g-factor $g_{\rm ss}$ and high-field offset $\Delta_{\rm hfo}$. Errors, s. e. m. ($n = 5$ - 7). (To convert ΔV_c in **a** to ΔE in **b**, we used the V_t-dependent conversion factors $a = \Delta E/\Delta V_c$ listed in the legend of **b**, obtained approximately from nonlinear transport measurements[7,9].) **c,f**, $|g_{\rm ss}|$ (and in insets, $\Delta_{\rm hfo}$), plotted as a function of V_t (in **c**) or U (in **f**). The red straight line in **c** is a error-weighted least square fit. Both theory and experiment show the same trend, namely that $g_{\rm ss}$ and $\Delta_{\rm hfo}$ increase with the effective interaction strength U (which increases with V_t in our sample geometry.

$\widetilde{B} = T = 0$, because lead electrons screen the local spin into a spin singlet.

It is noteworthy, though, that the linear increase in $\Delta E(\widetilde{B})$ in Fig. S5**e** sets in already at rather small fields, of order $\mathcal{O}(\widetilde{B}_*)$ and similarly for $\Delta E(B)$ in Fig. S5**b**. The reason is that at small fields the spin polarization *rapidly* grows with field, since the spin susceptibility is *large*. It is large because it is strongly enhanced by interactions (Fig. A1**j**), as recognized and emphasized by Thomas *et al.*[7], and because the effects of interactions are further enhanced by the van Hove ridge in the QPC, as discussed in the main article. According to our analysis, the large spin susceptibility goes hand in hand with a strong interaction-induced enhancement in the inverse scale $1/B_*(\propto \chi_{\rm tot})$ [Fig. A1**j**], as discussed in the main article, and also in Sec. S-5 B below.

The scale $\widetilde{B}_*$ governs the "strength" of the 0.7-anomaly, in that the conductance is significantly reduced once $\widetilde{B}$ or $\widetilde{T}$ increase past $\widetilde{B}_*$. In an alternative model proposed by Reilly *et al.*[12], one of the advocates of spontaneous spin polarization, the strength of the 0.7-anomaly is governed by the size of the spin gap. This model was used successfully, for example, to model the shot noise measurements of Ref. 13. The Reilly model assumes that the spin gap increases strongly with decreasing V_c, i. e. with increasing density in the QPC-region. Note that this $\widetilde{V}_c$-dependence of the proposed spin gap shows the same tendency as that shown by the Hartree-enhancement of the barrier size in our work, which likewise increases linearly with increasing density as $\widetilde{V}_c$ is made more negative. (The density near the CCR center also increases as temperature or source-drain voltage is increased, and becomes strongly spin-asymmetry as $\widetilde{B}$ increases.) In this sense, our work sheds light on why the Reilly model is phenomenologically successful at large energies: it makes qualitatively correct assumptions about the V_c-dependence of the effective barrier height that governs the strength of the conductance's B- or T-dependence. That having been said, we emphasize once more that our Hartree-shift in barrier height is not a spin gap, and that our scenario differs decidedly from that of the Reilly model for energies below B_*: there we assert the appearance of Fermi-liquid behavior that is not compatible with spontaneous spin polarization. In our theory, a spin splitting sets in only once spin symmetry is broken by finite $\widetilde{B}$ (though a spin-symmetric Hartree-shift in barrier height is present even at $\widetilde{B} = 0$). The spin gap predicted by our theory for $\widetilde{B} \neq 0$ does increase with the density in the QPC, as in the Reilly model, since it arises from Hartree contributions to the self-energy (see Eq. (S42) in our fRG scheme, or the first two diagrams in Eq. (S53) when doing perturbation theory).

S-3. OTHER EXPERIMENTAL DATA VS. FRG

This section presents additional fRG results on the zero-temperature behavior of the conductance, the shot noise, and the charge susceptibility. Their $\widetilde{V}_c$- and $\widetilde{B}$-dependence is found to be in qualitative agreement with that observed experimentally by other groups (DiCarlo *et al.* for the shot noise[13], Smith *et al.* for the compressibility[14].

The fRG results presented below were obtained using "static" fRG, a simplified version of the "dynamic" fRG scheme used in the main text. Static fRG neglects the frequency dependence of the self-energy and all vertices (see Sec. S-6 F). This simplification reduces computational costs by a factor of 10^3. Nevertheless, for the model studied here the results of static fRG turn out to be qualitatively very similar to those of dynamic fRG (see Fig. S15 below). Hence we have opted to use static fRG for the results presented in Secs. S-3 and S-5.

A. Spin-resolved conductance, shot noise

This subsection presents a detailed discussion of the spin-resolved conductance. It is based on calculations using model I (defined in Sec. S-4 B), but the results are fully analogous to those shown in Figs. A2**a**, **b** for model II (defined in Sec. S-4 D).

The role of interactions for the magnetoconductance of a QPC at zero temperature can be very clearly revealed by studying the spin-resolved conductance $g_\sigma = \mathcal{T}_\sigma$ and the shot noise factor[15]

$$\mathcal{N} = \frac{1}{2}\sum_\sigma g_\sigma(1-g_\sigma). \tag{S4}$$

Fig. S6 shows these quantities together with the full conductance $g = g_\uparrow + g_\downarrow$, all calculated at $T = 0$ as functions of $\widetilde{V}_c$, for various fields. To highlight the effect of interactions, we also show corresponding results for the bare ($U = 0$) model, which we discuss first.

We begin with some elementary observations: First, the bare transmission probability $\mathcal{T}^0_\sigma(\widetilde{V}_c, 0)$ at zero field, studied as function of $\widetilde{V}_c$, is antisymmetric w. r. t. the point $\mathcal{T}^0_\sigma(0,0) = 0.5$ [cf. Eq. (S30) below]:

$$\mathcal{T}^0_\sigma(\widetilde{V}_c, 0) = 1 - \mathcal{T}^0_\sigma(-\widetilde{V}_c, 0)\ . \tag{S5}$$

A finite field $\widetilde{B}$ shifts the bare potential in opposite directions for opposite spins, $\delta\widetilde{V}_j = -\frac{\sigma}{2}\widetilde{B}$ (with $\sigma = \pm 1$ for $\uparrow$, $\downarrow$). Thus the bare spin-resolved transmission probability $\mathcal{T}^0_\sigma$ at finite $\widetilde{B}$ is equal to that at $\widetilde{B} = 0$ but for a shifted value of $\widetilde{V}_c$:

$$\mathcal{T}^0_\sigma(\widetilde{V}_c, \widetilde{B}) = \mathcal{T}^0_\sigma(\widetilde{V}_c - \tfrac{\sigma}{2}\widetilde{B}, 0). \tag{S6}$$

This implies that $\widetilde{B}$ induces a shift (but not a change in shape) for the spin-resolved conductance step in g_σ by $\frac{\sigma}{2}\widetilde{B}$ (see Figs. S6**b-c**). Nevertheless, since Eqs. (S6) and (S5) together imply

$$\mathcal{T}^0_\sigma(\widetilde{V}_c, \widetilde{B}) = 1 - \mathcal{T}^0_{\bar\sigma}(-\widetilde{V}_c, \widetilde{B})\ , \tag{S7}$$

the full conductance remains antisymmetric w. r. t. the point $\mathcal{T}^0_\sigma(0, \widetilde{B}) = 0.5$ even for finite $\widetilde{B}$ (see Fig. S6**a**):

$$g^0(\widetilde{V}_c, \widetilde{B}) = 1 - g^0(-\widetilde{V}_c, \widetilde{B})\ . \tag{S8}$$

Eq. (S7) also implies that the bare shot noise, $\mathcal{N}^0$, is symmetric w. r. t. $\widetilde{V}_c = 0$, or $g = 0.5$ (see Fig. S6**j**).

The above antisymmetry of $g(\widetilde{V}_c)$ w. r. t. $\widetilde{V}_c = 0$ is broken in the presence of interactions, in a manner that becomes increasingly more pronounced with increasing field, see Figs. S6**d** and S6**g**, for $U/\tau = 0.2$ and 0.45, respectively. In the latter case the broken antisymmetry is visible already at zero field, in that the fRG conductance curve shows a slight 0.7-shoulder, in agreement with experiment (cf. Fig. A2**e**). This shoulder at $\widetilde{B} = \widetilde{T} = 0$ occurs because the interaction-induced increase of the effective potential barrier is enhanced by the van Hove ridge in the local density of states (LDOS) and hence is nonuniform in $\widetilde{V}_c$ (see the main article for a detailed explanation). The breaking of $\widetilde{V}_c$-antisymmetry increases with $\widetilde{B}$ because (exchange) interactions amplify the field-induced asymmetry in the population of spin-up and -down electrons in the CCR, in particular near the top of the barrier: a small $\widetilde{B}$-induced surplus of spin-up electrons leads to a significantly increased Hartree barrier, and more so for spin-down electrons than for spin-up electrons (due to the Pauli principle), causing a strong decrease of $g_\downarrow$ relative to $g_\uparrow$. This effect, whose strength increases with U (compare 2nd and 3rd columns of Fig. S6) results in the field-induced strengthening of the 0.7-shoulder that is characteristic of the 0.7-anomaly, and its evolution into a double step for large fields.

The increasing $\widetilde{V}_c$-asymmetry (i. e. departure from perfect antisymmetry) in $g_\sigma(\widetilde{V}_c)$ as $\widetilde{B}$ increases is also reflected in the shot noise factor $\mathcal{N}(g)$ [Eq. (S4)], see Figs. S6**k** and S6**l**, for $U/\tau = 0.2$ and 0.45, respectively. For zero applied field, $\mathcal{N}(g)$ is symmetric w. r. t. $g = 0.5$; this follows directly from the form of Eq. (S4) (which holds whenever a Fermi-liquid description applies), and our assumption that there is no spontaneous breaking of spin symmetry at $\widetilde{B} = 0$, implying $g_\uparrow = g_\downarrow$. With increasing field, $\mathcal{N}(g)$ develops an g-asymmetry w. r. t. $g = 0.5$, being somewhat suppressed in the range $g > 0.5$ relative to its values in the range $g < 0.5$. This field-induced g-asymmetry is in good qualitative agreement with the experimental measurements of the noise factor by DiCarlo *et al.*, cf. Fig. 4(d) of Ref. 13. Note, though, that the measured noise factor shows an g-asymmetry even at zero field, in contrast to our fRG predictions; we believe that this remnant g-asymmetry is a finite-temperature effect that will gradually disappear if the experimental temperature is lowered further. Reproducing this behavior explicitly by a finite-temperature calculation of the

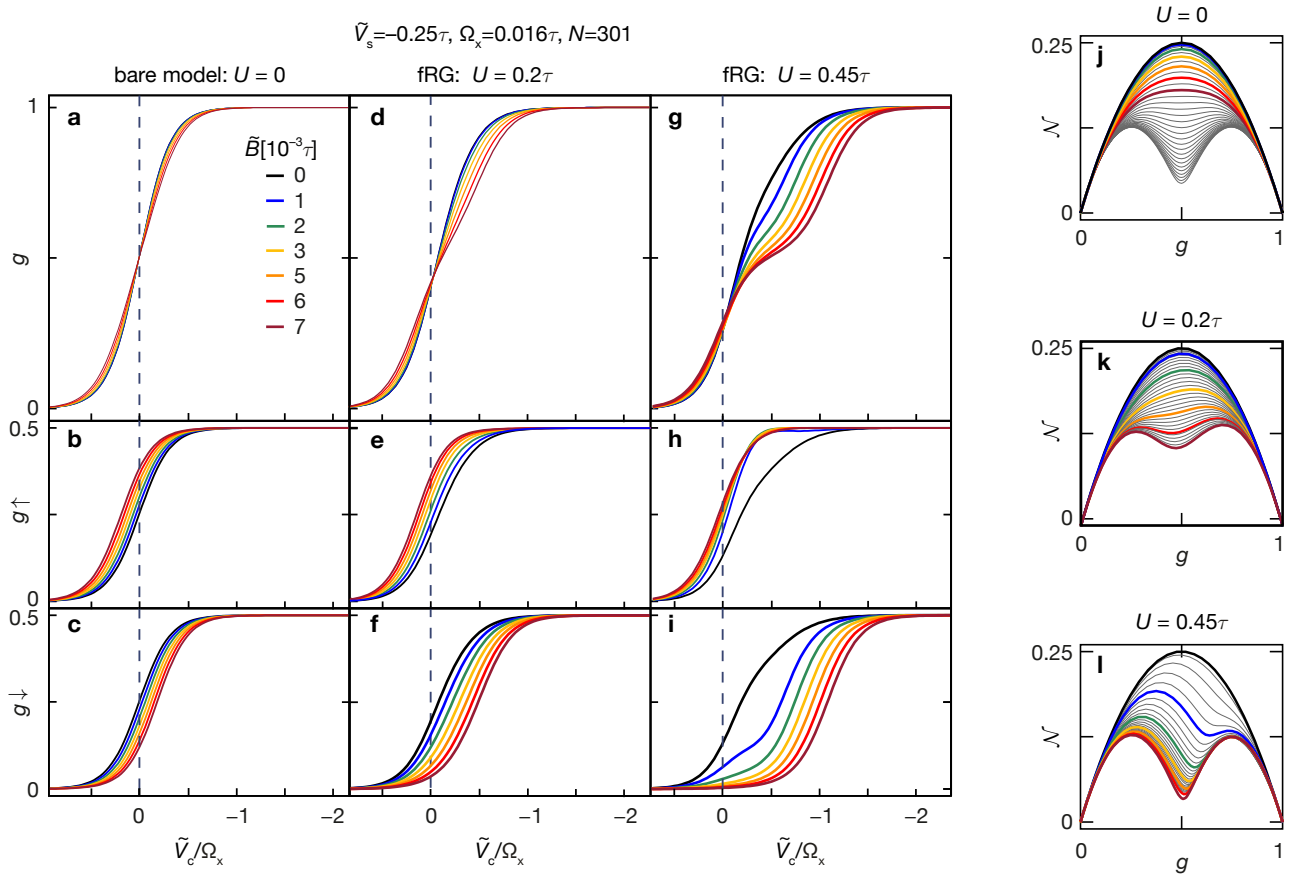

Figure S6: Comparison of results for model I, for its bare $U = 0$ version (first column), or treated using static fRG for $U/\tau = 0.2$ and 0.45 (second and third columns, respectively). The top, middle and bottom rows show, respectively, the full QPC conductance $g = g_\uparrow + g_\downarrow$ and its spin-resolved contributions $g_\uparrow$ and $g_\downarrow$, all plotted as functions of $\tilde{V}_c/\Omega_x$ for several values of magnetic field $\tilde{B}$. The fourth column shows a similar comparison for the shot noise factor $\mathcal{N}$ [Eq. (S4)], plotted as function of g.

noise factor for our model is left as a task for future study.

B. Compressibility and charge susceptibility

Recently, Smith *et al.*[14] have experimentally studied the compressibility of the electron gas of a QPC. In particular, they measured the V_c-dependence of the compressibility in the vicinity of the 0.7-anomaly and studied its evolution with increasing temperature and magnetic field. The compressibility is a measure of the density of states at the chemical potential. In a QPC geometry, its V_c-dependence is thus governed by that of the LDOS maxima at the bottom of the 1D band, i. e. by the van Hove ridge discussed in detail in the main article and in Sec. S-4 C below (see the yellow ridges in Fig. A1**b** and Fig. S10**d**); and its B-dependence is governed by the spin splitting of this van Hove ridge.

Within our model, the compressibility can be associated with the charge susceptibility of the CCR,

$$\chi_\mu = \frac{dn_{\rm tot}}{d\mu}, \qquad n_{\rm tot} = \sum_{j\sigma}^{\rm CCR} n_{j\sigma}\,, \tag{S9}$$

where $n_{\rm tot}$ is the total charge in the CCR and μ the chemical potential. Figs. S7**a** and S7**b** show zero-temperature fRG results for the conductance $g(\widetilde{V}_c)$ and the charge susceptibility $\chi_\mu(\widetilde{V}_c)$, respectively. The results exhibit a number of features, enumerated below, that are qualitatively consistent with features observed by Smith *et al.*[14].

Consider first the noninteracting case, $U = 0$ (black dashed lines for g^0 and χ^0_μ): When $\widetilde{V}_c$ is lowered past 0, the bare charge susceptibility $\chi^0_\mu(\widetilde{V}_c)$ in Fig. S7**b** traverses a single broad peak, aligned with the center of the corresponding conductance step in Fig. S7**a**. This peak arises because the bare charge susceptibility equals the bare total density of states at the chemical potential [cf.

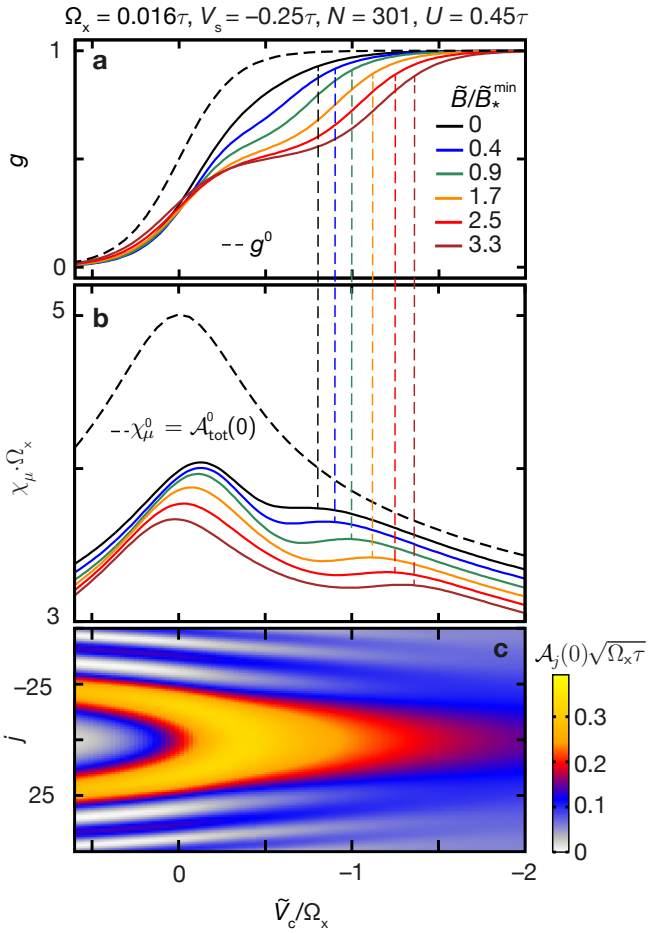

Figure S7: **Charge Susceptibility.** Static fRG results (model I) for (a) the conductance $g(\widetilde{V}_c)$ and (b) the charge susceptibility $\chi_\mu(\widetilde{V}_c)$ [Eq. S9] as function of $\widetilde{V}_c$, calculated for six values of $\widetilde{B}$ at a fixed $\widetilde{V}_s$ and $\widetilde{T} = 0$. Black dashed lines in **a** and **b** show the bare ($U = 0$, $\widetilde{B} = 0$) curves, g^0 and $\chi_\mu^0 = \mathcal{A}_{\rm tot}^0(0)$, respectively. Vertical dashed lines are a guide for the eyes and mark the weak shoulder or second maximum of $\chi_\mu(\widetilde{V}_c)$. **c**, The full ($U \neq 0$) LDOS at the chemical potential, $\mathcal{A}_j(0)$, as function of gate voltage $\widetilde{V}_c$ and site index j.

Eq. (S39)],

$$\chi_\mu^0 = \sum_{j\sigma}^{\rm CCR} \mathcal{A}_{j\sigma}^0(0) = \mathcal{A}_{\rm tot}^0(0), \tag{S10}$$

which traverses a peak when the spin-degenerate van Hove ridge is lowered past μ. For nonzero U but still $\widetilde{B} = 0$ (black solid lines), $\chi_\mu(\widetilde{V}_c)$ is reduced, since interactions tend to counteract the (infinitesimal) increase in charge induced by an (infinitesimal) increase in μ [Eq. (S9)]. This reduction occurs in such a way that (i) $\chi_\mu(\widetilde{V}_c)$ retains a dominant peak, with (ii) a weak shoulder developing on its right (even though $\widetilde{B} = 0$), roughly aligned with the roll-over of $g(\widetilde{V}_c)$ towards the first conductance plateau. This shoulder arises because when $\widetilde{V}_c$ decreases into the open-channel regime, the van Hove ridge apex drops so far below μ that $\mathcal{A}_j(0)$, the LDOS at μ, decreases rapidly (Fig. S7**c**). As a result, its interaction-enhancing effects, and hence also the Coulomb-blockade reduction in χ_μ, weaken rapidly, resulting in a shoulder in χ_μ.

The colored lines in Fig. S7 show the evolution of the conductance $g(\widetilde{B})$ and charge susceptibility $\chi_\mu(\widetilde{V}_c)$ with magnetic field for $U = 0.45\tau$. While the conductance step evolves into the familiar spin-split double step with increasing field (Fig. S7**a**), (iii) the dominant peak in $\chi_\mu(\widetilde{V}_c)$ (Fig. S7**b**) remains aligned with the center of the first conductance step, while (iv) the shoulder in $\chi_\mu(\widetilde{V}_c)$ develops into a weak peak that shifts towards the right, remaining roughly aligned with the roll-over to the second conductance plateau (as indicated by dashed colored lines between Figs. S7**a** and S7**b**). This reflects the field-induced spin-splitting of the van Hove ridge into two spin-resolved sub-ridges, which get lowered past μ at different $\widetilde{V}_c$-values. As a result, (v) $\chi_\mu(\widetilde{V}_c)$ develops a weak minimum between the two peaks.

Features (i)-(v) can also be found, on a qualitative level, in Figs. 2 and 3(a) of Smith *et al.*. Their measured signal, called $dV_{\rm sg}/dV_{\rm mid}$ there, has minima when the compressibility has maxima, and vice versa. In their Fig. 2(a), the red curve shows a strong dip at $V_{\rm mid} = 0.14$ V and a very weak minimum at 0.22 V. We associate these, respectively, with the dominant peak (i) and the weak shoulder (ii) in $\chi_\mu(\widetilde{V}_c)$ discussed above. In their Fig. 2(b), the two dips in the red curve at $V_{\rm mid} = 0.12$ V and 0.19 V, correspond, respectively, to the two maxima mentioned in (iii) and (iv) above. And in their Fig. 3(a), the peak marked by an arrow corresponds to the dip mentioned in (v). We thus conclude that the measured compressibility maxima accompanying the conductance steps are indeed due to maxima in the density of states at the band bottom, as suggested by Smith *et al.* themselves (and in Ref. 16). This supports our contention that van Hove ridges play a central role in the physics of the 0.7-anomaly. By implication it also confirms the presence of the "quasi-bound states" advocated by Meir and collaborators[17–19], provided that we identify their "quasi-bound states" with our van Hove ridges – as argued in Sec. S-4 E below, both names refer to the same peaked structures in the LDOS.

This identification was not clear at the time of writing of Ref. 14, however. Instead, Smith *et al.* argued that they see "no evidence of the formation of the quasi-bound state predicted by the Kondo model". This statement was based on a comparison of their $B = 0$ data for $dV_{\rm sg}/dV_{\rm mid}$ to simulations[16] using density-functional theory (DFT) combined with the local spin density approximation (LSDA). These data and the simulation results are shown, respectively, as black and red curves in Fig. 4(b) of Ref. 14. The simulations yielded an additional strong dip [indicated by an arrow in Fig. 4(b)],

aligned with the onset of the conductance plateau, that had no counterpart in the measured data. We suspect that this additional strong dip might be an artefact of the tendency of DFT+LSDA calculations, when initialized using a small nonzero magnetic field[19,20], to yield a nonzero spin polarization in regions where the spin susceptibility is large (as is the case in the QPC). We assert, however, that at $B = 0$ the spin polarization is strictly zero (in contrast to views expressed in Refs. 7,8,14), since this is a prerequisite for understanding the Fermi-liquid properties discussed in the main article. Our fRG calculations for $\widetilde{B} = 0$ thus assume zero spin polarization from the outset. Remarkably they yield, instead of the strong additional peak found by DFT+LSDA, only the weak shoulder (ii) mentioned above, which is consistent with the compressibility data of Smith *et al.* Further arguments in support of the absence of spontaneous spin polarization at zero field are offered at the end of Sec. S-2 C.

PART II: THEORETICAL DETAILS

S-4. MODELS USED FOR BARRIER SHAPE

In the course of our studies of the 0.7-anomaly, we have explored many different parametrizations of smooth, symmetric QPC barrier shapes. We found that as long as the barrier top is parabolic, characterized by a barrier height $\widetilde{V}_{\rm c}$ (w. r. t. to the chemical potential) and a curvature parameter Ω_x, the details of the parametrization of the barrier do not matter.

In this section we present the details of two different parametrizations for parabolic barriers, to be called "model I" and "model II", whose results for QPC properties are fully equivalent when expressed as functions of $\widetilde{V}_{\rm c}$ and Ω_x. Both models use the same Hamiltonian, choice of chemical potential and local interaction strength U_j, specified in Sec. S-4 A, but differ in their choices for the hopping amplitude τ_j (which is j-independent for Model I but not for Model II) and the on-site potential E_j.

Model I is presented in Sec. S-4 B: its hopping amplitude is j-independent, $\tau_j = \tau$, and the barrier shape is specified by parametrizing E_j in terms of a central gate voltage $\widetilde{V}_{\rm c}$ and a side gate voltage $\widetilde{V}_{\rm s}$. It is designed to allow a theoretic study of the crossover between a Kondo quantum dot (KQD) and a QPC by continuously deforming the 1D potential from a double-barrier to a single-barrier shape (see Figs. S9**c** and S9**d** below, respectively). (The results of a corresponding study will be published elsewhere[1].) Here we use model I to calculate numerous QPC properties presented in various parts of the supplementary material (Figs. S6, S7, S10, S11, S13 and S14). Moreover, model I allows instructive insights into the similarities and differences between the bare density of states of a QD and a QPC, which are key to understanding the similarities and differences between the Kondo effect and the 0.7-anomaly, as briefly discussed in Sec. S-4 C.

For model II, presented in Sec. S-4 D, τ_j depends nontrivially on j, and the barrier shape is specified solely in terms of a central gate voltage $\widetilde{V}_{\rm c}$ and the barrier curvature Ω_x (adjusted via the length N of the CCR, but without reference to a side gate voltage). Compared to model I, model II has technical advantages when treated using SOPT (as explained below). For clarity, model II was used for all numerical results (both from fRG and SOPT) presented in the main article. It was also used for Figs. S2, S4, S12, S16 in the supplementary material. We emphasize that the results obtained using models I and II are qualitatively consistent.

To conclude our introductory comments on the models used here, we remark that the idea of studying the 0.7-anomaly using an effective 1D model with a smoothly varying QPC potential and local interactions has of course been pursued previously by numerous authors. For example, a model with local exchange interactions was studied in Refs. 21 and 22, a model with an unscreened Coulomb interaction in Ref. 6, and a model with a point like interaction restricted to the center of the QPC potential in Ref. 23. Our work is similar in spirit to these, but our use of fRG allows us to treat the effects of interactions more systematically than Refs. 21 and 6, and for longer chains than Ref. 22, which also did not have access to the limit $T \to 0$. Works based on 2D or 3D density-functional theory calculations[16–20] treat the potential landscape more realistically than we do, but at the expense of not treating correlation effects as accurately as fRG does. In particular, our fRG treatment allows accurate predictions for the conductance at zero temperature, which is beyond the scope of all previous treatments. Moreover, our SOPT calculations at finite source-drain voltages are first to give a detailed description of the origin of the ZBP.

A. Hamiltonian, chemical potential, U_j

The model Hamiltonian defined in the main article,

$$\hat{H} = \sum_{j\sigma}\Big[E_{j\sigma}\hat{n}_{j\sigma} - \tau_j(d^\dagger_{j+1\,\sigma}d_{j\sigma} + \text{h.c.})\Big] + \sum_j U_j\hat{n}_{j\uparrow}\hat{n}_{j\downarrow}, \tag{S11}$$

with $E_{j\sigma} = E_j - \frac{\sigma}{2}\widetilde{B}$, is depicted schematically in Fig. S8. It shows a tight-binding chain divided into two semi-infinite, non-interacting, uniform leads on the left and right, connected to the central constriction region (CCR),

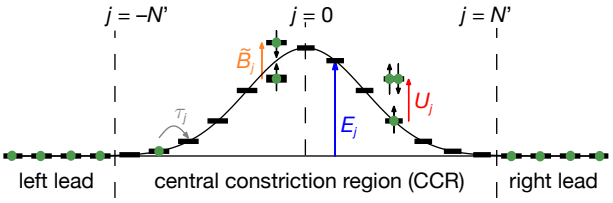

Figure S8: Schematic depiction of the one-dimensional model of Eq. (S11) (for a QPC barrier shape). It represents an infinite tight-binding chain with hopping matrix element τ_j (gray); the prescribed local potential E_j (blue) and on-site interaction U_j (red) are nonzero only within a central constriction region (CCR) of $N = 2N' + 1$ sites. The CCR is connected to two semi-infinite non-interacting leads on the left and right. A homogeneous Zeeman magnetic field $\widetilde{B}$ (orange) can be switched on along the whole chain.

consisting of an odd number $N = 2N'+1$ of sites centered on $j = 0$. The lattice does not represent actual atomic sites, but instead is merely used to obtain a discrete, coarse-grained description of transport in the lowest subband. The position-dependent parameters U_j and E_j, nonzero only within the CCR, are taken to vary slowly on the scale of the lattice spacing a. (We set $a = 1$ in our calculations.)

Choice of μ: Since the chemical potential is a property of the bulk, we begin by considering our model for $E_j = U_j = 0$ and $\tau_j = \tau$, representing a bulk tight-binding chain (infinite, homogeneous). The eigenergies ϵ_k corresponding to wave number k have dispersion

$$\epsilon_k = -2\tau\cos(ka) \ \in [-2\tau, 2\tau] \ , \qquad \text{(S12)}$$

plotted in Fig. S9**a**. To describe the phenomena of present interest, the chemical potential μ should lie somewhere within this band, not too close to its edges; the precise value does not matter. All our numerical calculations (fRG and SOPT) used $\mu = 0$, implying half-filled leads; but for the sake of generality, we keep μ arbitrary below, particularly in Figs. S9**a**,**b** and S10**a**,**b**.) The energy difference between the chemical potential and the bulk band bottom defines the bulk Fermi energy,

$$\varepsilon_{\rm F} = 2\tau + \mu \quad (> 0) \ . \qquad \text{(S13)}$$

Choice of U_j: In choosing a purely on-site interaction in Eq. (S11), we implicitly assume that screening is strong enough to render the interaction short-ranged. (A more realistic treatment of screening is beyond the scope of this work.) We set the on-site interaction U_j equal to U throughout the CCR, except near its edges, where it drops smoothly to zero to avoid spurious backscattering effects (Fig. S9**e**):

$$U_j = \begin{cases} 0 \ , & \forall \quad N' \le |j| \ , \\ U \exp\left[-\frac{\left(\frac{j}{N'}\right)^6}{1-\left(\frac{j}{N'}\right)^2}\right] & \forall \quad |j| \le N' \ . \end{cases} \qquad \text{(S14)}$$

U is to be regarded as an effective parameter, whose value is influenced by the transverse modes not treated explicitly in our model. In particular, the effect of increasing

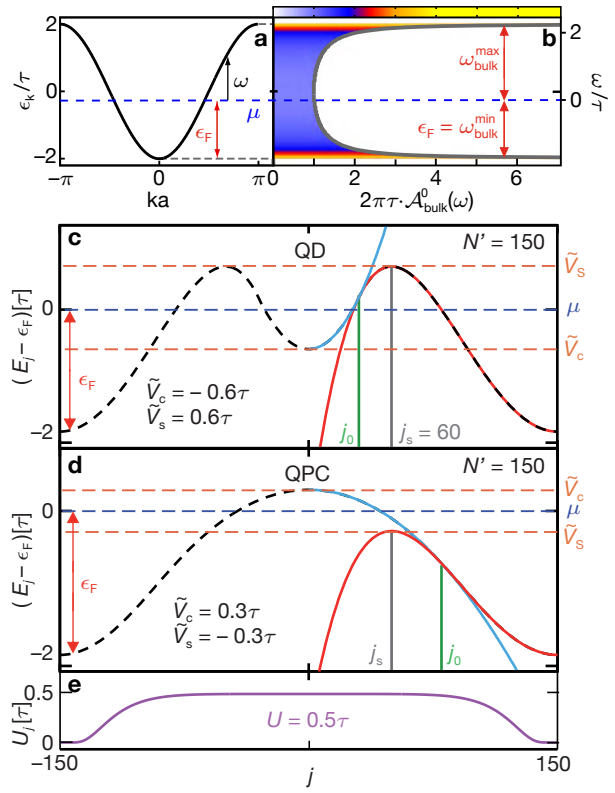

Figure S9: **a**, Dispersion relation ϵ_k vs. k [Eq. (S12)] for a bulk non-interacting tight-binding chain without magnetic field (infinite, homogeneous, $E_{j\sigma} = U_j = 0$). The filling factor in the leads is controlled by the global chemical potential μ (blue dashed line); it is here drawn at $\mu \neq 0$ for generality, although our fRG calculations use $\mu = 0$. **b**, The corresponding j-independent bulk LDOS [Eq. (S19)], shown both as $\mathcal{A}^0_{\rm bulk}(\omega)$ (on x-axis) versus $\omega = \epsilon_k - \mu$ (on y-axis), and using a color scale. The distance from the chemical potential to the bulk band bottom $\omega^{\rm min}_{\rm bulk}$ is $\varepsilon_{\rm F} = 2\tau + \mu = -\omega^{\rm min}_{\rm bulk}$ (> 0). **c** and **d**, Model I: The one-dimensional potential E_j of Eq. (S15) (thick dashed black line) for a QD potential ($\widetilde{V}_{\rm s} > \widetilde{V}_{\rm c}$) and a QPC potential ($\widetilde{V}_{\rm c} > \widetilde{V}_{\rm s}$), respectively. In the outer region of the CCR ($j_0 \le |j| \le N'$), E_j is described by quartic polynomial, in the inner region ($|j| < j_0$) by a quadratic one (thin red and blue lines, respectively, shown only for $j > 0$.) For given N', $j_{\rm s}$, $\widetilde{V}_{\rm s}$ and $\widetilde{V}_{\rm c}$, the parameters j_0 and $\overline{\Omega}_x$ are adjusted such that the resulting potential E_j depends smoothly on j throughout the CCR. **e**, The on-site interaction U_j of Eq. (S14).

the top gate voltage $V_{\rm t}$ can be mimicked by increasing U [Eq. (S1)], as will be discussed in more detail in Sec. S-5 C. We typically take U to be somewhat smaller than the maximum value of the inverse bare LDOS, since if $U \cdot \max[\mathcal{A}^0_j(\omega)]$, is too large, the fRG calculations do not converge. We remark that we have also explored the option of taking U_j to be proportional to E_j, or of taking the range of sites where $U_j = U$ to be several times larger than that where $E_j \neq 0$. Such modifications change details of the results, such as the precise shape of the con-

ductance $g(\widetilde{V}_c, \widetilde{V}_s)$ as function of $\widetilde{V}_c$ or $\widetilde{V}_s$, but not the qualitative trends discussed in the main article, as long as U_j drops smoothly to zero near the edges of the CCR.

B. Model I

For model I, we choose the the hopping amplitude to be j-independent, $\tau_j = \tau$, while the on-site potential E_j describes a reflection-symmetric barrier within the CCR. Its shape is tunable between a double barrier describing a QD (Fig. S9**c**) and a single barrier describing a QPC (Fig. S9**d**) (thick dashed black lines). We have parametrized it as follows:

$$E_j = \begin{cases} 0\,, & \forall\ |j| \geq N', \\ (\widetilde{V}_s + \varepsilon_F)\left[2\left(\frac{|j|-N'}{j_s-N'}\right)^2 - \left(\frac{|j|-N'}{j_s-N'}\right)^4\right], & \forall\ j_0 \leq |j| \leq N', \\ \widetilde{V}_c + \varepsilon_F + \frac{\overline{\Omega}_x^2 j^2}{4\tau}\,\mathrm{sgn}(\widetilde{V}_s - \widetilde{V}_c), & \forall\ 0 \leq |j| < j_0. \end{cases} \tag{S15}$$

The sites $\pm j_0$ divide the CCR into two "outer regions", where the potential is a quartic polynomial in j, and an "inner region", where it is quadratic in j. In the latter, the magnitude of the curvature is governed by the parameter $\overline{\Omega}_x$ (≥ 0), which has units of energy. (The quadratic term for the inner region was chosen to have the form $\frac{1}{2}m\omega_x^2 x^2$ used in Ref. 5, with $\omega_x = \overline{\Omega}_x/\hbar$, $x = aj$ and $m = \hbar^2/(2\tau a^2)$ corresponding to the effective mass at the bottom of a tight-binding chain.) The shape of E_j is controlled by four independent parameters: (i) N', which sets the halfwidth of the CCR; (ii) j_s, which governs the width of the outer flanks of the potential; (iii) $\widetilde{V}_s$ and (iv) $\widetilde{V}_c$, which give the potential's height w. r. t. ε_F at the sites $j = \pm j_s$ and 0, respectively:

$$E_{\pm j_s} = \widetilde{V}_s + \varepsilon_F; \quad E_{j=0} = \widetilde{V}_c + \varepsilon_F\,. \tag{S16}$$

Once the four parameters N', j_s, $\widetilde{V}_s$ and $\widetilde{V}_c$ have been specified, the dependent parameters j_0 and $\overline{\Omega}_x$ are chosen such that E_j is a smooth function of j at the boundaries $\pm j_0$ between the inner and outer regions.

An electron incident at the chemical potential has energy ε_F w. r. t. to the bulk band bottom and hence sees a relative potential of height $E_j - \varepsilon_F$ at site j. For $\widetilde{V}_s > \widetilde{V}_c$, the relative potential describes a QD potential with two maxima of height $\widetilde{V}_s$ at $j = \pm j_s$ and a local parabolic minimum of height $\widetilde{V}_c$ at $j = 0$. For $\widetilde{V}_c > \widetilde{V}_s$ (the case of present interest), it describes a QPC potential with a single parabolic maximum at $j = 0$, of height $\widetilde{V}_c$. The crossover point between QD and QPC lies at $\widetilde{V}_s = \widetilde{V}_c$ (for which $\overline{\Omega}_x = 0$). Evidently $\widetilde{V}_c$ and $\widetilde{V}_s$ respectively mimick the role of the voltages applied to the central gates (V_c) and side gates (V_s) in the experiment (with $\widetilde{V}_{c,s} \propto -|e|V_{c,s}$).

Figure	N'	$\widetilde{V}_c[\tau]$	$\widetilde{V}_s[\tau]$	Ω_x	j_s
Fig. S6	150	-0.035 to 0.015	-0.25	0.016	60
Fig. S7	150	-0.032 to 0.01	-0.25	0.016	60
Fig. S9**a**-**b**	150	-2	-2	0	-
Fig. S9**c**	150	-0.6	0.6	0.0416	60
Fig. S9**d**	150	0.3	-0.3	0.023	60
Fig. S10**a**	150	-0.5	0.5	0.037	60
Fig. S10**b**	150	0.5	-0.5	0.027	60
Fig. S10**c**	150	-0.025	0	0.005	60
Fig. S10**d**	150	0.008	-0.25	0.016	60
Fig. S11	150	0	-0.25	0.016	60
Fig. S13	150	-0.016 to 0.006	-0.25	0.016	60
Fig. S14	150	-0.02 to 0.02	-0.25	0.016-0.048	60

Table I: Parameters used for model I [defined in Eq. (S15)] for the fRG results shown in various figures of the supplementary information.

We emphasize that the QPC barriers studied in this work are all *parabolic* near the top. For quantitative studies of the 0.7-anomaly using model I, we fix N', j_s and V_s, and tune the QPC from closed to open by lowering $\widetilde{V}_c$ past 0, at which the bare ($U = 0$) conductance g^0 equals 0.5. The width of the conductance step [see Fig. A1**k**, and Eq. (S30)] is governed by the curvature parameter at this point, $\Omega_x = \overline{\Omega}_x|_{\widetilde{V}_c=0}$, which we will simply call "curvature" henceforth. ($\overline{\Omega}_x$ itself changes slightly during this crossover, but for the barrier shapes used in this work this change is typically less than 10% between $\widetilde{V}_c = \pm\Omega_x$.) The curvature Ω_x also governs the exponential $\widetilde{V}_c$-dependence of $\widetilde{B}_*$ [Eq. (S35a)]. Note that formulas such as Eqs. (S30) and (S35a) would change for non-parabolic QPC barriers, e. g. barriers with a flat top. Studying the 0.7-anomaly for such situations would be an interesting extension of the present work, which we leave for the future[24].

C. Bare local density of states (LDOS)

In the main article we have argued that geometry strongly influences the 0.7-anomaly, via its effect on the local density of states (LDOS) and the van Hove ridge of the latter. Here we elaborate this in detail, by discussing the geometry-dependence of the noninteracting LDOS (for model I). We do so not only for the QPC barrier shape of present interest, but also for a QD barrier shape. This lays the ground for a subsequent comparison, presented in Sec. S-4 E below, of the LDOS structures of a QPC and a QD, which sheds light on the similarities and differences between the 0.7-anomaly and the Kondo effect.

The LDOS per spin species σ at energy ω (measured

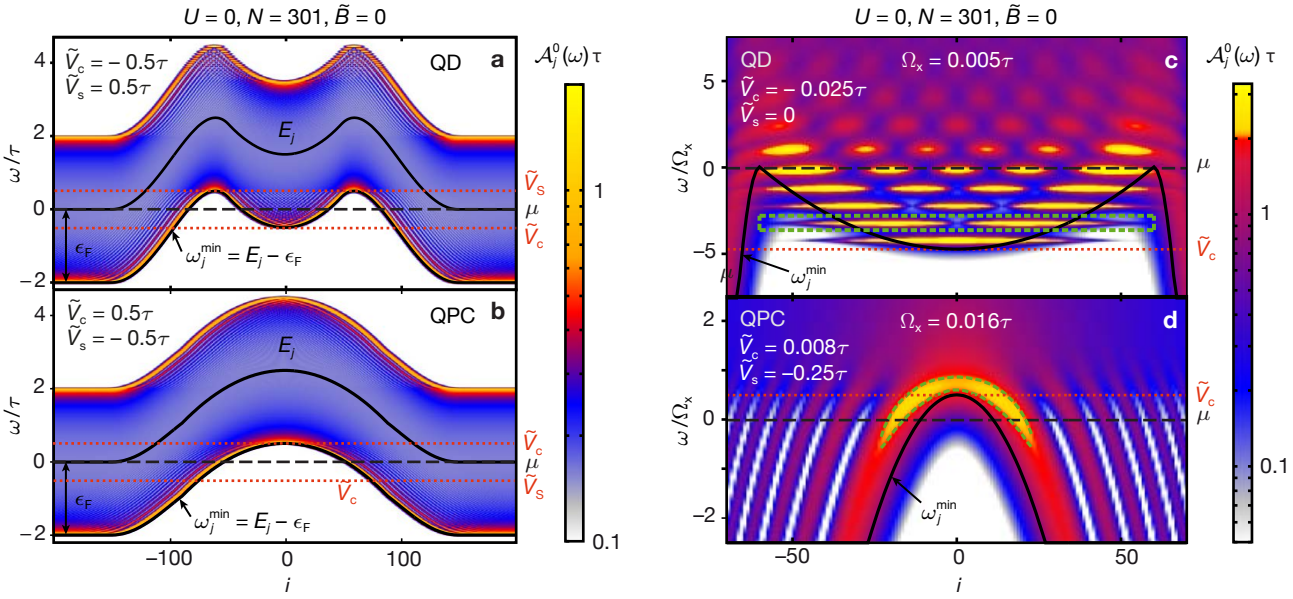

Figure S10: Model I: Noninteracting zero-field LDOS per spin species of **a,c**, a QD, and **b,d**, a QPC, for potential shapes shown by thin black lines (marked by black arrows) for $\omega_j^{\min} = E_j - \varepsilon_F$. (The logarithmic color scale shows $\mathcal{A}_j^0(\omega)$ smeared by a Lorentzian of width $\delta = 0.001\tau$, in order to render very sharp structures visible.) Panels **c**,**d** focus on the central region of the CCR and energies close to μ (black dashed lines); the $\widetilde{V}_c$- and $\widetilde{V}_s$-choices differ from those used in **a**,**b**. Thin green dashed lines in **c**,**d** indicate the shape of the "LDOS ridges" discussed in the text. For the KQD, they enclose an area in the j-ω plane on which the corresponding LDOS ridge has weight 1; for the QPC, they trace a contour along which $\mathcal{A}_j^{0,\mathrm{QPC}}(\omega) = 0.7$.

relative to the chemical potential μ) is defined as

$$\mathcal{A}_j^\sigma(\omega) = -\frac{1}{\pi}\mathrm{Im}\mathcal{G}_{jj}^{\sigma R}(\omega)\ , \qquad \text{(S17)}$$

where $\mathcal{G}_{ij}^{\sigma R}(\omega)$ is the Fourier transform of the retarded $T = 0$ propagator[25],

$$\mathcal{G}_{ij}^{\sigma R}(t) = -i\theta(t)\langle G|\{d_{i\sigma}(t), d_{j\sigma}^\dagger(0)\}|G\rangle\ , \qquad \text{(S18)}$$

where $|G\rangle$ is the model's ground state. In this subsection we will discuss only the spin-degenerate case of zero field ($\widetilde{B} = 0$) and zero interaction ($U_j = 0$). We thus drop the spin index σ (as in the main article) and instead put a superscript 0 on $\mathcal{A}_j^0(\omega)$ to denote the bare LDOS.

For $E_j = 0$, representing an infinite, homogenous, bulk tight-binding chain, the LDOS of Eq. (S17) is j-independent and equal to the 1D bulk LDOS,

$$\mathcal{A}_{\mathrm{bulk}}^0(\omega) = \frac{a}{\pi}\left[\frac{\partial k}{\partial \epsilon_k}\right]_{\epsilon_k=\omega+\mu}\ . \qquad \text{(S19a)}$$

This is nonzero only for $\omega_{\mathrm{bulk}}^{\min} < \omega < \omega_{\mathrm{bulk}}^{\max}$, where

$$\omega_{\mathrm{bulk}}^{\min} = -\varepsilon_F\ , \quad \omega_{\mathrm{bulk}}^{\max} = -\varepsilon_F + 4\tau\ , \qquad \text{(S19b)}$$

denote the bottom and top of the band, measured w. r. t. μ, respectively. Within these limits, it has the form

$$\mathcal{A}_{\mathrm{bulk}}^0(\omega) = \frac{1}{\pi\sqrt{(\omega_{\mathrm{bulk}}^{\max} - \omega)(\omega - \omega_{\mathrm{bulk}}^{\min})}}\ , \qquad \text{(S19c)}$$

shown in Fig. S9**b**, featuring square-root van Hove singularities near the band edges (yellow fringes in Fig. S9**b**). While the upper van Hove singularity (of unoccupied states) may be viewed as an artefact of describing the lowest subband using a tight-binding chain, the lower one is realistic for effective one-dimensional geometries; it would also arise, e. g., when using a free-electron model.

Now consider a nonzero potential E_j that is smooth on the scale of the lattice spacing, modelling a QD or QPC in the CCR, as shown by the thick black lines in Figs. S10**a-d**. The color scale in these figures indicates the corresponding j-dependent LDOS, $\mathcal{A}_j^0(\omega)$. The latter has an ω-dependence that, for fixed j, is reminiscent of the bulk case, but with several differences, caused by the spatial structure in E_j. First, the band edges now are j-dependent and follow the shape of the potential, with

$$\omega_j^{\min} = E_j - \varepsilon_F\ , \quad \omega_j^{\max} = E_j - \varepsilon_F + 4\tau\ . \qquad \text{(S20)}$$

In particular, the band bottom at the CCR center, $j = 0$, is given by $\omega_0^{\min} = \widetilde{V}_c$. Second, $\mathcal{A}_j^0(\omega)$ exhibits narrow fringes (visible clearly in Figs. S10**a-d**), due to the fact that the electronic wave functions form standing wave patterns. In the central part of the QD potential (Fig. S10**a**), and in the central part of the QPC potential for energies $\omega > \omega_{\mathrm{bulk}}^{\max}$ (Fig. S10**b**), these standing waves correspond to bound state wave functions. (For the case of the QPC these bound states are artefacts and they are avoided in model II.) In the outer regions of both QD and QPC potentials they correspond to Friedel oscilla-

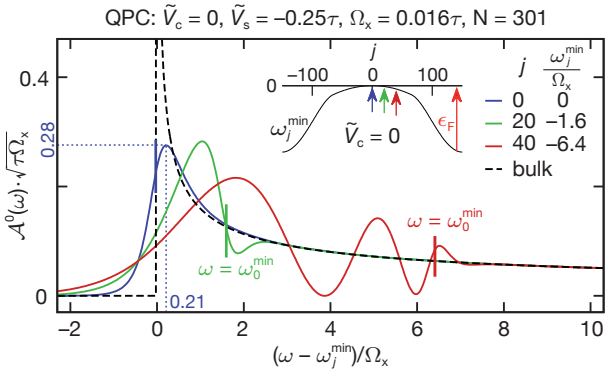

Figure S11: Inset: The band bottom $\omega_j^{\min}$ (black line) as function of j, for a 301-site CCR with a parabolic QPC barrier (model I) with curvature Ω_x and height $\widetilde{V}_c = \omega_0^{\min} = 0$. Main plot: Energy dependence of the LDOS near the band bottom, showing $\mathcal{A}^0_{\rm bulk}(\omega)$ (dashed), and $\mathcal{A}_j^{0,\rm QPC}(\omega)$ (solid) for three j-values near the center, all plotted as functions of $(\omega-\omega_j^{\min})/\Omega_x$ (blue line corresponds to Fig. 1 in Ref. 23). Arrows of matching colors in the inset indicate the corresponding values of j (namely 0, 20 and 40). The short, heavy, colored vertical lines in the main panel indicate where the energy coincides with the barrier top, $\omega = \omega_0^{\min}$; the corresponding values of the x-coordinate $(\omega_0^{\min} - \omega_j^{\min})/\Omega_x$ (namely 0, 1.6 and 6.4) give the remaining barrier height as seen from site j. In the bulk, $\omega_j^{\min} = -\varepsilon_{\rm F}$. The peak of $\mathcal{A}_j^{0,\rm QPC}(\omega)$ lies at an energy $\omega_j^{\rm H} = \omega_j^{\min} + \mathcal{O}(\Omega_x)$. For $j = 0$ it lies at $\omega_0^{\rm H} = 0.21\Omega_x$ and has height $0.28/\sqrt{\tau\Omega_x}$ (dotted blue lines). Note that $\mathcal{A}_j^{0,\rm QPC}(\omega)$ matches $\mathcal{A}^0_{\rm bulk}(\omega)$ once the energy ω lies above $\omega_0^{\min}$ by more than $\mathcal{O}(\Omega_x)$, corresponding to free propagation above the barrier.

tions. Third, the van Hove singularities are somewhat smeared out on the outer flanks of the QD, and throughout the entire QPC, in the latter case on a scale set by Ω_x (see Fig. S11).

For the rest of this subsection, we focus on the QPC barrier of Figs. S10**b**,**d**. (The QD barrier of Figs. S10**a**,**c** is revisited in Sec. S-4 E below, where we compare its LDOS to that of a QPC.) For a QPC, $\mathcal{A}_j^{0,\rm QPC}(\omega)$ depends *smoothly* on ω and j near the center of the CCR, its weight being concentrated along a curved, broad "van Hove ridge" (framed by the green dashed lines in Fig. S10**d**). This ridge originates from a van Hove singularity just above the band bottom that has been pushed upward by the QPC potential barrier. The van Hove ridge has limited spatial extent when traversed at constant ω, reflecting the limited spatial size of the QPC. At the outside flanks of the CCR barrier, the tails of the ridge split up into discrete fringes, representing Friedel oscillations associated with standing waves that build up near the barrier (as also seen in Figs. S10**a**,**b**). For given j, the ω-dependence of the van Hove ridge, shown in Fig. S11**,** is asymmetric w. r. t. to its maximum, with a steep, exponentially decaying flank below the maximum, and above it a long tail, whose envelope decays as

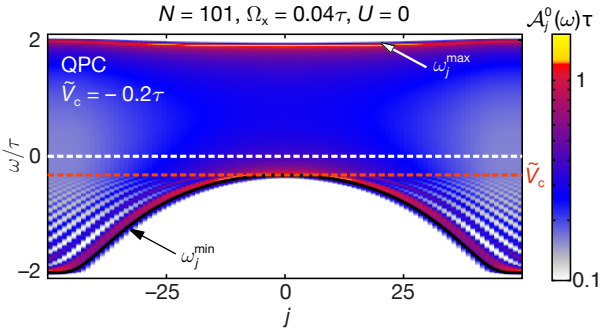

Figure S12: Noninteracting zero-field LDOS per spin species, $\mathcal{A}_j^0(\omega)$, shown on a logarithmic color scale, for the QPC model II defined by Eqs. (S22) and (S23). The thin black line (marked by black arrow) indicates the lower band edge, $\omega_j^{\min}$ [Eq. (S24)]. The curvature of the lower and upper band edges is, respectively, negative and positive throughout the CCR, ensuring that no bound states occur.

$[\tau(\omega-\omega_j^{\min})]^{-1/2}$, reflecting the ω-asymmetry of the bulk van Hove singularity of Eq. (S19). The divergence of the latter is cut off here, due to the absence of translational invariance, on a scale set by the barrier curvature. Indeed, the maximum value taken by the van Hove peak in $\mathcal{A}_j^{0,\rm QPC}(\omega)$ occurs at an energy, say $\omega_j^{\rm H}$, that lies above the lower band edge by an amount of order Ω_x,

$$\omega_j^{\rm H} = \omega_j^{\min} + \mathcal{O}(\Omega_x)\,. \tag{S21}$$

For example, for a purely parabolic barrier top, the van Hove peak in $\mathcal{A}_{j=0}^{0,\rm QPC}(\omega)$, the LDOS at the center of the QPC, lies at $\omega_0^{\rm H} = \omega_0^{\min} + 0.21\Omega_x$. In that case, the van Hove peak lies precisely at the chemical potential, $\omega_0^{\rm H} = 0$, when $\widetilde{V}_c = -0.21\Omega_x$.

Eq. (S21) implies not only that the van Hove peak energy depends on Ω_x, but also that its height (i. e. the maximum value of the LDOS) scales as $1/\sqrt{\tau\Omega_x}$. As a consequence, all local quantities that depend on $\mathcal{A}_j^{0,\rm QPC}(\omega)$, such as the local magnetic susceptibility χ_j, depend on Ω_x, too. In this way they acquire an explicit dependence on the shape of the QPC barrier.

D. Model II

In this section we describe model II, used for all numerical results (fRG and SOPT) presented in the main article. For model II, designed to model exclusively a QPC, we have modified the choice of E_j and τ_j in two minor ways relative to model I of Sec. S-4 B, which turn out to facilitate SOPT calculations. The two changes, described below, are designed (i) to allow using a shorter CCR while maintaining a small curvature Ω_x at the barrier top, and (ii) to avoid the occurrence of artificial bound states in the bare density of states of the QPC (such as those seen in Fig. S10**b** near the upper band edge, for energies $\omega > \omega_{\rm bulk}^{\max}$).

(i) Modified potential shape: We define the onsite potential E_j by

$$E_j = \begin{cases} 0\,, & \forall \quad N' \leq |j|\,, \\ \dfrac{(\widetilde{V}_{\rm c}+\varepsilon_{\rm F})}{1+2b}\exp\left[-\dfrac{\left(\frac{j}{N'}\right)^2}{1-\left(\frac{j}{N'}\right)^2}\right] & \forall \quad |j| \leq N'\,, \end{cases} \tag{S22}$$

where the parameter b is defined in *(ii)* below. This yields a smooth parabolic barrier near the CCR center and rapidly decaying flanks, allowing the CCR to be chosen shorter than for the potential of Eq. (S15). Using a short CCR is advantageous in particular for SOPT calculations: due to the matrix structure of the Greens function and the summation/integration over internal frequencies, the computation of the self-energy Σ and the vertex correction P needed for SOPT [see Eq. (S53) and Eq. (S52)] is rather time-consuming.

(ii) Modified hopping: For model I, the QPC potential barrier of Eq. (S15) (at $\widetilde{B}=0$) yields a bare band whose upper edge has a maximum in energy at $j=0$, causing a large number of bound states in the energy range $\omega \in [\omega_{\rm bulk}^{\rm max}, \omega_{\rm bulk}^{\rm max}+\widetilde{V}_{\rm c}]$ (visible as narrow fringes in Fig. S10). Though these artificial bound states are completely irrelevant for the physics of the 0.7-anomaly, the corresponding poles in the bare Green's functions nevertheless would have to be treated with due accuracy in the energy integrals involved in SOPT. To avoid the occurrence of such poles, model II takes the hopping matrix element τ_j in Eq. (S11) to be site-dependent within the CCR, $\tau_j = \tau - \delta\tau_j$, involving a smooth (adiabatic) reduction proportional to the local barrier height:

$$\delta\tau_j = \tfrac{1}{2}(E_j + E_{j+1})b \quad (>0)\,, \quad -N' \leq j < N', \tag{S23}$$

and $\delta\tau_j = 0$ otherwise. Then the lower and upper band edges are approximately given by

$$\left.\begin{matrix}\omega_j^{\rm min} \\ \omega_j^{\rm max}\end{matrix}\right\} = -\mu \mp 2\overline{\tau}_j + E_j\,, \quad \overline{\tau}_j = \tfrac{1}{2}(\tau_j + \tau_{j-1}). \tag{S24}$$

Here $\bar{\tau}_j$, the average hopping matrix element involving site j, is approximately equal to $\overline{\tau}_j \simeq \tau - bE_j$, since the potential varies smoothly with j. Eq. (S24) implies a j-dependent bandwidth, $4\overline{\tau}_j$. For the upper band edge $\omega_j^{\rm max}$, the upward shift contributed by E_j inside the CCR is counteracted by a downward shift, contributed by $2\overline{\tau}_j$, of $-2\delta\overline{\tau}_j \simeq -2bE_j$. The latter can be ensured to overcompensate the former by choosing the numerical factor b to be larger than $1/2$ (we choose $b=0.55$). Then the upper band edge $\omega_j^{\rm max}$ throughout the CCR lies *below* the bulk band edge $\omega_{\rm bulk}^{\rm max}$, ensuring that no bound states occur near the upper band edge. This is illustrated in Fig. S12, which is to be contrasted to the bound states seen in Fig. S10**b** for model I, with j-independent hopping.

The prefactor $1/(1+2b)$ in Eq. (S22) ensures that $\widetilde{V}_{\rm c}$ corresponds to the effective barrier height w. r. t. the chemical potential, $\widetilde{V}_{\rm c} = \omega_{j=0}^{\rm min}$ [as is the case for Eq. (S15)]. Finally, the parameter Ω_x is defined as the curvature of the band bottom at $\widetilde{V}_{\rm c}=0$, obtained by expanding Eq. (S24) to second order in j [in analogy to Eq. (S15)]: $\omega_j^{\rm min}|_{\widetilde{V}_{\rm c}=0} \simeq -\Omega_x^2 j^2/(4\overline{\tau}_0)$. For the choice $\mu=0$ used here, $\overline{\tau}_0 \simeq \tau/(1+2b)$. We have checked that with this definition of Ω_x, the bare transmission probability for model II, calculated numerically, agrees well with the analytic prediction of Eq. (S30) below (and that of model I). For all calculations performed in this with with model II, we chose $N'=50$ and $b=0.55$, in which case $\Omega_x = 0.04\tau$.

We emphasize that transport and local properties are not modified in any essential way by the changes (i) and (ii) of model II w. r. t. model I. Their effect is solely to reduce the computation time.

E. Comparison: bare LDOS of QPC and QD

In this subsection, we offer a detailed comparison of the bare LDOS structures for a QPC and a QD. They are shown in Figs. S10**d** and S10**c**, respectively, which focus on the CCR-center and energies near $\omega=0$. They evidently exhibit numerous differences, but also some similarities. These are key to understanding the differences and similarities between the 0.7-anomaly and the Kondo effect.

For a QPC, $\mathcal{A}_j^{0,\rm QPC}(\omega)$ exhibits a prominent, smooth van Hove ridge (Fig. S10**d**), as discussed in detail in Sec. S-4 C. In contrast, for a QD, $\mathcal{A}_j^{0,\rm QD}(\omega)$ has appreciable weight only along a set of "ridges" at *discrete* energies, one of which is marked by the green box in Fig. S10**c**. Each ridge is associated with a discrete eigenstate of the bare QD potential: it is characterized by a discrete eigenenergy, say ω_α, and its spatially confined, oscillatory j-dependence reflects that of $|\psi_\alpha(j)|^2$, where the wavefunction $\psi_\alpha(j)$ represents a confined standing wave. Its spatial extent is approximately set by the classical turning points (where $\omega_\alpha = \omega_j^{\rm min}$), though it tunnels a bit beyond these. Each ridge has a small but nonzero width in ω, due to tunneling into the leads outside the QD, and a quantized total weight of 1 when j-summed over the range of $\psi_\alpha(j)$ and ω-integrated over its width, as indicated by the green box in Fig. S10**c**.

(Parenthetic remark: When interactions are turned on, the detailed shape of the LDOS will change, since barrier heights and energy levels will be renormalized. Nevertheless, the full $\mathcal{A}_j(\omega)$ will retain the generic properties illustrated in Figs. S10**c**,**d**, namely discrete ridges for the QD and a single broad ridge for the QPC. Many-body correlations may lead to additional fine structures in the full LDOS, such as a narrow Kondo resonance at the Fermi energy for $\mathcal{A}_j^{\rm KQD}(\omega)$. However, such many-body effects do not concern us at the present qualitative level of argumentation, which merely seeks to identify the geometric

prerequisites for their occurrence.)

The most important difference between the bare LDOS of a QD and a QPC lies in the following fact, evident from Figs. S10**a-d**: near the center of the CCR, $\mathcal{A}_j^{0,\mathrm{QD}}(\omega)$ consists of a series of discrete ridges of quantized weight, whereas $\mathcal{A}_j^{0,\mathrm{QPC}}(\omega)$ does not, being dominated by just a single ridge of nonquantized weight. The physical reason for this difference clearly is that a QD constitutes a closed structure that hosts discrete, localized states, whereas a QPC, being truly open, does not. This difference is responsible for the different behavior between a KQD and a QPC for large fields: for $\widetilde{B} \gg \widetilde{B}_*$, the magnetization of a KQD saturates, whereas that of a QPC does not (as seen in Fig. A1d and its inset). This behavior reflects the fact that for the KQD the spin of only the single odd electron in the topmost nonempty level is being polarized in a large field, whereas for the QPC, whose LDOS has no discrete structure, there is no intrinsic limit for the magnitude of the magnetization.

While the differences between the LDOS ridge structures of KQD and QPC matter at high energies, the low-energy behavior ($\widetilde{B}, \widetilde{T} \ll B_*$) is governed by a generic *common* feature shared by the LDOS of both geometries: the very existence of a $\widetilde{V}_\mathrm{c}$-tunable ridge with a strongly peaked dependence on both ω and j. (Details such as the number of such ridges or their internal spatial structure are irrelevant for the ensuing argument.) The existence of such a ridge guarantees a strong magnetic response in both the conductance and the magnetization when $\widetilde{V}_\mathrm{c}$ is tuned such that the (interaction-shifted version of the) ridge is located energetically somewhat below μ. For a KQD, this is the local moment regime; for the QPC, it is the regime where $g \simeq 0.7$. This situation is particularly inductive to a strong local magnetic response, for two reasons: First, when spin symmetry is broken by turning on a magnetic field (say $\widetilde{B} > 0$), the $\widetilde{B}$-induced surplus of spin-up over spin-down electrons is enhanced by the presence of an LDOS ridge below the chemical potential, because this ridge constitutes a large density of states in a confined region of space. Second, interactions will generally act to further increase this surplus by repelling spin-down electrons, and will be aided in this by the fact that the ridge, and hence the region in which the surplus is large, has a limited spatial extent.

This microscopic mechanism generates a strong, local magnetic response *irrespective* of whether the LDOS ridge has quantized weight or not. Thus, this mechanism applies equally to a KQD and a QPC, and in this respect the low-energy behavior of the Kondo effect and the 0.7-anomaly are indeed similar. This similarity was first pointed out in Ref. 26 and emphasized, in particular, by Meir and collaborators[17–19]: the "narrow transmission resonances above the barrier" or "quasi-bound state" evoked in their arguments correspond to the van Hove ridge in $\mathcal{A}_j^{0,\mathrm{QPC}}(\omega)$ described above. Indeed, the asymmetric bare LDOS peak at the QPC barrier center found by us [Fig. S11**,** blue line for $\mathcal{A}_{j=0}^{0,\mathrm{QPC}}(\omega)$] is qualitatively similar to that found in Ref. 17 [see Fig. 3a there, right inset, solid line for $\nu_\uparrow(\epsilon)$] by spin-density-functional theory (SDFT) in a small applied field. Moreover, the van Hove ridge in our Figs. S10**b**,**d** corresponds to the bright spot seen in the center of Fig. 3a of Ref. 19 by Rejec and Meir, which shows the full spin-up LDOS $\mathcal{A}_j(\omega)$ as function of position and energy, again calculated by SDFT in a small applied field. Though SDFT includes interactions and our bare LDOS does not, interactions affect the minority species much more strongly than the majority species. We therefore expect that the geometry-dependence of the majority LDOS obtained from SDFT should be similar to that of a noninteracting theory. Thus, we believe that Meir and Rejec's "quasi-bound states" are synonymous to our "van Hove ridges". (We somewhat prefer the latter nomenclature, since it indicates the origin of these LDOS structures.) It would be highly desirable to have a plot similar to Fig. S10**d** for the full $\mathcal{A}_j^{\mathrm{QPC}}(\omega)$ calculated using fRG, but its energy dependence is not accessible by static fRG. To obtain a first impression, we have calculated it using perturbation theory, see Fig. A3**g**,**h**; calculating it with Keldysh fRG would be an interesting goal for future studies.

We wish to emphasize that the details of the magnetic response of a KQD and a QPC will be similar *only as long as the conditions* $\widetilde{B}, \widetilde{T} \ll \widetilde{B}_*$ *hold*; once they are violated, the differences in the LDOS ridges, discrete for QD vs. continuous for QPC, begin to matter. This caveat, not discussed in Refs. 17–19, prevents the similarity between Kondo effect and 0.7-anomaly from extending to the regime of large energies.

A detailed comparative study of the similarities and differences in the behavior of a KQD and QPC, all originating from the similarities and differences between their LDOS ridges, will be published elsewhere[1].

S-5. THE LOW-ENERGY SCALE $\widetilde{B}_*$

This section covers the influence of geometry and interactions on the low-energy scale $\widetilde{B}_*$ for a QPC. In Sec. S-5 A we show that the exponential dependence of the low-energy scale $\widetilde{B}_*(\widetilde{V}_\mathrm{c})$ has a purely geometric origin, and contrast this to the more complicated case of the Kondo temperature for a KQD. Sec. S-5 B discusses the effects of interactions on $\widetilde{B}_*$ and $\widetilde{T}_*$ for a QPC. Finally, Sec. S-5 C discusses the extent to which the interaction parameter U itself depends on the 2D potential landscape.

A. Exponential $\widetilde{V}_\mathrm{c}$-dependence of $\widetilde{B}_*$

In the main article we reported that for a QPC the low-energy scale $B_*(V_\mathrm{c})$ depends exponentially on V_c (see Eq. (A3), Figs. A2**a**, **c**, **e**). The same is true for $T_*(V_\mathrm{c})$ (see Eq. (A3), Figs. A2**d**, **f**), as was first found in Ref. 26. In this subsection, we explain the origin of this exponential V_c-dependence. It is present already for the nonin-

teracting ($U = 0$) version of our model, hence we begin by discussing the latter.

According to the Landauer-Büttiker formula, the noninteracting differential conductance $g^0_{\rm nl}(\widetilde{T},\widetilde{B},\widetilde{V}_{\rm sd})$ as a function of temperature $\widetilde{T} = k_{\rm B}T$, magnetic field $\widetilde{B} = |g_{\rm el}|\mu_{\rm B}B$ and source-drain voltage $\widetilde{V}_{\rm sd} = -|e|V_{\rm sd}$ is given by

$$g^0_{\rm nl}(\widetilde{T},\widetilde{B},\widetilde{V}_{\rm sd}) = \frac{d}{d\widetilde{V}_{\rm sd}}\frac{1}{2}\sum_{\sigma=\pm}\int_{-\infty}^{\infty} d\omega\, \mathcal{T}(\omega+\tfrac{1}{2}\sigma\widetilde{B}) \times\Big[f(\omega-\tfrac{1}{2}\widetilde{V}_{\rm sd}) - f(\omega+\tfrac{1}{2}\widetilde{V}_{\rm sd})\Big] \quad \text{(S25)}$$

where $f(\omega) = [e^{\omega/\widetilde{T}}+1]^{-1}$ is the Fermi function, and $\mathcal{T}(\omega)$ is the noninteracting transmission probability across the QPC barrier of a lead electron incident with energy ω w. r. t. μ, at $\widetilde{B} = 0$. Let us expand it in powers of energy:

$$\mathcal{T}(\omega) = \mathcal{T}^{(0)} + \mathcal{T}^{(1)}\omega + \frac{1}{2}\mathcal{T}^{(2)}\omega^2 + \dots\,, \quad \text{(S26)}$$

where $\mathcal{T}^{(0)} = \mathcal{T}(0)$ is the transmission probability at the chemical potential. Inserting Eq. (S26) into (S25) leads to the following expression for the leading dependence of the bare conductance on $\widetilde{T}^2$, $\widetilde{B}^2$ and $\widetilde{V}^2_{\rm sd}$ (at fixed $\widetilde{V}_{\rm c}$ and $\widetilde{V}_{\rm s}$)

$$\frac{g^0_{\rm nl}(\widetilde{T},\widetilde{B},\widetilde{V}_{\rm sd})}{\mathcal{T}^{(0)}} = \left[1-\left(\frac{\widetilde{T}}{\widetilde{T}^0_*}\right)^2-\left(\frac{\widetilde{B}}{\widetilde{B}^0_*}\right)^2-\left(\frac{\widetilde{V}_{\rm sd}}{\widetilde{V}^0_{\rm sd*}}\right)^2\right], \quad \text{(S27)}$$

with low-energy scales $\widetilde{T}^0_*$, $\widetilde{B}^0_*$ and $\widetilde{V}^0_{\rm sd*}$ given by

$$-\frac{8\mathcal{T}^{(0)}}{\mathcal{T}^{(2)}} = \left(\widetilde{B}^0_*\right)^2 = \left(\widetilde{V}^0_{\rm sd*}\right)^2 = \frac{4\pi^2}{3}\left(\widetilde{T}^0_*\right)^2 . \quad \text{(S28)}$$

Their mutual ratios hence are independent of $\widetilde{V}_{\rm c}$:

$$\frac{\widetilde{B}^0_*}{\widetilde{T}^0_*} = \frac{2\pi}{\sqrt{3}}, \qquad \frac{\widetilde{V}^0_{\rm sd*}}{\widetilde{B}^0_*} = 1\,. \quad \text{(S29)}$$

(Remark: Depending on the height and shape of the potential barrier, $\mathcal{T}^{(2)}$ can be either negative or positive; in the latter case, the scales $\widetilde{B}^0_*$, $\widetilde{T}^0_*$ and $\widetilde{V}^0_{\rm sd*}$ as defined here would be imaginary. In the following, we are interested only in the former case.)

Now consider a purely parabolic QPC potential barrier with height $\widetilde{V}_{\rm c}$ and longitudinal curvature $\frac{1}{4\tau}\Omega_x^2$ [as in Eq. (S15)]. Then the bare transmission $\mathcal{T}(\omega)$ at $\widetilde{B} = 0$ is given by[5]

$$\mathcal{T}(\omega) \simeq \frac{1}{e^{-2\pi(\omega-\widetilde{V}_{\rm c})/\Omega_x}+1}\,. \quad \text{(S30)}$$

Recall that $\widetilde{V}_{\rm c} = \omega^{\rm min}_{j=0}$ is the height of the band bottom's maximum at the central site w. r. t. the chemical potential. When $\widetilde{V}_{\rm c}$ is decreased to open up the QPC, the bare transmission of an electron incident at the chemical potential ($\omega = 0$) increases past $\mathcal{T}(0) = 0.5$ when $\widetilde{V}_{\rm c}$ decreases past 0. [We obtained Eq. (S30) from Eq. (4) of Ref. 5, which in turn was derived by a semiclassical treatment of transmission through a parabolic barrier[27,28], assuming a quadratic dispersion of the form $p^2/2m$. The latter assumption is applicable for our situation in the limit that our tight-binding band is much wider than the energy range over which the transmission changes rapidly, $\tau \gg \Omega_x$. This allows a quadratic approximation for the dispersion [Eq. (S12)] near the band bottom, $\epsilon_k \simeq -2\tau + \tau k^2a^2$, implying an effective mass of $m = \hbar^2/(2\tau a^2)$.]

The bare dimensionless conductance at $\widetilde{B} = \widetilde{T} = \widetilde{V}_{\rm sd} = 0$, viewed as function of $\widetilde{V}_{\rm c}$, is then given by

$$g^0_{\rm nl} = g^0_{\rm nl}(0,0,0) = \mathcal{T}^{(0)} = \frac{1}{e^{-2\pi\widetilde{V}_{\rm c}/\Omega_x}+1}\,. \quad \text{(S31)}$$

Let us now focus on the regime of negative $\widetilde{V}_{\rm c} = -|\widetilde{V}_{\rm c}|$, where for the quadratic potential top considered here the bare magnetoconductance is strictly negative. Evaluating Eq. (S28) for $\widetilde{B}^0_*$ using Eq. (S30), one finds:

$$\widetilde{B}^0_* = \frac{\Omega_x}{\pi}\sqrt{2\coth(\pi|\widetilde{V}_{\rm c}|/\Omega_x)}\,e^{\pi|\widetilde{V}_{\rm c}|/\Omega_x} \quad \text{(S32a)}$$

$$= \frac{\Omega_x}{\pi}\frac{1}{\sqrt{g^0-1/2}}\sqrt{\frac{g^0}{1-g^0}}\,. \quad \text{(S32b)}$$

(The second line follows from the first by inverting Eq. (S31).) Expression (S32a) for the low-energy scale in the absence of interactions, $\widetilde{B}^0_*$, agrees to within a few percent with our numerical calculations for $U = 0$, shown by the black dashed line in Fig. S13**a**. It states that $\widetilde{B}^0_*$ diverges both when $|\widetilde{V}_{\rm c}| \to 0^+$ (i. e. $g^0 \to 1/2$ from above) and when $|\widetilde{V}_{\rm c}|/\Omega_x \gg 1$ (i. e. $g^0 \to 1$ from below). Between these two limiting cases $\widetilde{B}^0_*$ has a minimum, which turns out to occur at a bare conductance of $g^0_* = 1/\sqrt{2} \simeq 0.707$.

The message of the above analysis is that the experimentally observed exponential $V_{\rm c}$-dependence of the low-energy scales B_* and T_* reported in the main article (and for T_* also in Ref. 26) has a *purely geometric origin, which can already be understood within a noninteracting model.* It arises simply because for a quadratic barrier the transmission amplitude above the barrier depends exponentially on its height (as can be made explicit in a semiclassical WKB treatment of the transmission problem[27,28]). Moreover, the scale for the $\widetilde{V}_{\rm c}$-dependence is set solely by Ω_x, the curvature at the top of the barrier [Eq. (S15)].

The fact that for a QPC the exponential $\widetilde{V}_{\rm c}$-dependence of $\widetilde{B}_*$ can be found without considering interactions at all stands in striking contrast to the case of a KQD: there $\widetilde{B}_*$ is proportional to the Kondo temperature, which likewise depends exponentially on $\widetilde{V}_{\rm c}$, but the exponent is quadratic in $\widetilde{V}_{\rm c}$, and the scale of its $\widetilde{V}_{\rm c}$-dependence is set by the interaction strength U and effective level width Γ. To be explicit, for the single-impurity

Anderson model, with level position $\varepsilon_d = \widetilde{V}_c$, the Kondo temperature corresponding to $\widetilde{T}_*$ is given by[29]

$$\widetilde{T}_K = \sqrt{U\Gamma/2}\exp\left[\frac{\pi\widetilde{V}_c(\widetilde{V}_c+U)}{2\Gamma U}\right] . \qquad \text{(S33)}$$

It arises as the low-energy scale $\widetilde{T}_K \propto e^{-1/j_{\rm eff}}$ characterizing the onset of a logarithmic infrared divergence that occurs when doing perturbation theory in the effective exchange interaction between the spins of a local moment and a conduction band. The form of the corresponding effective dimensionless exchange coupling $j_{\rm eff}$, given by

$$j_{\rm eff} = \frac{2\Gamma}{\pi}\left[\frac{1}{\widetilde{V}_c+U} - \frac{1}{\widetilde{V}_c}\right] , \qquad \text{(S34)}$$

is found by a Schrieffer-Wolff transformation. Evidently, such KQD results can not be obtained without considering the role of interactions from the outset. In contrast, for a QPC the origin of the exponential $\widetilde{V}_c$-dependence of $\widetilde{B}_*$ is decidedly different and can be understood already for a noninteracting theory, as described above. In particular, at high energies a QPC does *not* display local-moment behavior, so that the corresponding logarithmic infrared divergence characteristic of the Kondo effect does not occur.

Having made this point, we hasten to add that $\widetilde{B}_*$ is of course affected by interactions for a QPC too, albeit less severely than for a KQD. The role of interactions is discussed in the next subsection.

B. Effects of interactions on $\widetilde{B}_*$ and $\widetilde{T}_*$

While the fact that the low-energy scales $\widetilde{B}_*$, $\widetilde{T}_*$ and $\widetilde{V}_{\rm sd*}$ for a QPC depend exponentially on gate voltage, as $e^{\pi|\widetilde{V}_c|/\Omega_x}$, has an elementary geometric origin, the behavior of the pre-exponential factor is more subtle: quite generally this pre-exponential factor will depend on the interaction strength U and gate voltage $\widetilde{V}_c$. A detailed theoretical analysis of this issue is beyond the scope of the present paper. Here we just want to make two points, the first regarding the ratio $\widetilde{B}_*/\widetilde{T}_*$, the second regarding the U-dependence of $\widetilde{B}_*$.

The ratio $\widetilde{B}_*/\widetilde{T}_*$: When interactions are turned on, the effects of finite $\widetilde{B}$ or finite $\widetilde{T}$ are, in general, not equivalent: Finite $\widetilde{B}$ shifts the effective barrier height seen by spin-up and spin-down electrons in opposite directions, in a way that is enhanced by interactions (which amplifies the imbalance between spin up and spin down), however without opening up the possibility of inelastic scattering. Finite $\widetilde{T}$ causes an effective increase in barrier height, too, due to an increase in density near the barrier center (because the LDOS is ω-asymmetric there), but it does not involve any imbalance between spin-up and -down. Moreover, finite $\widetilde{T}$ also leads to inelastic scattering. In lowest-order perturbation theory for the self-energy (Sec. S-7), shifts in barrier height (both $\widetilde{B}$-induced, spin-asymmetric and $\widetilde{T}$-induced, spin-symmetric shifts) are described by the Hartree contribution, and $\widetilde{T}$-induced inelastic scattering by the Fock contribution [see Eq. (S53)]. In general, the relative strength of these two effects will depend not only on U but also on gate voltage. Since the strength of the (negative) conductance response to increasing $\widetilde{B}$ or $\widetilde{T}$ is characterized by $1/\widetilde{B}_*$ or $1/\widetilde{T}_*$, respectively, the ratio $\widetilde{B}_*/\widetilde{T}_*$, too, will in general likewise depend not only on U, but also directly on $\widetilde{V}_c$.

In the light of the above comments, it is all the more remarkable that the experimentally observed ratio $B_*/\widetilde{T}_*$ *does*, in fact, become essentially independent of V_c in the V_c-regime well below V_{c0}, where $g \to 1$ (compare thin grey and black lines in Fig. A2**f**). In the main article we have already pointed out that this V_c-independence of B_*/T_* for $g \simeq 1$ is characteristic of the Fermi-liquid behavior expected from Nozières' treatment of the Kondo problem in the limit $B, T \ll T_K$.

Once the condition $g \simeq 1$ is relaxed, the experimentally determined B_*/T_* does acquire a dependence on V_c, in accord with the expectations stated above. Indeed, in Fig. A2**f** the measured ratio B_*/T_* *increases* with increasing $\widetilde{V}_c$ as B_* and T_* approach their minimal values. Remarkably, our model qualitatively reproduces this behavior when we treat interactions using SOPT (compare the lines for $\widetilde{B}_*$ and $\widetilde{T}_*$ in Fig. A2**d**). An increase in $\widetilde{B}_*/\widetilde{T}_*$ means that the conductance reduction induced by increasing $\widetilde{T}$ grows relative to that induced by increasing $\widetilde{B}$, implying that inelastic scattering [Fock term, diagram **c** in Eq. (S53)] gains importance relative to the $\widetilde{B}$-induced enhancement of the barrier height [Hartree terms, diagrams **a** and **b** in Eq. (S53)]. Moreover, Fig. S4 above shows that $\widetilde{B}_*/\widetilde{T}_*$ decreases with increasing U, implying that in general interactions have a stronger effect on the low-$\widetilde{B}$ dependence of the conductance than on its low-$\widetilde{T}$ dependence.

U-dependence of $\widetilde{B}_*$: We have used fRG to explore in some more detail how interactions affect the $\widetilde{V}_c$-dependence of $\widetilde{B}_*$ for a QPC. (Similar studies of $\widetilde{T}_*$ are not possible using static fRG, but would be worth pursuing by Keldysh fRG). As in Sec. S-5 A above, we focus on the regime $g \simeq 1$ (say $|\widetilde{V}_c| \gtrsim 0.75\Omega_x$). Our results for this regime can be summarized by stating that for U small enough to be treatable by fRG, $\widetilde{B}_*$ shows the following behavior:

$$\widetilde{B}_*(\widetilde{V}_c, U) \simeq \frac{\sqrt{2}\Omega_x}{\pi} e^{-F(U)} e^{\pi|\widetilde{V}_c|/\Omega_x} , \qquad \text{(S35a)}$$

$$F(U) \simeq (0.8 \pm 0.05)U/\sqrt{\tau\Omega_x} . \qquad \text{(S35b)}$$

The behavior of Eq. (S35a) is illustrated in Fig. S13**a**, which shows $\ln(\widetilde{B}_*)$ as function of $|\widetilde{V}_c|/\Omega_x$ for several values of U: for $|\widetilde{V}_c|/\Omega_x \gtrsim 0.75$ the resulting lines all have roughly the same slope, but are shifted downward

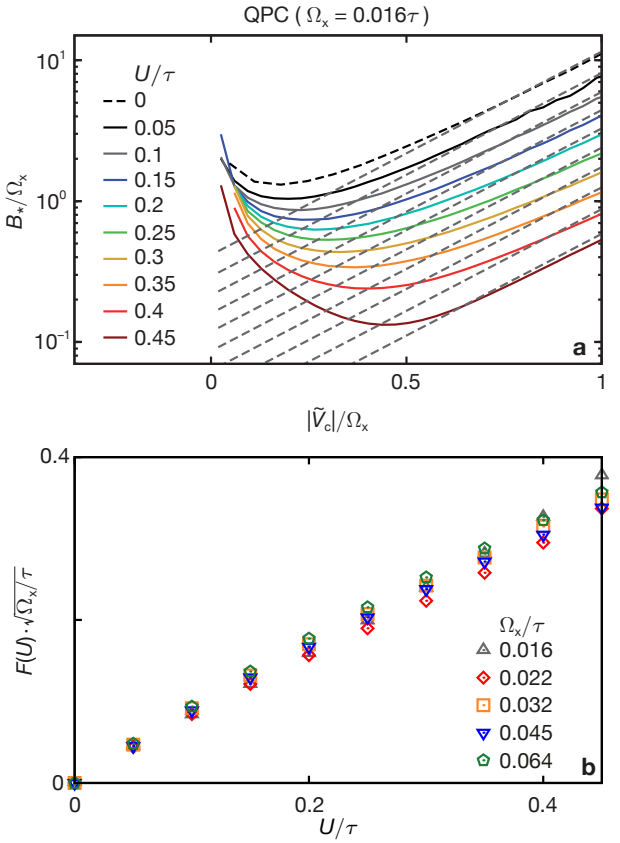

Figure S13: Effect of interaction strength U on the low-energy scale $\widetilde{B}_*$, in the regime of negative $\widetilde{V}_c = -|\widetilde{V}_c|$ (calculated for model I using static fRG). **a**, $\widetilde{B}_*/\Omega_x$ as function of $|\widetilde{V}_c|/\Omega_x$. Grey dashed lines indicate linear fits of $\ln(\widetilde{B}_*)$ vs. $|\widetilde{V}_c|/\Omega_x$ in the range $0.8 \leq |\widetilde{V}_c|/\Omega_x < 1$, the offsets of which yield $F(U)$. **b**, The function $F(U)$ vs. U for several choices of Ω_x, plotted in scaled fashion to illustrate the behavior of Eq. (S35b).

in uniformly-spaced steps when U is increased in uniform steps. This implies that $\widetilde{B}_*$ is exponentially suppressed with increasing U (which also shifts the minimum in $\widetilde{B}_*$ towards more positive $|\widetilde{V}_c|$-values). The function $F(U)$ that characterizes the exponential suppression can be obtained from the offsets of linear fits to $\ln(\widetilde{B}_*)$ vs. $\pi|\widetilde{V}_c|/\Omega_x$, repeated for various U-value. The resulting function $F(U)$, shown in Fig. S13**b** for several values of the curvature Ω_x, exhibits the behavior described by Eq. (S35b) quite well: it increases linear with U, on a scale set by $\sqrt{\tau\Omega_x}$. This reflects the fact that in static fRG, the dimensionless quantity that governs the effective interaction strength is $U\mathcal{A}_j(0)$ (cf. Sec. S-6), and at the barrier top we have [cf. Eq. (S19c) and Fig. S11]

$$U\mathcal{A}_{j=0}(0) \propto U/\sqrt{\tau\Omega_x}\,. \tag{S36}$$

Paraphrasing Eq. (S35a), we can formulate the following conclusions for how the $\widetilde{V}_c$-dependence of $\widetilde{B}_*$ in the regime $g \simeq 1$ is affected by turning on U: (i) The factor $e^{\pi|\widetilde{V}_c|/\Omega_x}$ from Eq. (S32) persists, essentially without a change in the numerical prefactor π/Ω_x of $|\widetilde{V}_c|$ in the exponent. (ii) The pre-exponential factor decreases exponentially with U, in a fashion that corresponds to shifting $\widetilde{V}_c \to \widetilde{V}_c + \Omega_x F(U)/\pi$. The physical interpretation is that local interactions increase the Hartree potential and hence the effective barrier height [causing (ii)], but do not significantly change its effective curvature [resulting in (i)]. Of course, the latter statements are true only approximately, in that Fig. S13 does exhibit slight deviations between the actual data and the behavior stated by Eqs. (S35).

Together, points (i) and (ii) suggest that for a QPC, the qualitative effect of interactions on $\widetilde{B}_*$ can already be found by *perturbatively* calculating the Hartree potential. We have done so, obtaining results (not shown here) in qualitative agreement with those just discussed. A simpler treatment of the same effects might be possible using semiclassical WKB wave functions, as done in Ref. 6 in a calculation of the Fock contribution to $\widetilde{T}_*$, but this is left as a topic for future study. (We remark that when the calculation of $\widetilde{T}_*$ in Ref. 6, extractable from their Eq. (33), is specialized to a point-like interaction with range zero, the result yields precisely the same $e^{\pi|\widetilde{V}_c|/\Omega_x}$ dependence for $\widetilde{T}_*$ as found by us in Eq. (S32) above.)

Note from Eq. (S35) that decreasing the curvature Ω_x at the top of the QPC barrier or increasing the interaction strength U (e. g. using a top gate) have qualitatively similar effects, in that both tend to decrease $\widetilde{B}_*$ and hence to strengthen the low-$\widetilde{B}$ response of the conductance. Likewise, decreasing Ω_x or increasing U also cause similar changes in the conductance step at $\widetilde{B} = \widetilde{T} = 0$, in that both tend to make the 0.7-shoulder more prominent. This is illustrated in Fig. S14, whose panels **b** and **c** offer a succinct summary of how the 0.7-anomaly depends on geometry and interactions, respectively.

Since Ω_x sets both the width of the conductance step [Eq. (S31)] and the slope of $\ln(\widetilde{B}_*)$ vs. $|\widetilde{V}_c|$ [Eq. (S35a)], an experimental consistency check is possible: We have determined the said step width and slope from Fig. A2**e** and extracted Ω_x-values from each, finding $\Omega_x^{\text{step}} \simeq a \times 0.026$ V from the step width and $\Omega_x^{\text{slope}} \simeq a \times 0.048$ V from the slope ($a \simeq 37$ meV/V is a geometric conversion factor between applied gate voltage (in V) and the resulting electrostatic potential energy (in meV), such that $\widetilde{V}_c = -a\,V_c$). The fact that Ω_x^{step} and Ω_x^{slope} agree within a factor of two is quite satisfactory, given the fact that we made no attempt to realistically model the shape of the QPC potential. Possible reasons for why the agreement is not perfect are that the experimental QPC potential was not perfectly parabolic, and that our use of a purely on-site (instead of longer-range) interaction is an oversimplification. (See also Sec. S-5 C below.)

To conclude this subsection, let us emphasize once more its most important qualitative conclusion: *inter-*

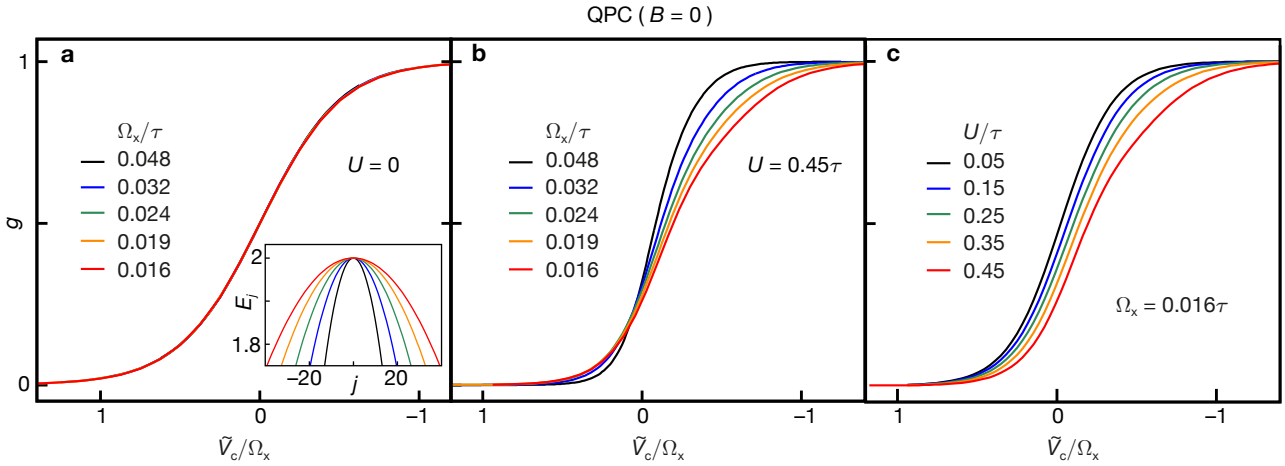

Figure S14: Effect of barrier curvature Ω_x (panels **a**,**b**) and interaction strength U (panel **c**) on the conductance through a QPC (model I), calculated by static fRG. The inset to **a** shows the top of a parabolic QPC barrier for several values of the curvature Ω_x. **a**, In the absence of interactions ($U = 0$) the conductance curves $g(\widetilde{V}_c)$, calculated for different Ω_x, all collapse onto a single curve when plotted as function of $\widetilde{V}_c/\Omega_x$, as expected from Eq. (S30). **b**, Similar plot as **a**, but for $U \neq 0$, which prevents a scaling collapse. **c**, Conductance curves $g(\widetilde{V}_c)$ calculated for fixed Ω_x but several different values of U, and scaled as in **a** and **b**. As explained in the main article, the combination of enhanced spectral weight at the Fermi energy $\mathcal{A}_{j=0}(0)$ and interaction U lowers the conductance in the vicinity of $\widetilde{V}_c \simeq 0$, resulting in an asymmetric and broadened conductance step. The strength of this effect is governed by the product $U\mathcal{A}_{j=0}(0) \propto U/\sqrt{\tau\Omega_x}$ [cf. Eq. (S36)]. This increases with decreasing Ω_x at fixed U (panel **b**) or likewise with increasing U at fixed Ω_x (panel **c**), causing an enhancement of the 0.7-shoulder in both cases.

actions cause an exponential reduction in $\widetilde{B}_*$, which can thus be significantly smaller than the QPC's natural energy scale Ω_x. (In Fig. A2**f**, the smallest values reported for $\mu_B B_*$ and $k_B T_*$ are 0.3 meV and 0.08 meV, respectively, significantly smaller than the above estimates of $\Omega_x^{\rm step} \simeq 1$ meV.) While the detailed form of the function $F(U)$ describing this suppression may be model-dependent, we believe the strong suppression of $\widetilde{B}_*$ with increasing U to be generic. This is a crucial ingredient for understanding the 0.7-anomaly, since it becomes more pronounced the smaller this crossover scale.

C. Geometry-dependence of interaction U

It would be interesting to experimentally study the interaction- and geometry dependence of B_* more systematically, by using the side- and top-gate voltages V_s and V_t to vary the effective barrier shape and interaction strength. Of course numerous studies of the 0.7-anomaly in varying geometries do exist[4,8–10,12,30,31], but to systematically check the predictions of Eq. (S35) for $\widetilde{B}_*(\widetilde{V}_c, \Omega_x, U)$, it would be necessary to simultaneously monitor the V_t- and V_s-dependence of $B_*(V_c)$, Ω_x *and* U. Indeed, whereas our model treats U as a fixed, given constant, in reality the effective interaction strength is geometry-dependent. We have already pointed out in Sec. S-2 A that it depends on the lateral confinement in the QPC region; more specifically, the effective interaction constant for a 1D model will depend on the spatial extent, say l_y, of the transverse wave-function, which, in turn, can depend quite delicately on the amount of screening, etc.

If no realistic modelling of the latter is available (we have not attempted any), the evolution of interaction strength with geometry is best gauged by tracking the evolution of experimentally accessible quantities such as g_{ss} and Δ_{hfo}. To be specific, the conductance $g(V_c, B, T)$ could be measured for various settings of V_t and V_s. A measure for the resulting changes in the effective interaction strength U could be obtained from the transconductance dG/dV_c at low T by monitoring the corresponding changes in g_{ss} or Δ_{hfo} (as in Fig. S5**b**, **c**). Simultaneously, estimates for Ω_x and l_y could be extracted, respectively, from the widths of the first step and first plateau of the conductance curve at low T; and B_* and T_* from the low-energy B- and T-dependence of the conductance (as in Figs. A2**e**, **f**). This would yield enough information to check Eq. (S35) in detail. We leave such a study for future work.

S-6. FUNCTIONAL RENORMALIZATION GROUP

In this section and the next, we describe the details of the two theoretical approaches used here: The present section is devoted to the functional renormalization group (fRG) which we used to study the $\widetilde{B}$-dependent quantities at $\widetilde{T} = \widetilde{V}_{sd} = 0$. Section S-7 outlines the second-order perturbation theory (SOPT) ap-

proach which we used to explore the properties of our model for fixed U at $\widetilde{T} \neq 0$ or $\widetilde{V}_{\rm sd} \neq 0$.

Both fRG and SOPT are set up as perturbation expansions with respect to a noninteracting ground state that has zero magnetization in the absence of a magnetic field, hence both yield perturbed ground states that also have this property. The possibility of spontaneous breaking of spin symmetry is thus ruled out *a priori* within both approaches. In choosing to set them up in this way, we therefore make the physical assumption that spontaneous symmetry breaking need not be invoked to explain the 0.7-anomaly. This assumption is justified *a posteriori* by the agreement between our fRG results and our experiments for the magnetic-field dependence of the 0.7-anomaly (as discussed in detail in Sec. S-2 C).

The present section summarizes the central ingredients of the fRG approach in the one-particle irreducible version[32] used here. The details of our approach, using the Matsubara formalism, are very similar to those of Refs. 33,34,40 and 41; technical aspects going beyond the latter works will be presented in detail elsewhere[36]. The main purpose here is to explicitly formulate the approximations that we have employed for the translationally nonuniform system with on-site interactions defined by Eq. (A1) of the main text [or Eq. (S11)]. (For completeness, we remark that the fRG approach described below is also capable of dealing with the Kondo effect in a 1D-model of a quantum dot, described by a double-barrier potential. Corresponding results will be presented elsewhere, in a comparative study of the Kondo effect and the 0.7-anomaly.[1])

A. Observables

Our goal is to calculate the conductance g through the CCR and the average number $n_{j\sigma}$ of spin-σ electrons at site j, at zero temperature. Following Ref. 33,34, we proceed in three steps. (i) We integrate out the two semi-infinite, noninteracting leads to the left and right of the CCR, using a standard projection technique; this results in a bare Matsubara Green's function for the CCR, $(\mathcal{G}_0)^\sigma_{ji}(i\omega)$, with a matrix structure in real space, $j, i \in [-N', N']$ being site indices. (ii) We incorporate interactions in the CCR by using fRG to calculate the full Matsubara Green's function of the CCR, $\mathcal{G}^\sigma_{ji}(i\omega)$; this step will be described in more detail in the next subsection. (iii) We calculate g and $n_{j\sigma}$ at $T = 0$ using

$$g = \frac{1}{2}\sum_\sigma \mathcal{T}_\sigma(0)\,, \tag{S37}$$

$$\mathcal{T}_\sigma(\omega) = \left|2\pi\tau^2\rho_0^\sigma(\omega)\mathcal{G}^\sigma_{-N',N'}(\omega+i0^+)\right|^2\,, \tag{S38}$$

$$n_{j\sigma} = \langle\hat{n}_{j\sigma}\rangle_T = \int_{-\infty}^{\infty} d\omega\, f(\omega)\mathcal{A}_{j\sigma}(\omega) = T\sum_n \mathcal{G}(i\omega_n) + \frac{1}{2}\,, \tag{S39}$$

$$\mathcal{A}_{j\sigma}(\omega) = -\frac{1}{\pi}\,{\rm Im}\mathcal{G}^\sigma_{jj}(\omega+i0^+)\,. \tag{S40}$$

Here $\mathcal{T}_\sigma(\omega)$ is the spin-dependent transmission probability for a spin-σ electron incident with energy ω relative to the chemical potential μ, and $\rho_0^\sigma(\omega)$ is the local density of states at the first site of a semi-infinite noninteracting tight-binding chain, representing a lead. For our fRG calculations we have chosen $\mu = 0$, implying half-filled leads.

B. fRG strategy and approximations

fRG may be viewed as RG-enhanced perturbation theory in the interaction. It is based on solving a hierarchy of coupled ordinary differential equations, the *flow equations*, for the system's n-particle vertex functions, γ_n^Λ. The flow parameter Λ controls the RG flow from an initial cutoff Λ_i, at which all vertex functions are known and simple, to a final cutoff Λ_f, at which the full theory is recovered. Solving the full hierarchy of flow equations, however, is impossible in practice and simplifying approximations are needed to render them tractable. When setting up our flow equations, we make two technical approximations, which are both exact to second order in the interaction U. We briefly summarize them here, and provide more details in the subsequent technical discussions.

(i) We truncate the fRG hierarchy by setting $\gamma^\Lambda_{n\geq 3} = 0$. This standard approximation[32] offers a systematic way of summing up parquet-type diagrams (i. e. diagrams that result from coupled RPA-equations)[32] for the two-particle vertex. However, due to the neglect of higher order terms, it fails if the interaction becomes too large (on a scale set by the local density of states at the chemical potential).

(ii) We apply the coupled-ladder approximation[40,41] to treat the frequency dependence of the vertex, and extend this scheme to also treat the real space structure of the vertex. The coupled-ladder approximation sets to zero all components of the vertex except those that are generated already to second order in the bare (onsite) interaction, but retains the latter components throughout the flow.

C. fRG Flow equations

We introduce Λ as an infrared cut-off in the bare Matsubara propagator,

$$\mathcal{G}_0^\Lambda(i\omega) = \Theta_T(|\omega|-\Lambda)\mathcal{G}_0(i\omega)\,,\ \Lambda_i = \infty,\ \Lambda_f = 0\,, \tag{S41}$$

where Θ_T is a step function that is broadened on the scale of the temperature T (we discuss the limit $T = 0$ in Sec. S-6 E below). The fRG approach in the one-particle irreducible version then leads to the following set of equations. (For a derivation, see e. g. Refs. 32,37; very detailed discussions are given e. g. in Refs. 33,38, for

a diagrammatic derivation see Ref. 39.) The flow of the self-energy $\Sigma^\Lambda = -\gamma_1^\Lambda$ is given by

$$\frac{d}{d\Lambda}\gamma_1^\Lambda(q_1', q_1) = T\sum_{q_2', q_2} \mathcal{S}^\Lambda_{q_2,q_2'}\gamma_2^\Lambda(q_2', q_1'; q_2, q_1)\ , \tag{S42a}$$

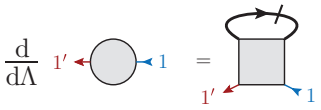

. (S42b)

Here $\mathcal{S}^\Lambda$ is defined in terms of the scale-dependent full propagator $\mathcal{G}^\Lambda$,

$$\mathcal{S}^\Lambda = \mathcal{G}^\Lambda\partial_\Lambda\left[\mathcal{G}_0^\Lambda\right]^{-1}\mathcal{G}^\Lambda = \quad , \tag{S43a}$$

$$\mathcal{G}^\Lambda = \left[\left[\mathcal{G}_0^\Lambda\right]^{-1} - \Sigma^\Lambda\right]^{-1} = \quad , \tag{S43b}$$

and γ_2^Λ is the two-particle irreducible vertex.

The flow of the latter can be arranged into three contributions (or parquet channels),

$$\frac{d}{d\Lambda}\gamma_2^\Lambda = \frac{d}{d\Lambda}(\gamma_p^\Lambda + \gamma_x^\Lambda + \gamma_d^\Lambda)\ , \tag{S44}$$

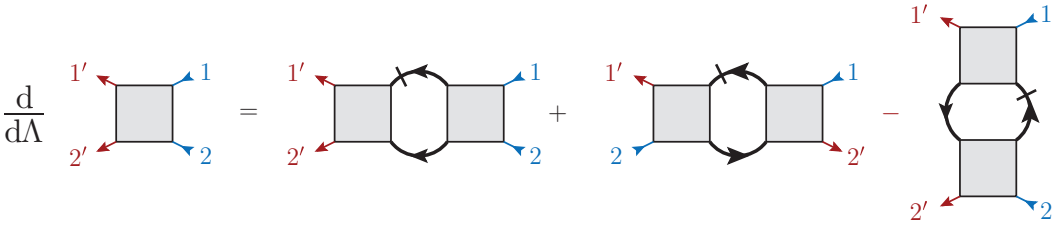

(S45)

called the particle-particle channel (P), and the exchange (X) and direct (D) contributions to the particle-hole channel, respectively, with the following explicit forms:

$$\frac{d}{d\Lambda}\gamma_p^\Lambda(q_1', q_2'; q_1, q_2) = T\sum_{q_3', q_3, q_4', q_4} \gamma_2^\Lambda(q_1', q_2'; q_3, q_4)\mathcal{S}^\Lambda_{q_3,q_3'}\mathcal{G}^\Lambda_{q_4,q_4'}\gamma_2^\Lambda(q_3', q_4'; q_1, q_2), \tag{S46a}$$

$$\frac{d}{d\Lambda}\gamma_x^\Lambda(q_1', q_2'; q_1, q_2) = T\sum_{q_3', q_3, q_4', q_4} \gamma_2^\Lambda(q_1', q_4'; q_3, q_2)\left[\mathcal{S}^\Lambda_{q_3,q_3'}\mathcal{G}^\Lambda_{q_4,q_4'} + \mathcal{G}^\Lambda_{q_3,q_3'}\mathcal{S}^\Lambda_{q_4,q_4'}\right]\gamma_2^\Lambda(q_3', q_2'; q_1, q_4)\ , \tag{S46b}$$

$$\frac{d}{d\Lambda}\gamma_d^\Lambda(q_1', q_2'; q_1, q_2) = -T\sum_{q_3', q_3, q_4', q_4} \gamma_2^\Lambda(q_1', q_3'; q_1, q_4)\left[\mathcal{S}^\Lambda_{q_4,q_4'}\mathcal{G}^\Lambda_{q_3,q_3'} + \mathcal{G}^\Lambda_{q_4,q_4'}\mathcal{S}^\Lambda_{q_3,q_3'}\right]\gamma_2^\Lambda(q_4', q_2'; q_3, q_2)\ . \tag{S46c}$$

All higher order vertices $\gamma_{n\geq 3}$ have been set to zero. For the purpose of treating the inhomogeneous chain model of Eq. (S11), the quantum numbers q_i denote a composite index of site, spin and Matsubara-frequency, $q_1 = (j_1, \sigma_1, i\omega_n^1)$, etc.

D. fRG for non-uniform systems

A standard strategy for getting an initial impression of the system's behavior is to neglect the flow of the two-particle vertex completely. For the present model, the results so obtained[36] turn out to be similar to those obtained from SOPT – they capture the effects of interactions quite well qualitatively, but not quantitatively. To allow quantitative comparisons to experiment, we have therefore included the flow of the two-particle vertex for all fRG results shown in this work. We now describe how this was done.

Since the bare propagators are not site-diagonal, the number of independent variables needed to describe the vertex $\gamma_2^\Lambda(q_1', q_2'; q_1, q_2)$ generated by Eq. (S46) is very large, $\mathcal{O}(N^4 N_\mathrm{f}^3)$ (N_f is the number of Matsubara-frequencies used in the numerics). To deal with this complication we use the coupled-ladder approximation[40,41] for the frequency dependence of γ_2^Λ and treat its site-dependence in a similar manner. Given the structure of the flow equation (S46) for γ_2^Λ, it is natural to divide the flowing vertex into four parts[41]:

$$\gamma_2^\Lambda = v + \gamma_p^\Lambda + \gamma_x^\Lambda + \gamma_d^\Lambda\ , \qquad \gamma_p^{\Lambda_i} = \gamma_x^{\Lambda_i} = \gamma_d^{\Lambda_i} = 0\ . \tag{S47}$$

Here v is the bare vertex, and γ_2^p, γ_2^x and γ_2^d, whose flows by definition are given by Eqs. (S46a), (S46b) and (S46c), sum up the P-, X- and D-channels, respectively (see Sec.

S-6 C).

Now, since the bare vertex is site-diagonal, only $\mathcal{O}(N^2 N_\mathrm{f})$ of the $\mathcal{O}(N^4 N_\mathrm{f}^3)$ different components in each channel are generated already to order v^2 [i. e. if, at the beginning of the flow, γ_2^Λ is replaced by v on the r. h. s. of Eq. (S46)]. We exploit this fact by making the following simplifying approximation in the spatial structure of γ_2: in each channel *we set to zero all components except those that are generated already to order v^2, but retain the latter components throughout the flow.* The dropped components are all of order v^3 or higher, which justifies their neglect as long as U_j is not too large. Furthermore *we only keep the intrinsic frequency dependence of each channel* (i. e. the frequency-dependence generated to 2nd order). Each channel thus depends only on a single bosonic frequency, denoted by Π, X and Δ for the P-, X- and D-channels, respectively. The feed-back into the other channels is performed using only the static part of each channel, i. e. its value evaluated at zero frequency[41]. By exploiting various symmetry relations, the retained components of γ_2^Λ can be parametrized in terms of four frequency-dependent matrices, $P_{ij}^\Lambda(\Pi)$, $X_{ij}^\Lambda(\mathrm{X})$, $D_{ij}^{\uparrow\Lambda}(\Delta)$ and $D_{ij}^{\downarrow\Lambda}(\Delta)$, defined as follows (and shown together with the diagrams that generate them to lowest order):

$$P_{ji}^\Lambda(\Pi) := \gamma_p^\Lambda\left(j\sigma\,\Pi-\omega_n', j\bar{\sigma}\,\omega_n'; i\sigma\,\Pi-\omega_n, i\bar{\sigma}\,\omega_n\right) = -\gamma_p^\Lambda\left(j\sigma\,\Pi-\omega_n', j\bar{\sigma}\,\omega_n'; i\bar{\sigma}\,\Pi-\omega_n, i\sigma\,\omega_n\right), \tag{S48a}$$

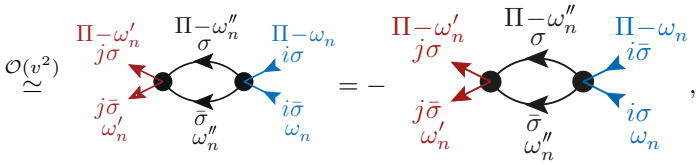

$$X_{ji}^\Lambda(\mathrm{X}) := \gamma_x^\Lambda\left(j\sigma\,\mathrm{X}+\omega_n', i\bar{\sigma}\,\omega_n; i\sigma\,\mathrm{X}+\omega_n, j\bar{\sigma}\,\omega_n'\right) = -\gamma_d^\Lambda\left(j\sigma\,\mathrm{X}+\omega_n', i\bar{\sigma}\,\omega_n; j\bar{\sigma}\,\omega_n', i\sigma\,\mathrm{X}+\omega_n\right), \tag{S48b}$$

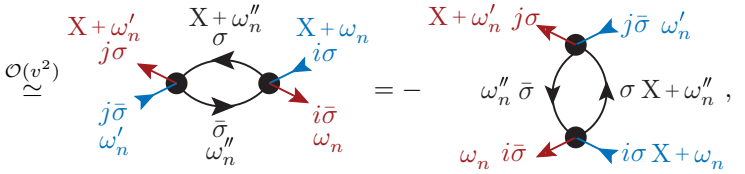

$$D_{ji}^{\sigma\Lambda}(\Delta) := \gamma_d^\Lambda\left(j\sigma\,\Delta+\omega_n', i\sigma\,\omega_n; j\sigma\,\omega_n', i\sigma\,\Delta+\omega_n\right) = -\gamma_x^\Lambda\left(j\sigma\,\Delta+\omega_n', i\sigma\,\omega_n; i\sigma\,\Delta+\omega_n, j\sigma\omega_n'\right), \tag{S48c}$$

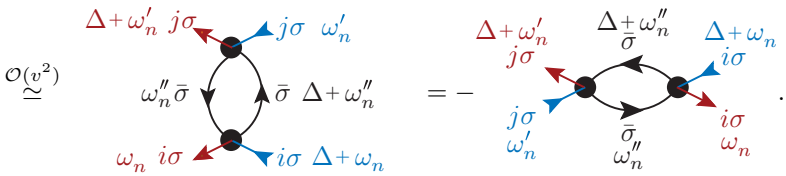

Note that these diagrams do not depend on ω_n and ω_n'; this is the reason why the coupled-ladder approximation allows each channel to be parametrized by just a single frequency. A detailed analysis of the flow of P_{ij}^Λ, X_{ij}^Λ and $D_{ij}^{\sigma\Lambda}$, to be published elsewhere[36], shows that the exchange channel X_{ij}^Λ, which grows significantly during the flow, is the dominant one. This lends *a posteriori* support to an assertion made in numerous works[4,7–9,12,14,20–22,30,31,42], namely that exchange interactions in the low-density inner region of the QPC play a dominant role for the 0.7-anomaly.

The parameter controlling the convergence of the fRG equations is $U \cdot \max_{\widetilde{V}_c,j}[\mathcal{A}_j(0)]$; if it is too large, these equations do not converge. For a QPC, the maximum value of the bare LDOS $\mathcal{A}_j^0(0)$ scales as $1/\sqrt{\tau\Omega_x}$ (see Sec. S-4 C).

E. Zero-temperature limit

The fRG flow equations discussed above apply to an arbitrary temperature T. However, the conductance at $T \neq 0$ depends on the retarded correlator $\mathcal{G}^R(\omega) = \mathcal{G}(i\omega_n \to \omega + i0^+)$ as well as the retarded parts of the vertex channels (e.g. $P(i\Pi_n \to \Pi + i0^+)$), which have to be obtained by analytic continuation from the imag-

inary to the real frequency axis. In numerical practice, this analytical continuation turned out to be unfeasible for the present problem. Therefore, we have here studied only the $T = 0$ limit, in which the Matsubara frequencies form a continuum and the conductance [Eq. (S37)] is expressed in terms of the zero-energy transmission $\mathcal{T}_\sigma(0)$. For numerical computations, we represented the continuum of Matsubara frequencies by a discrete set, and used its smallest positive member to evaluate the Matsubara Green's function $\mathcal{G}^\sigma_{-N',N'}(i0^+)$ needed for $\mathcal{T}_\sigma(0)$ [Eq. (S38)].

In the limit $T \to 0$, the cut-off function Θ_T in Eq. (S41) becomes a sharp step function, with $\Theta_0(0) = \frac{1}{2}$ and $\partial_\omega \Theta_0(\omega) = \delta(\omega)$. Since a combination of δ- and Θ-functions occurs in the fRG flow equations, the limit $T \to 0$ has to be taken with care, with the result[40]:

$$\mathcal{S}^\Lambda(i\omega) \overset{T=0}{=} \delta(|\omega| - \Lambda)\widetilde{\mathcal{G}}^\Lambda(i\omega), \tag{S49a}$$

$$\widetilde{\mathcal{G}}^\Lambda(i\omega) = \Big[[\mathcal{G}_0(i\omega)]^{-1} - \Sigma^\Lambda(i\omega) \Big]^{-1}, \tag{S49b}$$

$$\mathcal{S}^\Lambda_{i,j}(i\omega)\mathcal{G}^\Lambda_{k,l}(i\omega') \overset{T=0}{=} \delta(|\omega| - \Lambda)\widetilde{\mathcal{G}}^\Lambda_{i,j}(i\omega) \times \Theta(|\omega'| - \Lambda)\widetilde{\mathcal{G}}^\Lambda_{k,l}(i\omega'). \tag{S49c}$$

F. Static fRG

Most of our exploratory work on the zero-temperature properties of the 0.7-anomaly was done using "static" fRG (here denoted by fRG^0). It entails a further approximation relative to the "dynamic" fRG approach described above (here denoted by fRG$^\omega$), in that fRG^0 neglects the frequency dependence of the self-energy and all vertices. This is done by setting all three bosonic frequencies Π, X and Δ to zero. As a result the self-energy is frequency-independent, too. fRG^0 leads to reliable results only for the zero-frequency Green's function at zero temperature. If knowing the latter suffices (such as when studying the magnetic field-dependence at $\widetilde{T} = 0$), fRG^0 is a very flexible and efficient tool, computationally cheaper than our full coupled-ladder scheme fRG$^\omega$ by a factor of 10^3. Moreover, for the model studied here its results turn out to be qualitatively very similar to those of fRG$^\omega$. This is illustrated in Fig. S15, from which we note the following salient features.

The main difference in the conductance curves calculated by the two methods is an overall interaction-induced, U-dependent shift of the position of the fRG^0 conductance step w. r. t. to that of fRG$^\omega$, towards somewhat smaller values of $\widetilde{V}_c$ (compare Figs. S15**a**,**b**); however the *shapes* of the corresponding curves (modulo the shift) are essentially identical (Fig. S15**c**). The shift itself merely amounts to a small change in overall chemical potential and can be regarded as an insignificant detail, in particular in the context of the 0.7-anomaly, where both in theoretical and experimental studies, the focus is on the shape of the step, not its position.

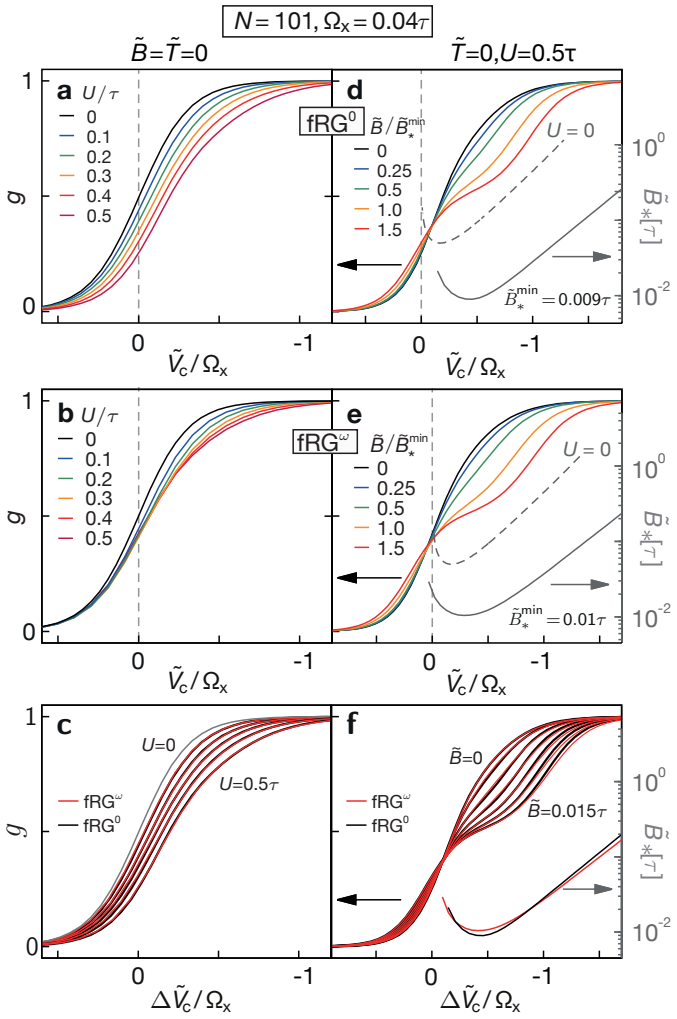

Figure S15: Comparison of results from static fRG (fRG^0, top panels) and dynamic fRG (fRG$^\omega$, middle panels, reproduced from Figs. A1**k** and A2**a**, respectively). The bottom panels show that after compensating for a U-dependent shift (here applied to the fRG$^\omega$ curves to get best overlap with the fRG^0 curves) both sets of curves have almost identical shapes. Left panels: The interaction dependence of the conductance $g(\widetilde{V}_c)$ at $\widetilde{B} = \widetilde{T} = 0$. Right panels: The magnetic-field dependence of the $\widetilde{T} = 0$ conductance $g(\widetilde{V}_c)$ at fixed $U = 0.5\tau$.

Closer inspection reveals that the magnetic field dependence (at fixed U) of the fRG^0 conductance curves is slightly stronger for small fields and slightly weaker for large fields, compared to that of fRG$^\omega$ (see Figs. S15**d**-**f**). This implies small quantitative differences in the low-energy scale $\widetilde{B}_*$ and the effective g-factor g_{ss}.

All in all, for the purposes of exploring the field-dependence of the 0.7-anomaly at fixed U, the differences in results between fRG$^\omega$ and fRG^0 are evidently very small. Hence we have opted to use the computationally much cheaper fRG^0 for the results presented in Secs. S-3 and S-5.

S-7. SECOND-ORDER PERTURBATION THEORY

The main limitation of our calculations using static fRG is their restriction to $\omega = 0$ and hence to zero temperature and zero source-drain voltage. As a first step toward exploring the properties of our model at $\widetilde{T} \neq 0$ and $\widetilde{V}_{\rm sd} \neq 0$, we have calculated the conductance of a QPC using second-order perturbation theory (SOPT), applied to model II (see Supplementary Sec. S-4 D). Sec. S-7 A presents the diagrams used for this purpose, and Sec. S-7 B discusses how we treat non-equilibrium transport using Keldysh-SOPT. Sec. S-7 C elaborates the main article's discussion of the SOPT results for the $\widetilde{B}$-, $\widetilde{T}$- and $\widetilde{V}_{\rm sd}$-dependence of the conductance, which are in fairly good qualitative agreement with experiment. Sec. S-7 D concludes with some comments regarding an SOPT artefact that arises with increasing U.

A. Equilibrium SOPT

We follow the strategy of Oguri[43], who has carried out a similar calculation for a particle-hole symmetric version of our model (with $N \leq 4$) at zero field. It is straightforward to generalize his equations to the case of present interest, with broken particle-hole symmetry and nonzero field. The conductance is calculated from

$$g \;=\; \frac{1}{2}\sum_{\sigma}\int_{-\infty}^{\infty} d\omega \left[-\frac{\partial f(\omega)}{\partial \omega}\right] \mathcal{T}_{\sigma}(\omega)\;. \qquad \text{(S50)}$$

where $\mathcal{T}_{\sigma}(\omega)$ is calculated using Oguri's[43] equations (2.36-38) and (4.10). They can be graphically depicted as

$\mathcal{T}_\sigma(\omega)$ = 4 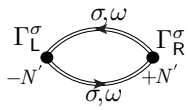 + 2 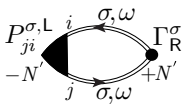

(S51)

$P^{\sigma,\mathsf{R/L}}_{ji}(\omega)$ = 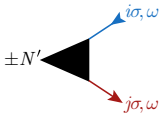

= 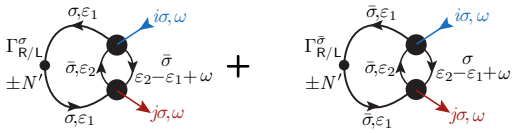

+ 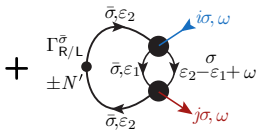

(S52)

where large black dots depict the bare interaction vertex, small black dots the coupling $\Gamma^{\sigma}_{R/L}(\epsilon)$ to the reservoirs, and the double lines represent the retarded interacting Green's function $\mathcal{G}^R = [(\mathcal{G}^{0R})^{-1} - \Sigma^R]^{-1}$. Its self-energy Σ^R is calculated to second order using the following diagrams:

$\Sigma^{\sigma}_{ji}(\omega)$ = δ_{ij} 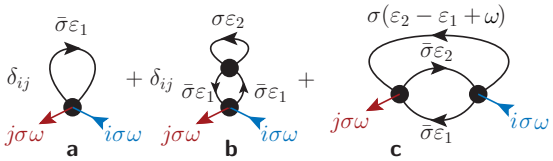

(S53)

Diagram **c** corresponds to Oguri's[43] Fig. 6, which represent the Fock contribution. Our treatment differs from Oguri's only regarding the Hartree diagrams **a** and **b**. Whereas he incorporates their effects in an implicit manner by exploiting particle-hole symmetry, this symmetry is not present in our problem, hence we include the Hartree diagrams explicitly in the self-energy.

The diagrams in Eqs. (S52) and (S53) involve Matsubara frequencies; they have to be analytically continued to real frequencies before being used in Eq. (S51) for $\mathcal{T}_\sigma(\omega)$, as discussed in detail by Oguri. The resulting formulas, obtained by generalizing Oguri's[43] equations [his (4.2), (4.3) for the Fock diagram, and (4.10) for the current vertex] to the spin-dependent case of non-zero field, will be presented elsewhere[36].

In the main article, the transmission probability is written as

$$\mathcal{T}_\sigma(\omega) = \mathcal{T}^{\rm el}_\sigma(\omega) + \mathcal{T}^{\rm in}_\sigma(\omega), \qquad \text{(S54)}$$

where $\mathcal{T}^{\rm el}_\sigma(\omega)$ and $\mathcal{T}^{\rm in}_\sigma(\omega)$, given by the first and second terms of Eq. (S51), describe the elastic and inelastic contributions to the transmission probability, respectively. They are related by a generalized Ward identity that is respected within the approximation scheme described above (Eq. (3.120) in Ref. 43):

$$-\,\mathrm{Im}\Sigma^{\sigma,R}_{ji}(\omega) = \sum_{\alpha=L/R} P^{\sigma,\alpha}_{ji}(\omega)\;. \qquad \text{(S55)}$$

This relation links the current vertex to the inelastic decay rate, governed by the imaginary part of the self-energy. An increase in the contribution of the current vertex, therefore, goes hand in hand with an increase in inelastic scattering.

SOPT calculations turn out to be computationally significantly more costly than fRG calculations. Therefore, all our SOPT calculations were done using model II, which has some computational advantages over model I, as explained in Supplementary Sec. S-4 D.

B. Nonequilibrium SOPT

In order to calculate the differential conductance

$$g_{\rm nl} = \frac{dI}{d\widetilde{V}_{\rm sd}} \qquad \text{(S56)}$$

at finite bias voltage ($\widetilde{V}_{\rm sd} \neq 0$) we use the Meir-Wingren formula for the current through a region of interacting electrons[44]:

$$I = \frac{ie}{2h}\int d\varepsilon \Big(\mathrm{Tr}\{[f_L\Gamma^L - f_R\Gamma^R](\mathcal{G}^R - \mathcal{G}^A)\} + \mathrm{Tr}\{[\Gamma^L - \Gamma^R]\mathcal{G}^<\}\Big), \tag{S57}$$

with $\mathcal{G}^< = \frac{1}{2}\left(\mathcal{G}^K - \mathcal{G}^R + \mathcal{G}^A\right)$. The finite bias $\widetilde{V}_{\rm sd}$ enters via the occupation functions of the left and right lead:

$$f_{R/L}(\omega) = f(\omega \mp \widetilde{V}_{\rm sd}/2). \tag{S58}$$

The retarded, advanced and Keldysh Green's functions $\mathcal{G}^{R/A/K}$ are given by Dyson equations:

$$\mathcal{G}^{R/A} = \frac{1}{(G^{R/A})^{-1} - \Sigma^{R/A}}.$$
$$\mathcal{G}^K = \mathcal{G}^R[(G^R)^{-1}G^K(G^A)^{-1} + \Sigma^K]\mathcal{G}^A, \tag{S59}$$

The non-equilibrium retarded, advanced and Keldysh self-energies occurring herein, $\Sigma^{R/A/K}$, are calculated to second order in the interaction, using standard Keldysh techniques. The corresponding diagrams are again given by Eq. (S53), but now feature an additional Keldysh index.

C. $\widetilde{B}$-, $\widetilde{T}$- , and $\widetilde{V}_{\rm sd}$-dependence of $g(\widetilde{V}_{\rm c})$

In this section, we give a detailed discussion of the SOPT results presented in the main text for the $\widetilde{B}$-, $\widetilde{T}$- and $\widetilde{V}_{\rm sd}$-dependence of the conductance $g(\widetilde{V}_{\rm c})$. In particular, we analyse their similarities and differences w. r. t. our fRG results and experimental measurements.

Dependence on magnetic field at zero temperature: To gauge the reliability of SOPT, we begin by comparing its results for the magnetic field dependence of the conductance (Fig. A2**c**) to those obtained from fRG (Fig. A2**a**) and from experimental measurements (Fig. A2**e**). Though some details differ, the qualitative agreement is very good. It includes, in particular, the following two important features: (i) The conductance $g(\widetilde{V}_{\rm c})$ is strongly suppressed with increasing $\widetilde{B}$ for $\widetilde{V}_{\rm c} < 0$, leading to the evolution of a kink around 0.5 (thick red line in Fig. A2**c**). (ii) $\ln(\widetilde{B}_*)$ increases nearly linearly with decreasing $\widetilde{V}_{\rm c}$ in the regime where $g \to 1$ (thin grey line in Fig. A2**c**); in fact, even the slope of the linear increase is nearly the same as that found by fRG (grey line in Fig. A2**a**). This remarkable agreement between SOPT and fRG for the $\widetilde{V}_{\rm c}$-dependence of $\widetilde{B}_*$ implies that the latter is determined mainly by geometry (corroborating a similar conclusion from Sec. S-5), i. e. interactions, which are underestimated in SOPT, influence the $\widetilde{V}_{\rm c}$-dependence only weakly.

As an aside, we note that both of the above-mentioned features (i) and (ii) survive[45] (data not shown) even if

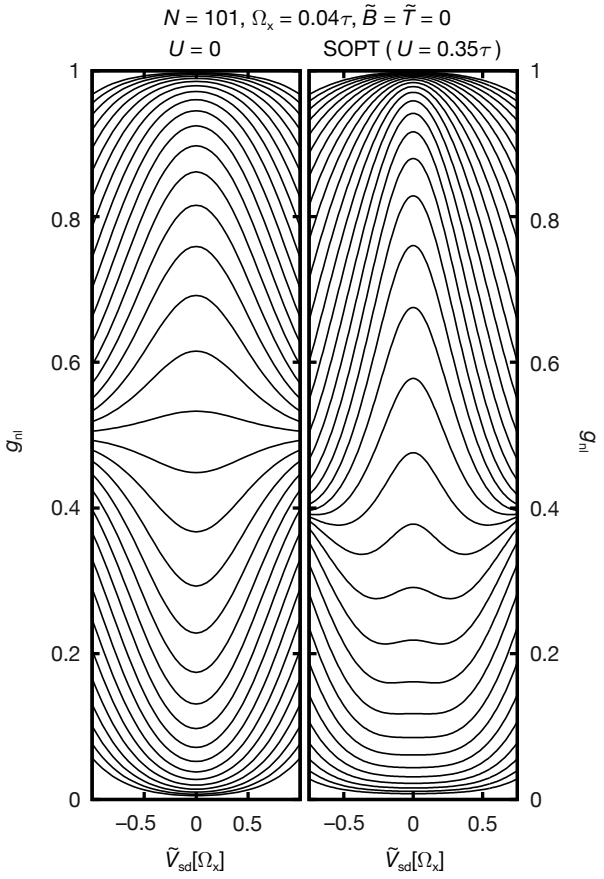

Figure S16: Differential conductance for model II at $\widetilde{B} = \widetilde{T} = 0$, plotted as a function of bias voltage for several $\widetilde{V}_{\rm c}$-values, calculated **a** without and **b** with interactions, the latter treated using second order perturbation theory (SOPT) (see Sec. S-7 B).

SOPT is simplified by neglecting the Fock contribution to the self-energy [diagram **c** of Eq. (S53)], retaining only the first- and second-order Hartree terms [diagrams **a** and **b** of Eq. (S53)]. Thus, the $\widetilde{B}$-dependence is dominated by Hartree terms (describing shifts in the barrier heights for spin-up vs. spin-down electrons), rather than Fock terms (describing inelastic scattering, which is relevant only at finite temperatures and finite bias voltage). This conclusion is consistent with the fact that the approach of Lunde *et al.*, Ref. 6, which properly incorporated the (model) system's geometry-dependence by using WKB wave functions, is nevertheless unable to reproduce the energy scale $\widetilde{B}_*$ from the magnetic field dependence as long as only Fock-like diagrams are considered[46].

Next, we mention an important instance in which SOPT fails to agree with experimental and fRG results for the conductance (compare Fig. A2**c** to Fig. A2**e** and Fig. A2**a**): SOPT does not yield the 0.7-shoulder in the conductance at $\widetilde{T} = \widetilde{B} = 0$. (A shoulder does develop for larger U ($\gtrsim 0.5\tau$), for which, however, SOPT can no longer be trusted.)

To summarize: SOPT correctly captures several important features of the field dependence of the conductance at zero temperature, but not all details. The same turns out to be true for the temperature dependence at zero field, as we discuss next:

Dependence on temperature at zero magnetic field: Fig. A2**d** presents SOPT results for the temperature-dependence of the conductance at zero field. Comparing these to the corresponding experimental results of Fig. A2**f**, we note that SOPT correctly reproduces the main effect of increasing temperature, namely to reduce the conductance. However, SOPT does not fully succeed in reproducing the detailed shape of the experimental pinch-off curves: the SOPT curves lack the tendency of the experimental curves to show a well-defined shoulder that is amplified by increasing temperature.

Dependence on bias voltage: Fig. S16**a** shows the bare ($U = 0$) differential conductance $g^0_{\rm nl}$ as a function of bias voltage $\widetilde{V}_{\rm sd}$ for several $\widetilde{V}_{\rm c}$-values ranging from the open channel ($g \simeq 1$) to the pinched-off regime ($g \simeq 0$). The bare conductance can easily be calculated from the Landauer-Büttiker formula (S25), using Büttiker's formula (S30) for the transmission. The resulting $g^0_{\rm nl}(\widetilde{V}_{\rm sd})$ exhibits a zero bias peak (ZBP) for linear conductance $g > 0.5$ ($\widetilde{V}_{\rm c} < 0$), and a zero bias minimum in the tunneling regime, where $\widetilde{V}_{\rm c} > 0$ and $g < 0.5$.

Turning on interaction (see Fig. A3**i**, as well as Fig. S16**b**) causes the following effects on $g_{\rm nl}$: First, a ZBP forms even when the linear conductance is $g < 0.5$, and second, the width of the ZBP is reduced across the whole $\widetilde{V}_{\rm c}$-range. These two interaction-induced characteristics can be understood in terms of two main mechanisms: (i) Applying finite bias generates a net charge flow into the barrier region (since there the LDOS is ω-asymmetric around $\omega = 0$), thereby enhancing the effective barrier height for electrons entering the CCR. For sufficiently large interaction this leads to a reduction of conductance (Hartree effect). (ii) Turning on $\widetilde{V}_{\rm sd}$ opens phase space for inelastic scattering. Consequently the combination of a large LDOS in the vicinity of the classical turning points (where $\omega_j^{\rm min} \simeq 0$), interactions, and $\widetilde{V}_{\rm sd} > 0$, leads to a high probability for backscattering, hence a reduction of conductance. We note that both mechanisms (i) and (ii) also apply when the temperature is increased; in this sense, the temperature- and bias-dependencies of the 0.7-anomaly are manifestations of the similar physical processes.

We take the SOPT results shown in Fig. A2**d** and Figs. A3**b**,**d**-**f** as encouraging indications that our model has the potential to properly describe properties of the 0.7-anomaly at finite temperature and bias. To summarize: the anomalous conductance decrease with increasing $\widetilde{T}$ or $\widetilde{V}_{\rm sd}$ in the sub-open regime originates from the enhancement, by the van Hove ridge apex near μ, of the $\widetilde{T}$- or $\widetilde{V}_{\rm sd}$-induced increase of (i) the net charge and (ii) the amount of inelastic scattering in the CCR.

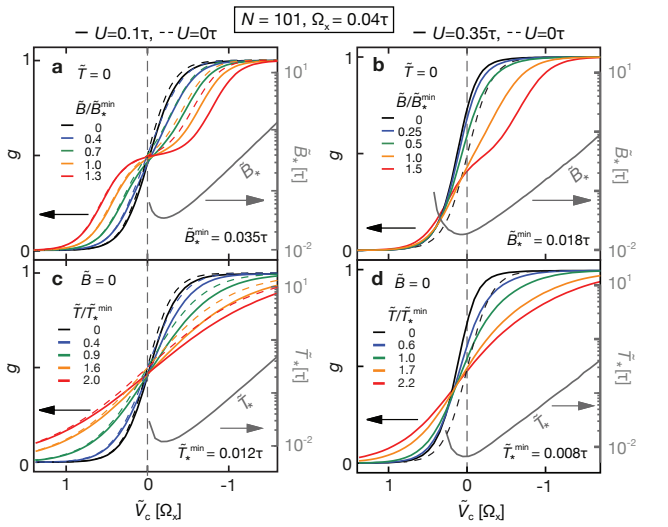

Figure S17: SOPT results (solid lines) for the conductance $g(\widetilde{V}_{\rm c})$ as function of $\widetilde{V}_{\rm c}$, illustrating the qualitative changes incurred when interactions are increased from being weak (left panels) to rather strong (right panels, reproduced from Figs. A2**c**, **d**). Panels (a,b) show the $\widetilde{B}$-dependence of the conductance at $\widetilde{T} = 0$, panels (c,d) show its $\widetilde{T}$-dependence at $\widetilde{B} = 0$. Dashed lines show corresponding curves for the bare $U = 0$ conductance, $g^0(\widetilde{V}_{\rm c})$.

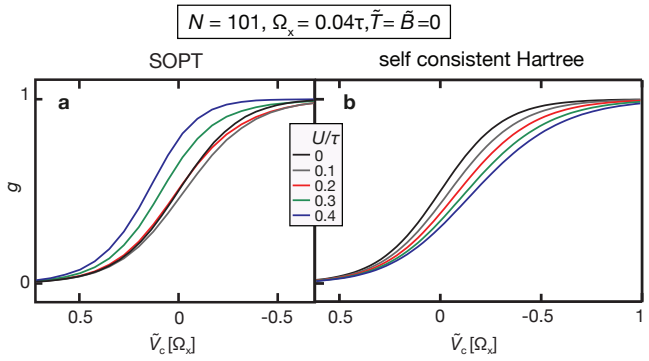

Figure S18: The zero-temperature linear conductance $g(\widetilde{V}_{\rm c})$ as function of $\widetilde{V}_{\rm c}$, for several values of U, calculated **a**, using pure SOPT, and **b**, using a self-consistent Hartree approach (without Fock contributions). The non-monotonic behavior of $g(\widetilde{V}_{\rm c})$ as function of increasing U seen in **a** is an SOPT artefact, caused by the neglect of terms beyond 2nd order; this artefact is avoided by the self-consistent Hartree approach, as seen in **b**.

D. SOPT artefact arising for increasing U

We conclude with some comments on the choice of interaction strength used for our SOPT calculations. Fig. S17 compares the SOPT results for the $\widetilde{B}$- and $\widetilde{T}$-dependence of $g(\widetilde{V}_{\rm c})$ calculated at $U = 0$ (left panels, dashed lines), $U = 0.1\tau$ (left panels, solid lines) and $U = 0.35\tau$ (right panels, solid lines). The left pan-

els show that upon turning on a weak interaction (solid lines), the conductance g at fixed values of $\widetilde{V}_c$, $\widetilde{B}$ and $\widetilde{T}$ is shifted slightly downward due to the increase of the Hartree barrier, leading to a slight skewing of the shape of the conductance step relative to the corresponding non-interacting value $g^0(\widetilde{V}_c)$ (dashed lines). However, significantly larger values of U are needed (right panels) to yield the strong type of skewing characteristic for measured conductance curves that exhibit the 0.7-anomaly.

Note that due to this large choice of U in the right panels, the SOPT conductance curve $g(\widetilde{V}_c)$ at $\widetilde{B} = \widetilde{T} = 0$ (solid black) has been shifted upwards to actually lie *above* its non-interacting value (dashed black). This non-monotonic behavior of $g(\widetilde{V}_c)$ for increasing U (the shift being initially downwards, then upwards, illustrated clearly in Fig. S18**a**) is an artefact of SOPT's neglect of terms beyond 2nd order: the signs (+ or −) of Hartree contributions are known to alternate with the order of expansion, hence truncating the latter beyond 2nd order generates non-monotonic behavior for the shift with increasing U once the 2nd-order term becomes larger than the 1st-order term. (fRG avoids this problem by summing up, in effect, a series of diagrams to all orders, resulting in a monotonic dependence of $g(\widetilde{V}_c)$ on U, see Fig. A1**k**.)

We emphasize that this SOPT artefact is problematic only if one is interested in following the evolution of physical properties with increasing U (examples of such evolution, calculated by fRG, are shown in Figs. A1**e**,**j**,**k**). However, for the purpose of studying physical properties *at fixed* U, SOPT does quite well: it succeeds in qualitatively illustrating the generic, experimentally observed trends of how interactions affect the $\widetilde{B}$-, $\widetilde{T}$-, and $\widetilde{V}_{sd}$-dependence of the conductance even if the (fixed) value of U is rather large, because the physical origin of these trends is robust. A detailed discussion of this point will be published elsewhere.

Finally, we note that the above-mentioned artefact can be avoided by adopting an approach similar in spirit to SOPT, but using a self-consistently-determined Hartree potential (thus treating Hartree and Fock terms on unequal footing): For $\widetilde{T} = \widetilde{V}_{sd} = 0$, calculate the self-energy from just the first-order Hartree diagram Eq. (S53)**a** to obtain a Hartree-shifted local potential $E_{j\sigma} + U_j n_{j\sigma}$, determine the local charge $n_{j\sigma}$ self-consistently, and calculate the QPC transmission using Hartree-dressed Green's functions (see Fig. S18**b**).

For nonzero $\widetilde{T}$ or $\widetilde{V}_{sd}$, use Hartree-dressed (instead of bare) Green's functions for all thin lines in the SOPT Eqs. (S51) to Eq. (S53), but include only the Fock diagram in the latter, to avoid double-counting Hartree contributions. The Ward identity [Eq. (S55)] relating the current vertex to the self-energy would remain intact in this approach. Pursuing it in detail is left as a topic for future study.

[1] Heyder, J., Bauer, F., E. Schubert, D. Borowsky, D. Taubert, D. Schuh, W. Wegscheider, J. von Delft & S. Ludwig. Comparative study of the Kondo effect and the 0.7-anomaly. *To be published.*

[2] D. Borowski. Transportmessungen zur Untersuchung der 0.7-Struktur in Quantenpunktkontakten. *Diploma Thesis*, Ludwig-Maximilians-Universität München (2011).

[3] Patel, N. K., Nicholls, J. T., Martín-Moreno, L., Pepper, M., Frost, J. E. F., Ritchie, D. A. & Jones, G. A. C. Evolution of half plateaus as a function of electric field in a ballistic quasi-one-dimensional constriction. *Phys. Rev. B*, **44**, 13549-13555 (1991).

[4] Reilly, D. J., Facer, G. R., Dzurak, A. S., Kane, B. E., & Clark, R. G. Many-body spin-related phenomena in ultra low-disorder quantum wires. *Phys. Rev. B* **63**, 121311(R) (2001).

[5] Büttiker, M. Quantized transmission of a saddle-point constriction. *Phys. Rev. B* **41**, 7906(R) (1990).

[6] Lunde, A. M., De Martino, A., Schulz, A., Egger, R., and Flensberg, K., Electron-electron interaction effects in quantum point contacts. *New J. Phys.* **11**, 023031 (2009).

[7] Thomas, K. J., Nicholls, J. T., Simmons, M. Y., Pepper, M., Mace, D. R. Possible Spin Polarization in a One-Dimensional Electron Gas. *Phys. Rev. Lett.* **77**, 135-138 (1996).

[8] Thomas, K. J., Nicholls, J. T., Appleyard, N. J., Simmons, M. Y., Pepper, M., Mace, D. R., Tribe, W. R., & Ritchie, D. A. Interaction effects in a one-dimensional constriction. *Phys. Rev. B* **58**, 4846-4852 (1998).

[9] Koop, E., Lerescu, A., Liu, J., van Wees, B., Reuter, D., Wieck A.D. & van der Wal, C. The Influence of Device Geometry on Many-Body Effects in Quantum Point Contacts: Signatures of the 0.7 Anomaly, Exchange and Kondo *J. Supercond. Nov. Magn.* **20**, 433-441 (2007).

[10] Burke A. M., Klochan O., Farrer I., Ritchie D. A., Hamilton A. R. & Micolich A. P. Extreme Sensitivity of the Spin-Splitting and 0.7 Anomaly to Confining Potential in One-Dimensional Nanoelectronic Devices. *Nano Letters*, Article ASAP, DOI: 10.1021/nl301566d (2012).

[11] Patel, N. K., Nicholls, J. T., Martn-Moreno, L., Pepper, M., Frost, J. E. F., Ritchie, D. A. & Jones, G. A. C. Properties of a ballistic quasi-one-dimensional constriction in a parallel high magnetic field. *Phys. Rev. B* **44**, 10973-10975 (1991).

[12] Reilly, D. J., Buehler, T. M., O'Brien, J. L., Hamilton, A. R., Dzurak, A. S., Clark, R. G., Kane, B. E., Pfeiffer, L. N. & West, K. W. Density-Dependent Spin Polarization in Ultra-Low-Disorder Quantum Wires. *Phys. Rev. Lett.* **89**, 246801 (2002).

[13] DiCarlo, L., Zhang, Y., McClure, D. T., Reilly, D. J., Marcus, C. M., Pfeiffer, L. N. & West, K. W. Shot-Noise Signatures of 0.7 Structure and Spin in a Quantum Point Contact. *Phys. Rev. Lett.*, **97**, 036810 (2006).

[14] Smith, L. W., Hamilton, A. R., Thomas, K. J., Pepper, M., Farrer, I., Griffths, J. P., Jones, G. A. C. &Ritchie, D. A. Compressibility measurements of quasi-one-dimensional

quantum wires Phys. Rev. Lett. **107**, 126801 (2011).
[15] Blanter, Ya. M. & Büttiker. Shot noise in mesoscopic conductors. *Physics Reports,* **336** 1-166, (2000).
[16] Lüscher, S., Moore, L. S., Rejec, T., Meir, Y., Shtrikman, H. & Goldhaber-Gordon, D. Charge Rearrangement and Screening in a Quantum Point Contact. *Phys. Rev. Lett.* **98**, 196805 (2007).
[17] Meir, Y., Hirose, K. & Wingreen, N. S. Kondo Model for the 0.7 Anomaly in Transport through a Quantum Point Contact. *Phys. Rev. Lett.* **89**, 196802 (2002).
[18] Golub, A., Aono, T. & Meir, Y. Suppression of Shot Noise in Quantum Point Contacts in the "0.7 Regime". *Phys. Rev. Lett.* **97**, 186801 (2006).
[19] Rejec, T. & Meir, Y. Magnetic impurity formation in quantum point contacts. *Nature* **442**, 900-903 (2006).
[20] Wang, C.-K. & Berggren, K.-F. Local spin polarization in ballistic quantum point contacts. *Phys. Rev. B* **57**, 4552-4556 (1998).
[21] Tokura, Y. & Khaetski, A. Towards a microscopic theory of the 0.7 anomaly. *Physica E: Low-dimensional Systems and Nanostructures*, **12**, 711 (2002).
[22] Aryanpour, K. & Han, J. E. Ferromagnetic Spin Coupling as the Origin of 0.7 Anomaly in Quantum Point Contacts. *Phys. Rev. Lett.*, **102**, 056805 (2009).
[23] C. Sloggett, C., Milstein, A. I., & Sushkov, O. P. Correlated electron current and temperature dependence of the conductance of a quantum point contact. *Eur. Phys. J. B* **61**, 427432 (2008).
[24] Theoretical work on nonparabolic barriers is being pursued in the group of H. Baranger, private communication (2012).
[25] Mahan, D. Many-Particle Physics. Kluwer Academic, New York (2000).
[26] Cronenwett, S. M., Lynch, H. J., Goldhaber-Gordon, D., Kouwenhoven, L. P., Marcus, C. M. Low-Temperature Fate of the 0.7 Structure in a Point Contact: A Kondo-like Correlated State in an Open System. *Phys. Rev. Lett.* **88**, 226805 (2002).
[27] Connor, J. N. L. On the semiclassical approximation for double well potentials. *Mol. Phys.*, **15**, 37 (1968).
[28] Miller, W. H. Semiclassical Treatment of Multiple Turning-Point Problems – Phase Shifts and Eigenvalues. *J. Chem. Phys.*, *48*, 1651 (1968).
[29] Haldane, F. D. M. Scaling Theory of the Asymmetric Anderson Model. *Phys. Rev. Lett.* **40**, 416-419 (1978).
[30] Thomas, K. J., Nicholls, J. T., Pepper, M., Tribe, W. R., Simmons, M. Y. & Ritchie, D. A. Spin properties of low-density one-dimensional wires. *Phys. Rev. B* **61**, R13365-13368 (2000).
[31] Reilly, D. J. Phenomenological model for the 0.7 conductance feature in quantum wires. *Phys. Rev. B*, **72**, 033309 (2005).
[32] Metzner, W., Salmhofer, M., Honerkamp, C., Meden, V. & Schönhammer, K. Functional renormalization group approach to correlated fermion systems. *Rev. Mod. Phys.* **84**, 299 (2012).
[33] Karrasch, C. Transport through Correlated Quantum Dots - a Functional Renormalization Group Approach. *Diploma thesis*, Universität Götingen (2006).
[34] Karrasch, C., Enss, T. & Meden, V. Functional renormalization group approach to transport through correlated quantum dots. *Phys. Rev. B*, **73**, 235337 (2006).
[35] Karrasch, C., Hecht, T., Weichselbaum, A., Oreg, Y. & von Delft, J. Mesoscopic to Universal Crossover of the Transmission Phase of Multilevel Quantum Dots. *Phys. Rev. Lett.* **98**, 186802 (2007).
[36] Bauer, F., Heyder, J. & von Delft, J. Functional Renormalization Group Treatment of a Quantum Chain Model for the Kondo Effect and the 0.7-Anomaly. *to be published.*
[37] Andergassen, S., Enss, T., Meden, V., Metzner, W. & Schollwöck, U. Functional renormalization group for Luttinger liquids with impurities. *Phys. Rev. B* **70**, 075102 (2004).
[38] Bauer, F. 0.7 Anomaly of Quantum Point Contacts: Treatment of Interactions with Functional Renormalization Group. *Diploma thesis*, LMU Munich (2008).
[39] Jakobs, S. G., Meden, V. & Schoeller, H. Nonequilibrium Functional Renormalization Group for Interacting Quantum Systems. *Phys. Rev. Lett.* **99**, 150603 (2007).
[40] Karrasch, C., Hedden, R., Peters, R., Pruschke, T., Schönhammer, K. & Meden, V. A finite-frequency functional RG approach to the single impurity Anderson model. *J. Phys.: Condensed Matter*, 20, 345205 (2008).
[41] Jakobs, S. G., Pletyukhov, M. & Schoeller, H. Nonequilibrium functional RG with frequency dependent vertex function - a study of the single impurity Anderson model. *Phys. Rev. B*, **81**, 195109 (2010).
[42] Wang, C.-K. & Berggren, K.-F. Spin splitting of subbands in quasi-one-dimensional electron quantum channels. *Phys. Rev. B* **54**, R14257-14260 (1996).
[43] Oguri, A. Transmission Probability for Interacting Electrons Connected to Reservoirs. *J. Phys. Soc. Jap.* **70**, 2666 (2001).
[44] Y. Meir & N. S. Wingreen. Landauer formula for the current through an interacting electron region. *Phys. Rev. Lett.* **68**, 2512-2515 (1992).
[45] Bruognolo, B. Störungstheoretische Analyse der Magnetfeldabhängigkeit der 0.7 Anomalie in Quantenpunktkontakten. *Bachelor Thesis*, LMU Munich (2011).
[46] Gangkofner, D. WKB-Calculations on the 0.7-Conductance Anomaly of Quantum Point Contacts. *Bachelor Thesis*, LMU Munich (2010).